POLITECNICO DI TORINO

I Facoltà di Ingegneria

Corso di laurea in Ingegneria Aerospaziale

Tesi di Laurea Specialistica

Campo di pressione medio e perturbato nello strato limite tridimensionale

Perturbative and mean pressure field
in the three-dimensional boundary layer

Relatori: Candidato:

Prof. Daniela Tordella   Andrea Boscolo

Dott. Stefania Scarsoglio

Dicembre 2012

<< Homines enim sunt hac lege
generati, qui tuerentur illum globum,
quem in hoc templo medium vides,
quae terra dicitur, iisque animus datus
est ex illis sempiternis ignibus, quae
sidera et stellas vocatis, quae globosae
et rotundae, divinis animatae mentibus,
circulos suos orbesque conficiunt
celeritate mirabili>>

Somnium Scipionis, Cicerone

Introduzione

Lo strato limite rappresenta, forse, la più importante regione di interesse in un fluido viscido ed è responsabile della maggior parte degli importanti fenomeni che lo contraddistinguono, come il distacco della vena fluida o i forti gradienti termici e di velocità. Sicuramente uno dei più importanti fenomeni è la transizione dal campo laminare a quello turbolento, indicata dal numero di Reynolds. Il campo turbolento è sicuramente lo stato di maggior interesse ed è oggetto di indagine approfondita in questa tesi.

In particolare, ci si propone di esaminare lo strato limite tridimensionale, generato dal fenomeno del "crossflow" che ha luogo sulle ali a freccia, e di calcolare il campo di pressione, medio e perturbato, che in esso si viene a creare introducendo perturbazioni molto piccole.

In primo luogo si fornisce una descrizione delle differenze che intercorrono nel trattare uno strato limite bidimensionale, introdotto concettualmente nel primo capitolo, ed uno tridimensionale "crossflow", soprattutto per quanto riguarda le cause che generano la transizione. Quest'ultimo viene trattato approfonditamente nel secondo capitolo, dove si introduce la TEORIA DELLA STABILITÀ DEI FLUSSI LAMINARI, in modo tale da elaborare un metodo tramite il quale calcolare il campo di pressioni e di velocità, ovvero vengono presentate ed adattate allo strato limite tridimensionale le *equazioni di Navier-Stokes*. Inoltre, vengono descritte le principali fenomenologie legate all'instabilità in uno strato limite crossflow, primaria e secondaria, fornendone una descrizione evolutiva e qualitativa, in modo tale da inquadrare il campo in cui ci si trova a calcolare il campo di pressione.

Nel terzo capitolo si fornisce la formulazione analitica necassaria al calcolo del campo di velocità, ovvero il problema ai valori iniziali, attraverso la quale si può risalire ai metodi utilizzati per la simulazione numerica del campo di pressione perturbato. Viene ricavato analiticamente, inoltre, il fattore di amplificazione, utile come confronto con gli andamenti temporali ottenuti delle pressioni.

Nel quarto capitolo, punto focale di questa tesi, si espongono i risultati ottenuti

tramite la simulazione numerica su MATLAB e si effettua l'analisi delle curve di pressione, nello spazio e nel tempo, al variare dei parametri caratteristici del flusso di crossflow, per configurazioni del flusso ritenute stabili ed instabili.

Nell'ultimo capitolo, infine, si dimensionalizza il campo di pressione perturbato e lo si sovrappone al campo medio di pressione, così da ottenere il campo di pressione reale dimensionale e fornire un ordine di grandezza dei valori presenti nel campo. Tutto ciò viene realizzato per proporre un'applicazione del metodo a campi di studio reali come quelli strutturale ed aeroelastico.

Abstract

Boundary layer represents the most important region in a viscid flow and it is responsable for the main significant phenomena which mark it, as the stream separation or strong thermal and velocity gradients. Certainly, one of the most important phenomena is the laminar-turbulent transition, suggested by the Reynolds number. The turbulent field is the state of major interest and it is the subject of deep investigation in this thesis.

In particular, the three-dimensional boundary layer, caused by the "crossflow" which is generated in swept-back wings, is investigated and the pressure field, mean and perturbative, is computed. This perturbative pressure field is due to the introduction of very small disturbances.

First, a description of the differences between a bidimensional boundary layer, introduced in the first chapter, and a crossflow three-dimensional boundary layer is given, mainly of the reason why transition is generated. This crossflow boundary layer is deeply treated in the second chapter, where the THEORY OF STABILITY OF LAMINAR FLOWS is introduced, in order to develop a method to compute the pressure and velocity fields. So the *Navier-Stokes equations* are presented and modified for the three-dimensional bounadry layer. Moreover, main phenomena related to the instability, primary and secondary, in a crossflow boundary layer, giving an evolutionary and qualitative description, in order to focus on the field where the pressure field is computed.

In the third chapter mathematical formulation, needed to compute the velocity field, is given; This permits to develop the methods for the numerical simulation of the perturbative pressure field. Furthermore, the amplification factor, which is useful as a comparison between obtained temporal pressure trends, is derived.

In the fourth chapter, focal point of this thesis, obtained results are shown, through the numerical simulation on MATLAB, and an analysis of pressure curves, in time and space, is made on varying characteristic parameters of the crossflow boundary layer, for stable and unstable flow configurations.

In the last chapter, finally, perturbative pressure field is made dimensional and it is superimposed to the mean pressure field in order to obtain dimensional total pressure field and give an idea of pressure quantities orders of magnitude. This is made in order to suggest an application of the method for practical studies as structural problems and aeroelasticity.

Ringraziamenti

In primo luogo vorrei ringraziare la Professoressa Daniela Tordella per avermi dato la possibilità di realizzare questo lavoro di tesi, fornendomi numerose ed utili indicazioni, a fronte di lunghe discussioni in ufficio, ma senza le quali non sarebbe stato possibile ottenere tale risultato.

Inoltre, un ringraziamento particolare e sentito va alla Dottoressa Stefania Scarsoglio per le innumerevoli ore dedicatemi negli uffici del dipartimento. Il confronto quotidiano è stato fondamentale ed imprescindibile al fine della comprensione di ogni aspetto del lavoro realizzato. Credo sia molto raro trovare una disponibilità così grande.

Vorrei ringraziare anche Francesca De Santi e Federico Fraternale per due consigli fondamentali nell'impostazione del mio lavoro nelle fasi iniziali. Senza il tuo aiuto, Federico, e la tua sincera disponibilità riguardo alla scrittura dei codici MATLAB, le ore di simulazione numerica sarebbero risultate interminabili.

Un grazie va alla mia Yara, che rappresenta il centro della mia vita. Tutto sarebbe insostenibile senza di te.

Grazie ai miei genitori, che soffrono e gioiscono con me, giorno dopo giorno, e nei momenti difficili hanno scacciato ogni dubbio, spingendomi fino a qui.

Un grazie a Maria Luisa ed Alessandro, che mi hanno sempre trattato come un figlio, anche quando le mia ansia pre-esame toccava livelli insopportabili. Scrivere questa tesi in lingua inglese è merito della mia "teacher" e dei lunghi lunedì pomeriggio di conversazione.

Un grazie a Giancarlo Gramoni e alle ottime persone del suo studio, che nel tempo sono diventate amiche.

Un grazie sincero e felice ai miei "gruppi di studio", dei quali hanni fatto in primo luogo Fabri e poi Matte, Gianni, Gianluca, Luiber, Michele, Carlo, che hanno reso questo lunghissimo cammino un po' meno faticoso.

5

Ringrazio i miei amici "torinesi", Robi, Giuli, Alan, Beck, Guly, e gli amici di una vita, Gavaz e Zava, con i quali ho trascorso e, spero, trascorrerò ancora momenti incancellabili. Inoltre, ringrazio tutte le "mie ragazze" e il Presidente del Vaia perchè rappresentate un'esperienza personale unica.

Infine, una dedica speciale va a quattro persone care, che oggi non possono più essere qui con me. Sono il mio passato ed io il loro futuro. Ciò che sono è dovuto a voi.

Contents

1 Boundary layer

1.1 Introduction

Boundary layer is the field we refer to, during the whole analysis, focusing on computation and parametric analysis of pressure field, which generate in it under some fixed flow conditions, after having shown main phenomenologies, both in two-dimansional field and three-dimensional field. Then it is useful to introduce, historically and theoretically, the *boundary layer* [1].

During the week of 8 August 1904, a small group of mathematicians and scientists gathered in Heidelberg, Germany, where the *Third International Mathematics Congress* took place. During the meeting, professor Ludwig Prandtl introduced e described a new concept that would revolutionized the understanding and analysis of fluid dynamics. His presentation, and the subsequent paper, introduced the concept of BOUNDARY LAYER in a fluid over a surface. The modern world of aerodynamics and fluid dynamics is still dominated by Prandtl's idea.

To set the stage in which this inovative concept, let us take a quick journey back over the history and development of fluid dynamics. Archimede introduced some basic ideas in fluid statics, and Leonardo da Vinci observed and drew sketches of complex flows over objects in streams. A quantitative physical and mathematical understanding of fluid flow began when Isaac Newton made examination of fluid dynamics and fluid statics in Book II of *Principia Mathematica*, published in 1687.

Efforts to obtain a mathematical formulation of a fluid flow took shape during next century with the contributions Bernoulli, D'Alambert and Euler. Euler, in particular, described flow in terms of spatially varying three-dimensional pressure and velocity fields and modeled the flow as a continuous collection of infinitesimally small fluid elements. By applying the basic principles of mass conservation and Newtons second law, Euler obtained two *coupled, nonlinear partial differential equations* involving the flow fields of pressure and velocity. But obtaining general solutions of them was realy difficult. Moreover, Euler did not account for the effect of friction

acting on the motion of the fluid elements, that is he ignored viscosity.

It was another hundred years before a system of even more elaborate nonlinear partial differential equations, called the *Navier-Stokes equations*, were introduced in order to count viscosity effects. This system of equations are the gold standard in the mathematical description of a fluid flow, and no one has yet obtained a general analytical solution of them.

The inability to solve the NavierStokes equations for most practical flow problems was particularly frustrating to those investigators interested in calculating the frictional shear force on a surface immersed in a flow. This difficulty became acute at the beginning of the 20th century, with the invention of the first practical airplane by Orville and Wilbur Wright and with the subsequent need to calculate the lift and drag on airplanes. The fluid, indeed, exerts a net aerodynamic force on the airfoil, caused by fluid pressure and the shear stress that results from friction between the surface and the flow, as one can notice from figure 1.
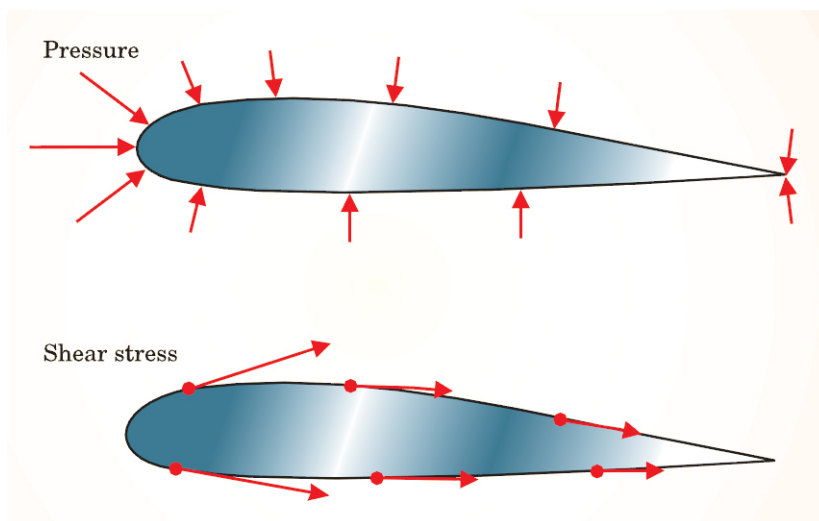

Figure 1: Pressure (a) and shear-stress (b) distribution on an airfoil [1].

To determine the force, aerodynamicists need to calculate both the pressure and shear-stress distributions and then integrate them over the surface of the airfoil.

Calculating the shear-stress distribution requires the inclusion of internal friction and the consideration of viscous flow.

1.2 Boundary layer concept

Prandtl, in his paper, theorized that an effect of friction was to cause the fluid immediately adjacent to the surface to stick to the surface (*no-slip condition* at the surface) and that frictional effects were experienced only in a boundary layer, a thin region near the surface. Outside the boundary layer, the flow was essentially the inviscid flow.

A graphic rappresentation of the boundary leyer ragion is given in figure 2, where one can observe, in types of flows associated with a body in flight, that the boundary layer is very thin compared to the size of the body.
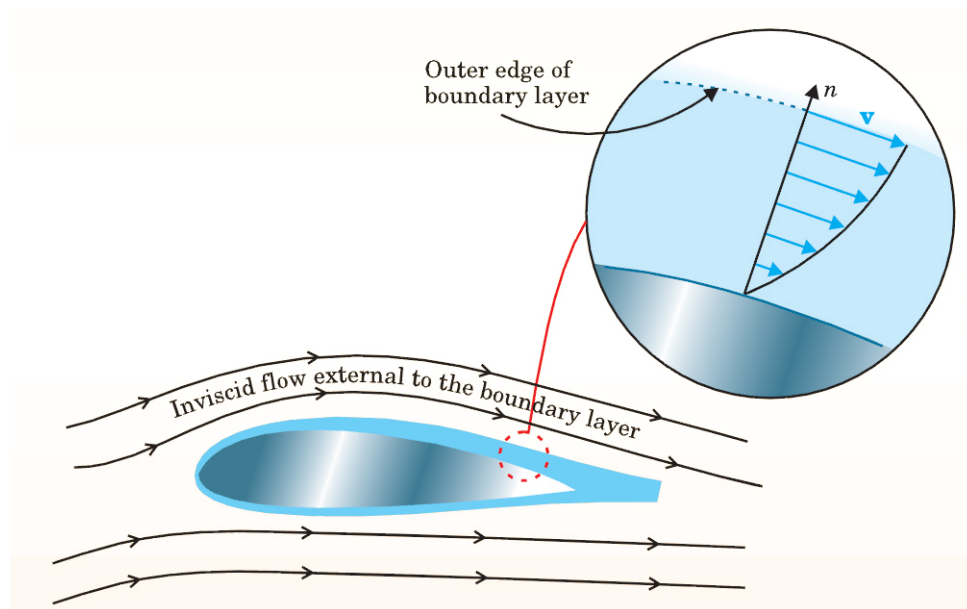

Figure 2: Airfoil boundary layer [1].

This id the Prandtl's description of boundary layer:

A very satisfactory explanation of the physical process in the boundary layer [Grenzschicht] between a fluid and a solid body could be obtained by the hypothesis of an adhesion of the fluid to the walls, that is, by the hypothesis of a zero relative velocity between fluid and wall. If the viscosity was very small and the fluid path along the wall not too long, the fluid velocity ought to resume its normal value at a very short distance from the wall. In the thin transition layer [Übergangsschicht] however, the sharp changes of velocity, even with small coefficient of friction, produce marked results.

One of those marked results is illustrated in figure 2: The velocity changes enormously over a very short distance normal to the surface of a body immersed in a flow. In other words, the boundary layer is a region of very large velocity gradients. According to Newtons shear-stress law, which states that the shear stress is proportional to the velocity gradient, the local shear stress can be very large within the boundary layer. As a result, the skin-friction drag force exerted on the body is not negligible. Moreover, most of the drag is due to skin friction.

1.3 Analitical solutions for the boundary layer

Once the concept of boundary layer is defined, we need to reach a satisfying analitical solution, concerning its mathematical modelling.

The outer inviscid flow strongly affects the boundary-layer properties; indeed, the outer flow creates the boundary conditions at the outer edge of the boundary layer and dictates, at the same time, the velocity profile within the layer. On the other hand, the boundary layer is so thin that it has virtually no effect on the outer inviscid flow.

Prandtl showed that for the boundary layer, the Navier-Stokes equations can be reduced to a simpler form, applicable only to characteristic region of the flow. The result of such a reduction processes the formulation of so called *boundary layer equations*, which are similar to Navier-Stokes in that each system consists of coupled, nonlinear partial differential equations and they will be useful hereafter in the thesis.

Boundary layer equations exhibit a completely different mathematical behavior than Navier Stokes equations system. The latter has an elliptic behavior, that is to say, the complete flow field must be solved simultaneously, in accord with specific boundary conditions defined along the entire boundary of the flow. In contrast, the boundary-layer equations have parabolic behavior, which affords tremendous analytical and computational simplification. They can be solved "step-by-step" by marching downstream from where the flow encounters a body, subject to specified inflow conditions at the encounter and specified boundary conditions at the outer edge of the boundary layer. The systematic calculation yields the flow variables in the boundary layer, including the velocity gradient at the wall surface, from which shear stresses at the wall, hence the skin-friction drag on the surface, is directly obtained.

With those solutions, it became possible to predict with some accuracy the skin-friction drag on a body, the locations of flow separation on the surface, and, given those locations, the form drag, the pressure drag due to flow separation. In the paper Prandtl gave the boundary-layer equations for steady two-dimensional flow, suggested some solution approaches for those equations, made a rough calculation of friction drag on a flat plate, and discussed aspects of boundary-layer separation under the influence of an adverse pressure gradient.

Studies about two-dimensional boundary layer flows over a flat plate and a circular cylinder were took back by Blasius, one of the Prandtl's students. He solved the boundary-layer equations in both cases. For the flat plate, he obtained an even more accurate solution for skin-friction drag than appeared in Prandtls previous calculations. It is important to notice how boundary layer equations, though simpler than NavierStokes, are still coupled, nonlinear partial differential equations. However, for certain types of pressure gradients in the flow, they reduce to a single ordinary differential equation. That simplification happens, for example, for the constant pressure along a flat plate oriented parallel to the flow. Indeed, the equation that applies to a flat plate at zero attack angle is known, today, as the *Blasius equation*.

Then, in 1921, Theodore von Kármán, a former student of Prandtls obtained a momentum-integral equation through the simple expedient of integrating the boundary-

layer equations across the boundary layer. That equation proved to be directly applicable to a large number of practical engineering problems and, thanks to this extension, the BOUNDARY LAYER THEORY can be used in practical technical applications. The first serious industrial application of boundary-layer theory occurred in the last century when designers began to use the theorys results to predict skin-friction drag on airships and airplanes. Prior to that time, they had been limited to using empirical data obtained primarily from wind tunnels, but such results concern total drag and the effect of skin friction was difficult to cull out.

From that time, sevaral books, about various aspects of boundary-layer theory, were written. The most complete of them is, without doubt, Hermann Schlichting's "*Boundary Layer Theory*", on which we will base for next arguments of the thesis.

1.4 Laminar-turbolent boundary layer transition

The instability of laminar boundary layer flows and the transition to turbulence are objects of studies in fluid mechanics problems. This interest results from the fact that transition controls important aerodynamic quantities such as drag or heat transfer. For example, the heating rates generated by a turbulent boundary may be several times higher than those for a laminar boundary layer, so that the prediction of transition location is of great importance for aerospace applications such as hypersonic re-entry spacecraft, because the thickness of the thermal protection system (TPS) is strongly dependent upon the altitude where transition occurs.

Furthermore, it is important to concentrate on the specific aspects of transition in three-dimensional flows. This phenomenon is the so-called *crossflow instability*, which exhibit features and properties completely different from those of two-dimensional instability. The thesis will be focalize on such a specific field showing this particular crossflow instability for certain Reynolds numbers.

To describe the laminar-turbulent transition process in two-dimensional (2D) or threedimensional (3D) flows, it is usual to distinguish three successive steps [2]. The first step, which takes place close to the leading edge, is called "*receptivity*". It de-

scribes the means by which forced disturbances such as free-stream noise, free-stream turbulence, vibrations, small roughness elements enter the laminar boundary layer and excite its *eigenmodes*. In the second phase, these eigenmodes take the form of periodic waves, the energy of which is convected in the streamwise direction. Some of them are amplified and will be responsible for transition. Their evolution is well described by the *linear stability theory*, mentioned before. When the wave amplitude becomes finite, *non linear interactions* occur and lead rapidly to turbulence. The general features of these three steps are briefly described below, teorically and analitically.

Receptivity. Describes the link between the excitation sources and the initial amplitude A_0 of the boundary layer eigenmodes. Two important results are:
i) A_0 increases when the amplitude of the excitation increases
ii) a perturbation of frequency f excites waves having the same frequency.
If there is no excitation of frequency f, then there is no chance to observe waves of frequency f travelling in the boundary layer, even if these waves are unstable according to the linear stability theory. The receptivity process is completely different for two-dimansional and for three-dimansional flows.

Linear stability theory. The principle of this theory is to introduce small sinusoidal disturbances into the Navier- Stokes equations in order to compute the range of unstable frequencies. Any fluctuating quantity r (velocity, pressure, density or temperature) is expressed by:

$$r = \hat{r}(y) \cdot \exp[i(\alpha x + \beta z - \omega t)]$$

where $\hat{r}$ is an amplitude function and y is normal to the surface. In the particular case of a swept wing, x is often measured along the wing surface in the direction normal to the leading edge, z is the spanwise direction. In general, α, β and ω are complex numbers. α and β represent the wave number components, in the x and z directions, and the wave frequency.

15

The fluctuating quantities are very small, so that the quadratic terms of the disturbances are neglected in the Navier-Stokes equations. It is also assumed that the *mean flow* quantities do not vary significantly over a wavelength of the disturbances. Mean flow velocity components, U and W, in the x and z directions, as well as the mean temperature T are functions of y alone, and the vertical velocity V is equal to zero. The implication of this "parallel flow" assumption is that the stability of the flow at a particular location (x, z) is determined by the local conditions at that location independently of all others. This leads to a system of homogeneous, ordinary differential equations for the amplitude functions. For two-dimensional, low speed flows, these equations reduce to the well-known *Orr-Sommerfeld equation*, the solutions of which represent the classical *Tollmien-Schlichting waves*, showed in figure 3. The transition process, represented in figure below, in the boundary layer, is referred to the case of a flate plate, wraped by low turbolence intencity free flow. As one can easily notice, the flow move throw subsequent steps, starting from the leading edge.
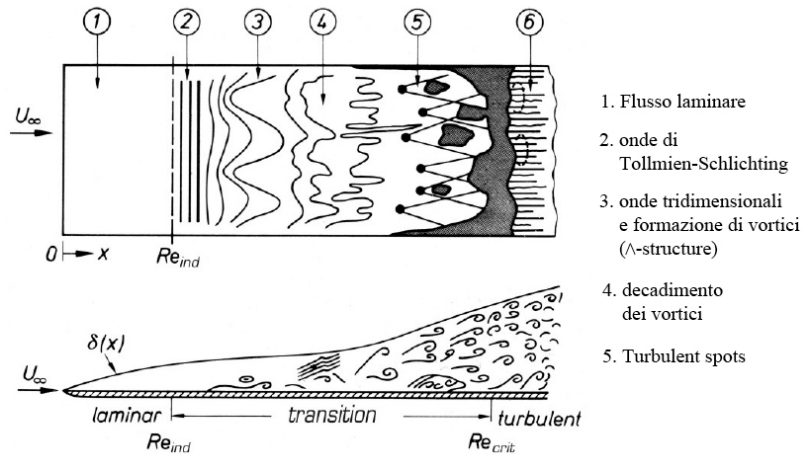
Figure 3: Laminar-turbolent transition (point 6) and flow evolution inside the boundary layer on a flat plate with zero angle of attack [3].

Due to the homogeneous boundary conditions, the problem is an eigenvalue one.

16

For a given mean flow field, non trivial solutions exist for certain combinations of the parameters α, β, ω and R, where R is the Reynolds number.

The transition process, shown in figure 3, inside the boundary layer is referred to the case of a flat plate wrapped by a slow turbulence intensity outer flow. As it can be noticed, the flow is moving through following states, beginning from the leading edge. Taking into account a spatial theory, concerning transition mechanisms governed by a convective instability, ω can be express as real number and α as a complex. For the sake of simplicity, it will be assumed that β is also real. Therefore r is expressed by:

$$r = \hat{r}(y) \cdot \exp(-\alpha_i x) \cdot \exp[i(\alpha_r x + \beta z - \omega t)]$$

The spatial growth rate $-\alpha_i$ is the opposite of the imaginary part of α, α_r being the real part. The wave number vector $\vec{k} = (\alpha_r, \beta)$ makes an angle ψ with respect to the x direction. When the mean flow is specified, the eigenvalues α_r and α_i are computed for imposed values of β, ω and R. On the $R - \omega$ *diagram*, also called *stability diagram*, showed in figure 4, a neutral curve $(-\alpha_i = 0)$ separates the stable region where the disturbances are damped $(-\alpha_i < 0)$, from the unstable region $(-\alpha_i > 0)$, where the disturbances are amplified.
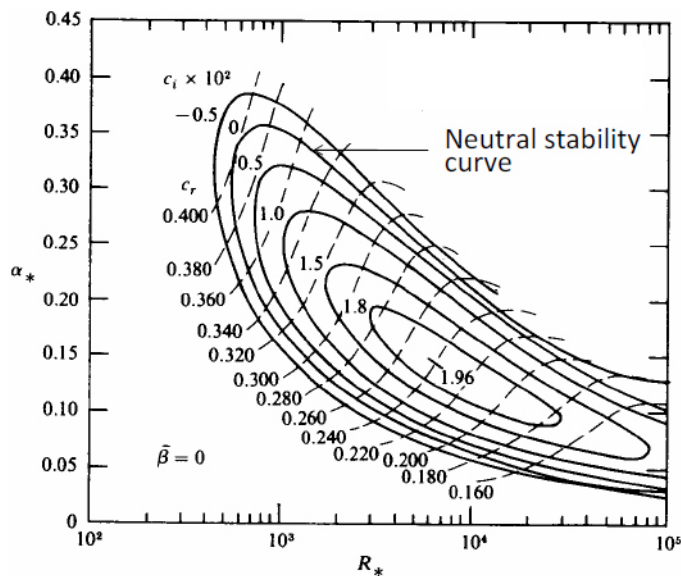
Figure 4: $R - \omega$ *diagram*, in which one can notice the neutral instability curve [2].

Non-linear phase.   On this stage, disturbances are expressed as a double series of (n, m) *modes* of the form:

$$r = \sum_{n=-\infty}^{n=+\infty} \sum_{m=-\infty}^{m=+\infty} \hat{r}_{nm}(x, y) \cdot exp[i(\int \alpha_{nm}(\xi)d\xi + m\beta z - n\omega t)]$$

where α_{nm} is complex, β and ω are real numbers.

The integers n and m characterise the frequency and the spanwise wave number, respectively. When these disturbances are introduced into the Navier-Stokes equations, a system of coupled partial differential equations is obtained, which is solved by a marching procedure. Any non linear computation requires to choose the most interesting interaction scenario between particular modes which are referred to as "major modes" and to impose initial amplitudes A_0 for these modes. For 2D flows, non linear computations end with a sudden increase of the major modes and of their harmonics; this simulates the *breakdown to turbulence*. On the other hand, for 3D flows, the non linear interactions result in a saturation of the amplitude of all the

18

modes, without any indication of *breakdown*. It is then necessary to use a *secondary instability theory* to predict transition, as will be presented up ahead.

1.4.1 "Natural" transition in two-dimensional flows

An important aspect of instability for compressible flows is the effect of the wave number direction "ϕ", the so called *obliquity angle*, on the amplification rates. Up to Mach numbers of the order of 0.7 to 0.8, the maximum value of $-\alpha_i$, for a given Reynolds number, usually corresponds to $\phi = 0^o$. At transonic Mach numbers, the largest growth rates are obtained for non zero values of ϕ (oblique waves). Typically, the most unstable direction is around 40° o 50° for Mach numbers close to unity.

For flat plates up to $M = 2,2$, on adiabatic wall, the unstable region in the $R - \omega$ *diagram* is contained into a single curve. At higher Mach numbers, the waves become supersonic relative to the mean flow close to the wall; this results in the generation of higher modes on the diagram. In figure 5 two stability diagram are showed, for $M = 4,5$ and two different values of ϕ: 0° and 60°. Variables which appears in the diagram are: R_δ, the displacement thickness Reynolds number, α_i, made dimensionless with δ, and ω, made dimensionless with δ and the free stream velocity U_e.
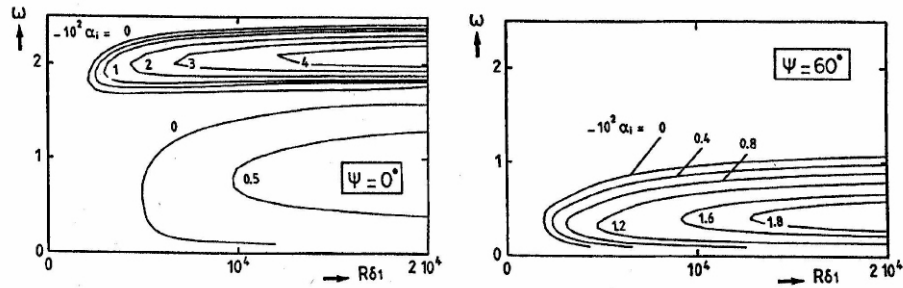
Figure 5: Effect of wave orientation ϕ on the growth rate $-\alpha_i$ [2].

As we can see from the figure above, for $\phi = 0^o$, two unstable loops are visible. The unstable region associated with low values of ω is the equivalent of the unique

unstable region observed at low Mach number and is referred to as the *first mode.* The second loop, at higher frequencies, is the *second mode* resulting from the existence of the supersonic waves. The results for $\phi = 60^o$, on the right hand side of figure 5, show that changing the wave orientation stabilises the second mode, but increases the instability of the first one. This is a general rule: systematic computations demonstrated that the most unstable first mode disturbances are oblique, whilst the most amplified second mode waves are two-dimensional.

In supersonic and hypersonic wind tunnels, the main factor affecting transition on two-dimensional models is the *noise*, the origin of which lies in the pressure disturbances radiated by the turbulent boundary layers developing along the nozzle walls. This leads to low transition Reynolds numbers, which decrease with increasing free-stream pressure fluctuations in the nozzle. In order to reduce this noise level, it is necessary to delay transition on the nozzle walls, because a laminar boundary layer is less noisy than a turbulent one. This was done in the so called quiet tunnel. A careful polishing and a careful design of the nozzle walls contour in order to minimise the development of *Görtler vortices.* With a laminar boundary layer on the nozzle walls, the measured pressure fluctuations can be one or two orders of magnitude below those measured in conventional facilities.

Other factors which affect transition are:

- wall cooling

- leading edge bluntness

- real gas effects

When *wall cooling* is applied, the stability properties change dramatically. Cooling a wall strongly stabilises first mode disturbances and has less effect on second mode disturbances. At low Mach numbers, very large values of the transition Reynolds number Re_t can be achieved with a moderate cooling. These trends have been observed in wind tunnels and in flight conditions; they have been confirmed by linear stability computations.

20

In hypersonic flows, a small *nose bluntness* of a cone at zero angle of attack or a *small leading edge bluntness* of a flat plate strongly affects the transition location because it reduces the local Reynolds number and creates a negative pressure gradient which stabilises the flow. As a result, transition is delayed. When the nose or leading edge bluntness becomes large, the downstream movement of transition is no longer observed, but, on the contrary, transition begins to move upstream.

At hypersonic speeds, the gas often cannot be modelled as perfect because the molecular species begin to dissociate due to aerodynamic heating. It is important, therefore, the analysis of *real gas effects* on stability properties.
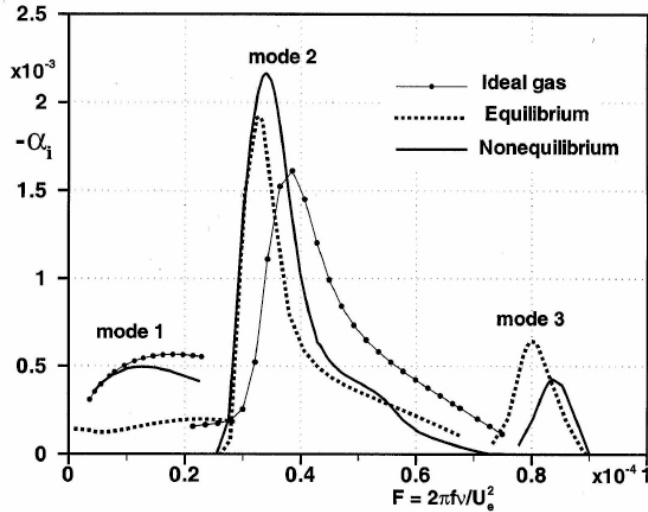
Figure 6: *Real gas effects* on stability properties [2].

Figure 6 shows the variation of the growth rate as a function of a dimensionless frequency F for a flat plate flow at a $Mach = 10$, $Re_x = 4 \cdot 10^6$, $T_e = 350\,K$ and adiabatic wall. The computations have been performed for ideal gas, chemical equilibrium and non equilibrium. In the latter two cases, a third unstable mode appears, and instability is enhanced for the second mode.

1.4.2 "Natural" transition in three-dimensional flows

Presenting the natural transition in threedimensional flow it is useful to note that the mean velocity profile of a boundary layer developing on a three-dimensional body can be decomposed into a streamwise mean velocity profile u, in the direction of the external streamline, and a "crossflow" velocity profile w, in the direction normal to this streamline. Figure 7 shows a schematic view of the boundary layer development on a swept wing, with a negative pressure gradient in the leading edge region and a positive pressure gradient further downstream. This scheme will be take into account at the end of the thesis in order to introduce an analitical computation practical extension.
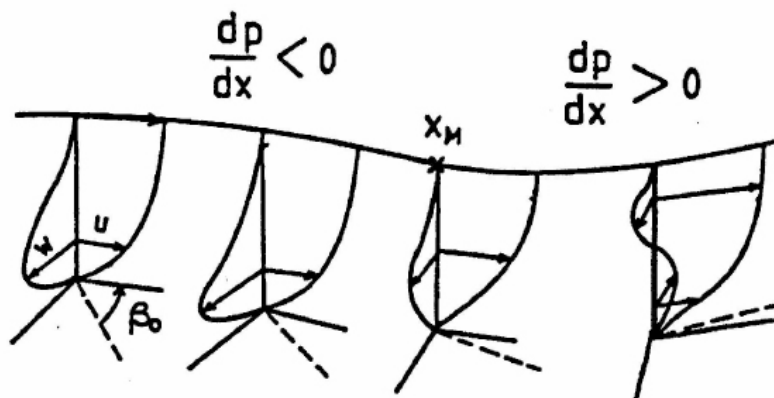
Figure 7: Laminar boundary layer development on a swept wing [2].

On the graph, x_m is the location of the inviscid streamline inflection point and β_0 is the angle netween the wall and potential streamline.

As the streamwise mean velocity profiles look like classical two-dimensional velocity profiles, their instability properties are qualitatively similar to those of two-dimensional flows; in particular first and second mode disturbances are likely to exist at large Mach numbers. This corresponds to the "*streamwise instability*". On the other side, an inflection point is always present in the crossflow mean velocity

profile. As a consequence a powerful inflectional instability is expected to occur in regions where w develops rapidly. This phenomenon is called "*crossflow instability*". It is observed, for instance, in the vicinity of the leading edge of a swept wing, a region where the crossflow mean velocity profile w develops rapidly due to the strong negative pressure gradient.

It is to note that the unstable frequency range is usually wider for crossflow instability than for streamwise instability. In particular, linear stability theory shows that crossflow instability can amplify zero frequency disturbances. This leads to the formation of *stationary vortices*, the axes of which are close to the streamwise direction. These vortices can be visualised as streaks on the surface, as it can be seen on the infrared picture presented in figure 8. The picture corresponds to supersonic experiments performed at $M = 3$ on a swept wing. The right hand part shows the spanwise variation of the mean wall temperature measured in the area of the ellipse drawn in the left hand part. From this curve a spanwise wavelength close to $1, 5mm$ can be deduced, in very good agreement with linear stability theory.
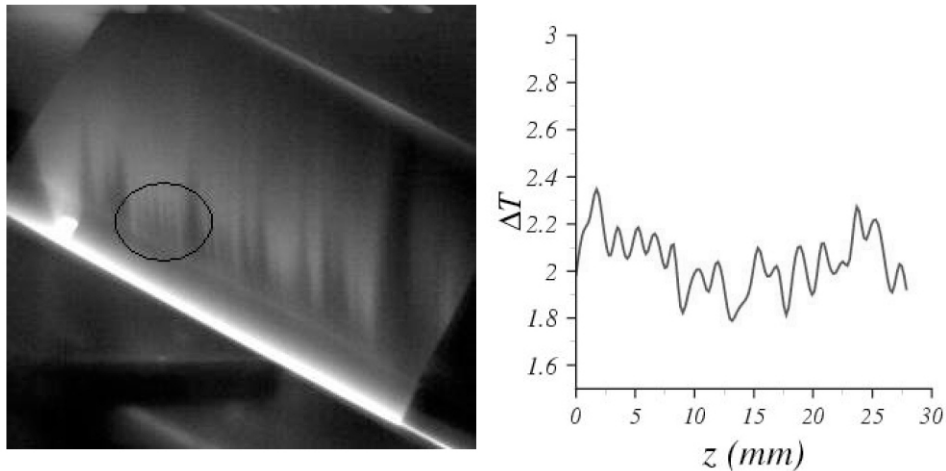
Figure 8: Stationary vortices on a swept wing at supersonic Mach number ($M = 3$) [2].

For 2D flows, it has been shown previously that the unstable waves are mainly excited by the free-stream noise. This is no longer true for 3D flows when transition is governed by a pure crossflow instability. In this case, the stationary vortices mentioned before play the major role in the transition process by creating a steady inflection point in the streamwise mean velocity profile. It follows that noise has only a small effect on the receptivity mechanisms and on transition.

According to the statement that waves of frequency f are generated by excitations of the same frequency, one has to look at stationary excitations to explain the origin of the vortices. For low speed flows, *Radetsky* demonstrated that micron-sized roughness elements are the main factor influencing the generation of the stationary vortices and hence the transition location. This statement seems to remain true for high speed flows, at least at supersonic Mach numbers. This was demonstrated by several series of experiments carried out on a swept wing equipped with a blunt leading edge, whole results are shown in figure 8, and on the same swept wing equipped with a sharp leading edge.

2   Three-dimensional boundary layer

In the previous chapter, boundary layer concept has been introduced and transition inside the region close to wall has been analyzed, both in bidimensional and three-dimensial field. Studies now will be focalized on the last boundary layer typology, caracterized by the so-called crossflow flow, and instability linked phenomenon will be analyzed, in order to explain transition to turbulent.

Problems of two-dimensional and of axially symmetrical flow have this in common that the prescribed potential flow depends only on one space coordinate, and the two vclocity components in the boundary layer depend on two space coordinates each. In the case of a three-dimensional boundary layer the external potential flow depends on two coordinates in the wall surface and the flow within the boundary layer possesses all three velocity components which, moreover, depend on all three space coordinates in the general case. The flow about a disk rotating in a fluid at rest and rotation in the neighbourhood of a fixed wall establish examples of three-dimensional boundary layers.

Another important case of a three dimensional boundary layer is that of an aeroplane wing, whose leading edge is not orthogonal to the stream, as in the case of "*swept-back wings*" and "*yawed wings*". It is known from experience that on the suction side considerable quantities of the fluid move towards the receding end, the phenomenon having a very detrimental effect on the aerodynamic behaviour of the wing.

In two-dimensional motion through a boundary layer, the geometrienl shape of the body influences the field of flow only indirectly. By contrast three-dimensional boundary layers are affected by both: by the external velocity distribution and by the geometrical shape directly.

For the purpose of establishing the three-dimensional boundary layer equations it is useful to confine ourselves to the case of a curved wall which is developed into a plan, in analogy with studies about a yawed cylinder as shown in figure 9.

25
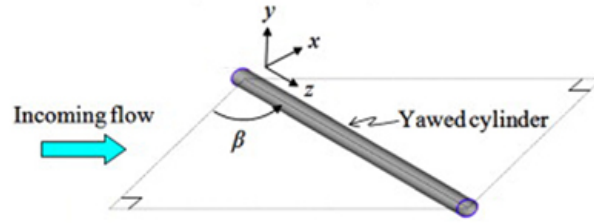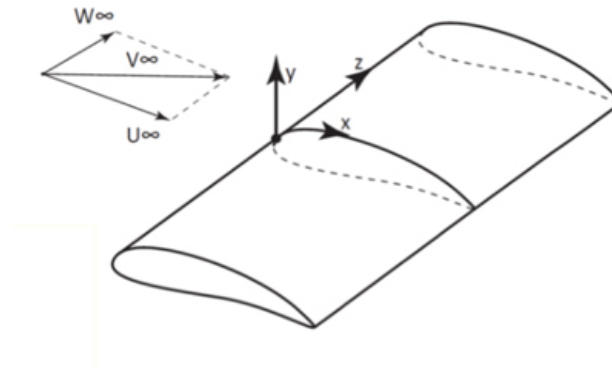
Figure 9: Yawed cylinder with yaw angle β (a) and curved surface developed into a plane (b) .

Let x and z denote the coordinates in the wall surface, while y the coordinate which is orthogonal to the wall. The velocity vector of potential flow, V, will be assumed to have the components $U(x,z)$ and $W(x,z)$, so that, in the steady-state case, the pressure distribution in the potential flow is given by:

$$p + \frac{1}{2}\rho[U^2 + W^2]$$

2.1 Three-dimensional boundary layer equations

Therefore, it is essential to derive equations which control three-dimensional boundary layer [3], proceeding, in order to reach them, with an evaluation similar to the computation of two-dimensional boundary layer *Navier-Stokes equations*. A short summary of this evaluation is listed below in order to formulate equations for considered three-dimensional case.

The Navier-Stokes equations for incompressible flow ($\rho = cost$) assume the following form:

$$\begin{cases} \rho(\frac{\partial u}{\partial t} + u\frac{\partial u}{\partial x} + v\frac{\partial u}{\partial y} + w\frac{\partial u}{\partial z}) = -\frac{\partial p}{\partial x} + \mu(\frac{\partial^2 u}{\partial x^2} + \frac{\partial^2 u}{\partial y^2} + \frac{\partial^2 u}{\partial z^2}) \\ \rho(\frac{\partial v}{\partial t} + u\frac{\partial v}{\partial x} + v\frac{\partial v}{\partial y} + w\frac{\partial v}{\partial z}) = -\frac{\partial p}{\partial y} + \mu(\frac{\partial^2 v}{\partial x^2} + \frac{\partial^2 v}{\partial y^2} + \frac{\partial^2 v}{\partial z^2}) \\ \rho(\frac{\partial w}{\partial t} + u\frac{\partial w}{\partial x} + v\frac{\partial w}{\partial y} + w\frac{\partial w}{\partial z}) = -\frac{\partial p}{\partial z} + \mu(\frac{\partial^2 w}{\partial x^2} + \frac{\partial^2 w}{\partial y^2} + \frac{\partial^2 w}{\partial z^2}) \\ \frac{\partial u}{\partial x} + \frac{\partial v}{\partial y} + \frac{\partial w}{\partial z} = 0 \end{cases}$$

For a non-stationary, bidimansional flow, on $x - y$ plane, Navier-Stokes equations can be reduced to the following system:

$$\begin{cases} \frac{\partial u}{\partial t} + u\frac{\partial u}{\partial x} + v\frac{\partial u}{\partial y} = -\frac{1}{\varrho}\frac{\partial p}{\partial x} + \nu(\frac{\partial^2 u}{\partial x^2} + \frac{\partial^2 u}{\partial y^2}) \\ \frac{\partial v}{\partial t} + u\frac{\partial v}{\partial x} + v\frac{\partial v}{\partial y} = -\frac{1}{\varrho}\frac{\partial p}{\partial y} + \nu(\frac{\partial^2 v}{\partial x^2} + \frac{\partial^2 v}{\partial y^2}) \\ \frac{\partial u}{\partial x} + \frac{\partial v}{\partial y} = 0 \end{cases}$$

which gives the three equations for u, v and p.

In general it is possible to state that the *thickness of the boundary layer* increases with viscosity or that it decreases as the Reynolds number increases. The boundary-layer thickness is proportional to the square root of kinematic wiscosity:

$$\delta \simeq \sqrt{\nu}$$

This thickness is very small compared with a still unspecified linear dimension, L, of the body, so that first semplification of Navier-Stokes eqauations can be considered:

$$\delta \ll L$$

In this way the solutions obtained from the boundary-layer equations are asimptotic and and apply to very large Reynolds numbers.

Through parameters introduction, in order to make equations dimensionless, and a consequent analysis about order of magnitude of each term, tratment of which is dropped here, a semplify form of the equations system could be obtained. In particular, by referring velocities to free-stream velocity, V, and all linear dimensions to a characteristic length L, of the body, which is selected in order to ensure that the dimensionless derivative $\frac{\partial u}{\partial x}$ do not exceed unity in the region under consideration. Moreover, the pressure is made dimensionless with ρV^2 and time is referred to $\frac{L}{V}$. Finally, *Reynolds number* is introduced, which is assumed very large:

$$Re = \frac{VL\rho}{\mu} = \frac{VL}{\nu}$$

A simplify Navier-Stokes equation is obtained, known as *Prandtl's boundary layer equations*, which, coming back to dimensioanal quantities, can be expressed by:

$$\begin{cases} \frac{\partial u}{\partial x} + \frac{\partial v}{\partial y} = 0 \\ \frac{\partial u}{\partial t} + u\frac{\partial u}{\partial x} + v\frac{\partial u}{\partial y} = -\frac{1}{\varrho}\frac{\partial p}{\partial x} + \nu\frac{\partial^2 u}{\partial y^2} \end{cases}$$

with the boundary conditions:

$$\begin{cases} u = v = 0 & per\ y = 0 \\ u = U(x,t) & per\ y = \infty. \end{cases}$$

and the system can become simpler for *stationary flow*.

During the order of magnitude analysis, it can be observed that the Reynolds number is equal to $\frac{1}{\delta^2}$ and can be expressed as:

$$\frac{1}{Re} = \delta^2$$

From this relationship, it can be made a boundary layer thickness valuation:

$$\frac{\delta}{L} \sim \frac{1}{Re} = \sqrt{\frac{\nu}{VL}}$$

and this ratio will be useful up ahead in the thesis.

If now perform the same estimation, under the assumption of very large Reynolds numbers, relative to the *three-dimensional Navier-Stokes equations*, the conclusion can be reached that, in the frictional terms of the equations for the x anrl z directions respectively, it is possible to neglect the derivatives with respect to the coordinates which are parallel to the wall as against the derivative with respect to the coordinates with right angles to it. Regarding the equation in the y-direction we again obtain the result that $\frac{\partial p}{\partial y}$ is very small and may be neglected. Thus the pressure is seen to depend on x and z alone, and is impressed on the boundary layer by the potential flow. Boundary layer equations for three-dimensional flow are:

$$\begin{cases} u\frac{\partial u}{\partial x} + v\frac{\partial u}{\partial y} + w\frac{\partial u}{\partial z} = -\frac{1}{\rho}\frac{\partial p}{\partial x} + \nu\frac{\partial^2 u}{\partial y^2} \\ u\frac{\partial w}{\partial x} + v\frac{\partial w}{\partial y} + w\frac{\partial w}{\partial z} = -\frac{1}{\rho}\frac{\partial p}{\partial z} + \nu\frac{\partial^2 w}{\partial y^2} \\ \frac{\partial u}{\partial x} + \frac{\partial v}{\partial y} + \frac{\partial w}{\partial z} = 0 \end{cases}$$

with the following boundary conditions:

$$\begin{cases} u = v = w = 0 & per\ y = 0 \\ u = U;\ \ w = W; & per\ y = \infty. \end{cases}$$

The pressure gradients $\frac{\partial p}{\partial x}$ and $\frac{\partial p}{\partial z}$ are known from the potential flow in accordance with *Bernoulli equations*, directly derived from free-stream.

2.1.1   Yawed cylinder

A particular case of three-dimensional boundary-layer flow is that where the potential flow depends on x but not on z, as written below:

$$\begin{cases} U = U(x) \\ W = W(x). \end{cases}$$

These conditions are transferable to the case of a *yawed cylinder* and *yawed wing* with zero lift. The system of equations, seen before, is simplified in that there is no dependence on z. Taking into account that $W = W_\infty = cost$ and that $-(1/\rho) \cdot (\partial p / \partial x) = U \cdot (\partial U / \partial x)$, is obtained:

$$\begin{cases} u \frac{\partial u}{\partial x} + v \frac{\partial u}{\partial y} = U \cdot \frac{\partial u}{\partial x} + \nu \frac{\partial^2 u}{\partial y^2} \\ u \frac{\partial w}{\partial x} + v \frac{\partial w}{\partial y} = \nu \frac{\partial^2 w}{\partial y^2} \\ \frac{\partial u}{\partial x} + \frac{\partial v}{\partial y} = 0 \end{cases}$$

with the same boundary conditions as before.
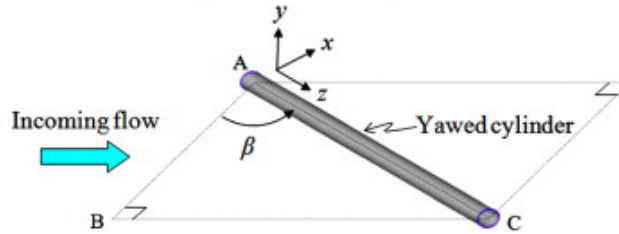
Figure 10: Yawed cylinder.

The calculation of three-dimensional boundary layer on a yawed cylinder, shown in figure 9, can be carried out, by a method, similar to that used in the case of two-dimensional flow about a cylinder, by assuming a *series expansion* with respect to the length of arc measured from the stagnation point. For a symmetrical cylinder it results:

$$U(x) = u_1 x + u_3 x^3 + ... \qquad con \ \ W(x) = W_\infty = cost.$$

Moreover, a characteristic coordinate is defined:

$$\eta = y\sqrt{\frac{u_1}{\nu}}$$

Through this coordinate, $u(x,y)$, $v(x,y)$ and $u(x,y)$ can be expressed by a series expansion with respect to x, where $f_1, f_{3,...}$ costants and $g_0, g_2, ...$ functions are present, satisfying the following differential equations:

$$\begin{cases} g_0'' + f_1 g_0' = 0 \\ g_2'' + f_1 g_2' - 2f_1' g_2 = -12 f_3 g_0' \end{cases}$$

whose boundary conditions are:

$$\begin{cases} g_0 = 0, \ g_2 = 0, \ ... \qquad per \ \eta = 0 \\ g_0 = 1, \ g_2 = 1, \ ... \qquad per \ \eta = \infty \end{cases}$$

As indicated by Prandt the equation for g_0 can be solved by direct integration, the result being:

$$g_0(\eta) = \frac{\int_0^\eta \left\{ \exp\left(-\int_0^\eta f_1 d\eta\right) \right\} d\eta}{\int_0^\infty \left\{ \exp\left(-\int_0^\eta f_1 d\eta\right) \right\} d\eta}$$

where f_1 denotes the solution for the two-dimensional stagnation point flow and it is expressed by: $f_1(\eta) \equiv \Phi(\eta)$. Functions g_0 and g_2 are represented in figure 11.
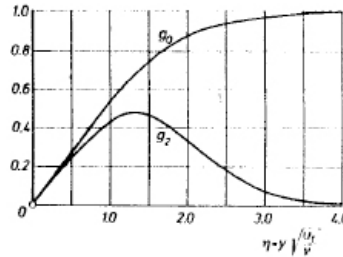
Figure 11: Functions g_0 and g_2 for the velocity component w along the axis of the body, inside laminar boundary layer on a yawed cylinder [3].

2.1.2   Swept wings and cross-flow phenomenon

The existence of *cross-flow* which occurs in the boundary layer of a yawed cylinder, described in last paragraph, is important for the aerodynamic properties of swept wings.

When yawed or swept-back wings operate at higher lift values the pressure on the suction side near the leading edge shows a considerable gradient towards the receding tip, the effect being due to the rearward shift of the airfoil sections of the wing. This phenomenon can be inferred from figure 12, which shows the isobars on the suction side of a yawed wing.
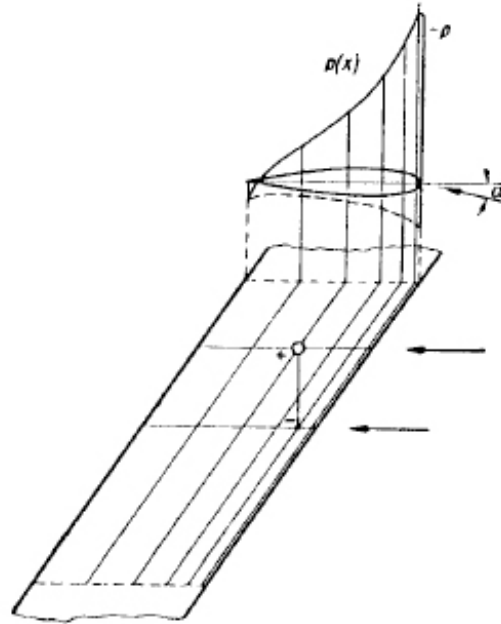
Figure 12: Origin of *cross-flow* on a yawed wing at an angle of incidence [3].

The fluid particles, which become decelerated in the boundary layer, have a tendency to travel in the direction of this gradient, and a *cross-flow* in the direction of the receding tip results, as seen before. The boundary layer on the receding portion thickens, the effect leading to premature separation. In aircraft equipped with swept

32

back wings separation begins at the receding portion, near the ailerons, and causes the dreaded one-winged stall to occur. It is possible to prevent one-winged stalling, by equipping the wing with a "*boundary layer fence*" which consists of a sheet-metal wall placed on the suction side in the forward portion of the wing, as shown in figure 12, thus preventing cross-flow.

Figure 13: Swept-back wings aeroplane (*De Havilland DH.110*).

2.2 Theory of stability of laminar flows

In order to explain, with accuracy, process of transition characterizing crossflow boundary layer hereafter, a theoretically investigation, relating to stability, is introduced: the THEORY OF STABILITY OF LAMINAR FLOWS.

The theory is hased on the assumption that laminar flows are affected by certain small disturbances, which, in the case of a boundary layer on a solid body placed in a stream, may be due to wall roughness or to irrogularities in the external flow, as seen before. The theory endeavours to follow up in time the behaviour of such disturbances when they are superimposed on the main flow, that is the "*base flow*", bearing in mind that their exact form still remains to be determined in particular cases. The focal point of the theory is the potential decadence of disturbances: if they decay with time, the main flow is considered stable; on the other hand, if the disturbances increase with time the flow is considered unstable and there is the possibility of transition to a turbulent field.

In order to establish, indeed, the *Reynolds-number critical value*, at which turbulent transiton occurs for a certain base flow, *theory of stability* has been developed.

2.2.1 Method of small disturbances

As countered in the last paragraph , the STABILITY THEORY base on introducing small disturbances inside a flow, caused by several potential triggering factors. The theory of stability of Iaminar flows decomposes the motion into a "*base flow*", whose stability constitutes the subject of the investigation, and into a "*disturbed flow*" superimposed on it.

Let the base flow, which may be regarded as steady, be described by its Cartesian velocity components U, V, W and its pressure P. The corresponding quantities for the non-steady disturbance, instead, will be denoted by u', v', w' and p'. Hence, in the resultant motion, caused by the superimposition of two fields, the velocity components are:

$$u = U + u', \qquad v = V + v', \qquad w = W + w'$$

while the pressure results:

$$p = P + p'$$

the quantities related to the disturbance are small compared with the corresponding quantities of the base flow.

The investigation of the stability of such a disturbed can he carried out with the small disturbances method, which analyzes, through appropriate differential equations, the manner in which flows develop in the flow.

It shall be now considered a two-dimensional incompressible mean flow and an equally two-dimensional diaturbance. The resulting motion, described by equations above, satisfies the two-dimensional form of the Navier-Stokes equations. The problem shall be further simplified by stipulating that the mean velocity U depends only on y, resulting $U = U(y)$, whereas the remaining two components are supposed to be zero everywhere. Such an assumption can also be made because the dependence of the velocity U in the main flow on the z-coordinnte is very much smaller than that on y, in analogy with the case of *parallel flows*. As far as the pressure in the main flow is concerned, it is necessary to assume a dependence on x as well as on y, that is $P = P(x, y)$, because the pressure gradient $\partial P / \partial x$ maintains the flow. Thus a base flow can be assumed with:

$$U(y), \qquad V \equiv W \equiv 0, \qquad P(x, y)$$

Upon tho mean flow is assumed superimposed a two-dimensional disturbance which is a function of time and space. Its velocity components and pressure are, respectively:

$$u'(x, y, t), \qquad v'(x, y, t), \qquad p'(x, y, t)$$

35

Hence the resultant motion is described by:

$$u = U + u', \quad v = v', \quad w = 0, \quad p = P + p'$$

It is assumed that the base flow is a solution of the Navier-Stokes equations, and it is required that the resultant motion must also satisfy these equations. The superimposed fluctuating velocities, moreover, are taken to be "*small*" in the sense that all quadratic terms in the fluctuating components may be neglected with respect to the linear terms.

Now, the task of the stability theory consists in determining whether the disturbance is amplified or whether it decays for a given mean motion and, therefore, the flow is considered unstuble or stable depending respectively.

Substituting motion equations into the Navier-Stokos equations for a two-dimensional, incompressible, non-steady flow, and neglecting quadratic terms in the disturbance velocity components, it is obtained:

$$
\begin{cases}
\frac{\partial u'}{\partial t} + U\frac{\partial u'}{\partial x} + v'\frac{\partial U}{\partial y} + \frac{1}{\varrho}\frac{\partial P}{\partial x} + \frac{1}{\varrho}\frac{\partial p'}{\partial x} = \nu\left(\frac{\partial^2 U}{\partial y^2} + \nabla^2 u'\right) \\
\frac{\partial v'}{\partial t} + U\frac{\partial v'}{\partial x} + \frac{1}{\varrho}\frac{\partial P}{\partial y} + \frac{1}{\varrho}\frac{\partial p'}{\partial y} = \nu\nabla^2 v' \\
\frac{\partial u'}{\partial x} + \frac{\partial v'}{\partial y} = 0
\end{cases}
$$

where ∇^2 denots the *Laplacian operator*: $\partial^2/\partial x^2 + \partial^2/\partial y^2$.

If it is considered that the base flow itself satisfies the Navier-Stokes equations, the above equations can be simplified to:

$$
\begin{cases}
\frac{\partial u'}{\partial t} + U\frac{\partial u'}{\partial x} + v'\frac{\partial U}{\partial y} + \frac{1}{\varrho}\frac{\partial p'}{\partial x} = \nu\nabla^2 u' \\
\frac{\partial v'}{\partial t} + U\frac{\partial v'}{\partial x} + \frac{1}{\varrho}\frac{\partial p'}{\partial y} = \nu\nabla^2 v' \\
\frac{\partial u'}{\partial x} + \frac{\partial v'}{\partial y} = 0
\end{cases}
$$

Three equal.ions for u', v' and p' are obtained. The boundary conditions specify that the turbulent velocity components u' and v' vanish on the walls (*no-slip condition*).

36

2.2.2   The Orr-Sommerfeld equation

In order to achieve a stability analysis of flow through the stability theory, it is necessary to apply a method based on the use of the *Orr-Sommerfeld equation*. Hereafter, the procedure requested to achieve this formulation is shown.

The base laminar flow in the x direction with a velocity $U(y)$ is assumed to be influenced by a disturbance which is composed of a number of discrete partial fluctuations, each of which is said to consist of a wave which is propagated in the x direction. As it has already been assumed that the perturbation is two-dimensional, it is possible to introduce a *stream function $\psi(x, y, t)$* thus integrating the *equation of continuity*. The stream function representing a single oscillation of the disturbance is assumed to be of the form:

$$\psi(x, y, t) = \phi(y)e^{i(\alpha x - \beta t)}$$

Any arbitrary two-dimensional disturbance is assumed expanded in a Fourier series and each of its terms represents such a partial oscillation. In equation above, α is a real quantity and $\lambda = {}^{2\pi}/_{\alpha}$ is the wavelength of the disturbance, while the quantity β is complex:

$$\beta = \beta_r + i\beta_i$$

where β_r is the *circular frequency* of the partial oscillation, whereas β_i, *amplification factor*, determines the degree of amplification or damping. The disturbances are damped, as said before, if $\beta_i < 0$ and consequently the laminar mean flow is stable. If $\beta_i > 0$ instability sets in. Apart from α and β it is convenient to introduce their ratio:

$$c = \frac{\beta}{\alpha} = c_r + ic_i$$

Here c_r denotes the velocity of propagation of the wave in the x direction, that is *phase velocity*, whereas c_i again determines the *degree of damping*, or amplification,

depending on sign it presents. The *amplitude function, ϕ,* of the fluctuation is assumed to depend on y only, because the mean flow depends on this coordinate alone.

Perturbation velocity components can be now achieved with respect to this amplitude function:

$$\begin{cases} u' = \frac{\partial \psi}{\partial y} = \phi'(y)e^{i(\alpha x - \beta t)} \\ v' = -\frac{\partial \psi}{\partial x} = -i\alpha\phi(y)e^{i(\alpha x - \beta t)} \end{cases}$$

Introducing these values into Navier-Stokes equations, it is obtained, after the elimination of pressure, the following, ordinary, fourth-order, differential equation for the amplitude $\phi(y)$:

$$(U - c)(\phi'' - \alpha^2\phi) - U''\phi = -\frac{i}{\alpha R}(\phi'''' - 2\alpha^2\phi'' + \alpha^4\phi)$$

This is the fundamental *differential equation for the disturbance* or *stability equation* which forms the point, of departure for the stability theory of laminar flows. It is commonly referred to as the *Orr-Sommerfeld equation* and it has been cast in dimensionless form. All lengths have been divided by a suitable reference length or boundary-layer thickness δ, while velocities have been divided by the maximum velocity U_{max} of the base flow. Reynolds number, which is a characteristic of the mean flow, in this case results:

$$Re = \frac{U_{max}\delta}{\nu}$$

whose *boundary conditions* are:

$$\begin{cases} u' = v' = 0: \quad \phi = 0, \quad \phi' = 0 \quad \text{ per } y = 0 \\ u' = v' = 0: \quad \phi = 0, \quad \phi' = 0 \quad \text{ per } y = \infty. \end{cases}$$

in order to nullify perturbation velocity components at wall.

It is possible to note that disturbances superimposed on a two-dimensional flow

pattern need not to be two-dimensional, if a complete analysis of the question of stability is to be achieved. Thanks to *Squire theorem* it can be proved that, by assuming disturbances which are periodic in the z-direction, a two-dimensional flow pattern becomes unstable at a higher Reynolds numbers when the disturbance is assumed three-dimonsional than when it is supposed to be two-dimensional. So this approach become "*conservative*". The two-dimensional disturbances are "more dangerous" than three-dimensional flows and lower stability limit of the flow.

2.2.3 The eigenvalue problem

The problem of stability has now been reduced to an *eigenvalue problem* of the Orr-Sommerfeld equation with the boundary conditions defined in previous section (2.2.2). When the mean flow $U(y)$ is specified, Orr-Sommerfeld equation contains four parameters, namely α, Re, c_r and c_i. Of these the Reynolds number is specified and the wavelength, $\lambda = {}^{2\pi}/\alpha$, of the disturbance is to be considered given. In this case the differential equation , together with the boundary conditions, furnish one eigenfunction $\phi(y)$ and one complex eigenvalue $c = c_r + ic_i$, for each pair of values α and Re. As said before, the sign of c_i determines whether the wave is amplified ($c_i > 0$) or damped ($c_i < 0$). For $c_i < 0$, the corresponding flow (U, Re) is stable for the given value of α, whereas $c_i > 0$ denotes instability condition. The limiting case $c_i = 0$ corresponds to *neutral disturbances*.

The result of such an analysis, for a prescribed laminar flow $U(y)$, can be representod graphically in an $\alpha - Re$ diagram, as in figure 14, because every point, of this plane corresponds to a pair of values of c_r and c_i.
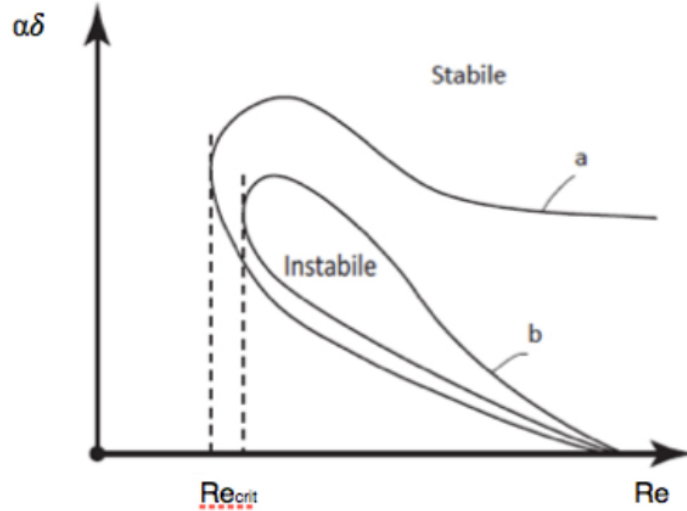
Figure 14: Curves of neutral stability for a two-dimensional boundary layer with two-dimensional disturbances, on $\alpha - Re$ diagram, represented for a *non-viscous* (a) and a *viscous* (b) flow [3].

In particular, the locus $c_i = 0$ separtes the region of stable from that of unstable disturbances and is called the *curve of neutral stability*. The point on this curve at which the Reynolds number present its smallest value (tangent parallel to the α-axis) indicates that value of the Reynolds number below which all individual oscillations decay, whereas above that value at least some are amplified. This smallest Reynolds number is the *critical Reynolds number* or *limit of stability* with respect to the type of laminar flow under cousideration.

The experimental evidence concerning transition from laminar to turbulent flow leads us to expect that, at small Reynolds numbers for which laminar flow is observed, all wavelengths would produce only sltable disturbances, whereas at large Reynolds numbers, for which turbulent flow is observed, unstable disturbauces ought to correspond to at least some wavelengths.

However, it is necessary to remark, at this point, that the critical Reynolds number calculated from stability considerations cannot be expected to be equal to

the Reynolds observed at the point of transition. If attention is fixed on the flow in the boundary layer along a wall, then *theoretical critical Reynolds number* indicates the point on the wall at which amplification of some individual disturbances begins and proceeds downstream of it. The transformation of such amplified disturbances into turbulence takes up some time and the unstable disturbances have a chance to travel some distance in the downstream direction, inside the boundary layer. It must, therefore, be expected that, the observed position of the point of transition will be downstream of the calculated, theoretical limit of stability, or, in other words, that the experimental critical Reynolds number execeds its theoretical value. In order to distinguish between these two values, it is usual to call the theoretical critical Reynolds number the "*point of instability*", whereas the experimental critical Reynolds number is called the "*point of transition*".

2.3 Three-dimensional flows instability

Up to this point, 2D flows stability with two-dimensional disturbances has been discussed. These flows, as explained, result the most unstable and then lead to a more conservative evaluation of stability. The experimental evidence also shows that transition is started as a result of the amplification of two-dimensional disturbances. It also turned out that the amplification of the unstable plane waves produces a distinctly three-dimensional flow structure. After the amplitude of the wave has reached a certain magnitude, there sets in a period of strong and non-linear amplification of the disturbance. This process is accompanied by a *transfer of energy* in the transverse direction and this distorts the original, two-dimensional character of the base flow. Thus, the *breakdown of laminar flow* and, hence, the *birth of turbulence* appear to be a consequence of the development of the unstable disturbances in three dimensions. This is accompanied by the appearance to a certain extent in the boundary layer too, of *vortices* whose axes lie in the direction of the flow.

In this section, crossflow instability linked phenomenology will be investigated and the consequent propagation of such vortices [4].

Transition to turbulence in swept-wing flows has resisted correlation with LINEAR THEORY because of its sensitivity to freestream conditions and 3-D roughness and because one of the principal *instability modes* quickly becomes non-linear.

The basic idea is that the combination of sweep and chordwise pressure gradient within the boundary layer creates a velocity component orthogonal to the inviscid streamline (base flow). This crossflow profile is *inflectional* and exhibits both *traveling* and *stationary unstable waves* called CROSSFLOW VORTICES that are approximately aligned along the inviscid streamlines. Under conditions of low freestream turbulence levels, the dominant crossflow wave is stationary, while moderate to high turbulence levels initiate dominant traveling waves. The mechanism is relatively insensitive to sound and 2-D surface roughness but very sensitive to 3-D roughness near the attachment line.

Although, the v' and w' components of the disturbances are very small, by convecting streamwise momentum in the wall-normal direction, they produce remarkable changes in u'. Thus the mean flow is highly distorted with localized inflection points. Transition is then triggered by a high-frequency secondary instability of the distorted mean profile.

Transition, therefore, is now triggered by an high frequency secondary instability of the inflectional mean profile, as it is shown in figure 15. One can notice, from this figure, that, because the crossflow velocity must vanish at the wall and at the edge of the boundary layer, an *inflection point* exists and provides a source of an inviscid instability. The instability appears as co-rotating vortices whose axes are aligned to within a few degrees of the local inviscid streamlines.
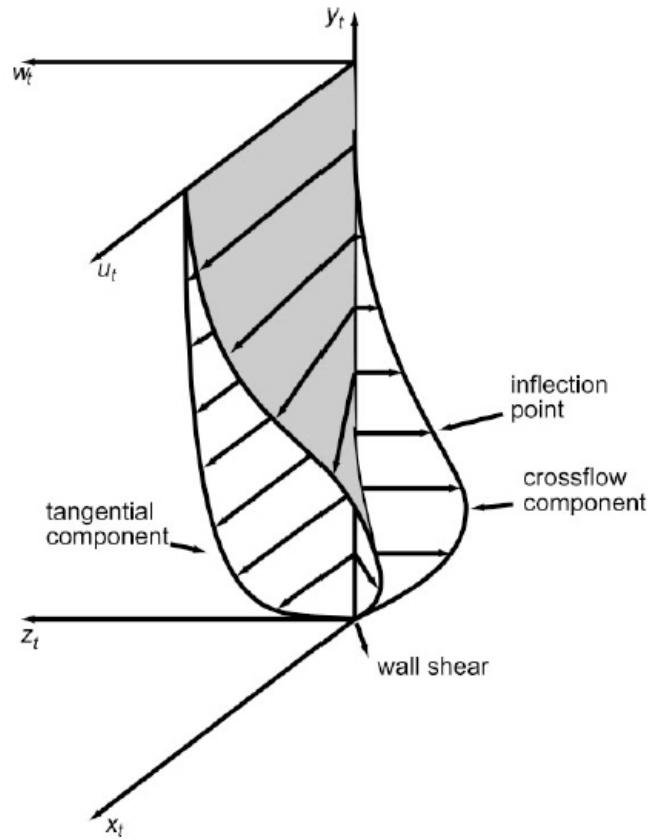
Figure 15: Crossflow boundary layer velocity contour with *inflection point* and *resultant velocity contour*, caused by the combination of transversal and streamwise components [5].

The study of three-dimensional boundary layers is motivated by the need to understand the fundamental instability mechanisms that cause transition in swept-wing flows. Research has identified four types of instabilities for these flows, which are listed below.

- The *attachment-line problem* is caused by a basic instability of the attachment-line boundary layer or by its contamination with turbulent disturbances and develops, in general, on swept wings with a large leading edge radius.

- The streamwise instability is not unlike the familiar *Tollmien-Schlichting wave* (TS) in two-dimensional flows, shown in figure 16. This mechanism is associated with the chordwise velocity component and is generally stabilized by a favorable pressure gradient.
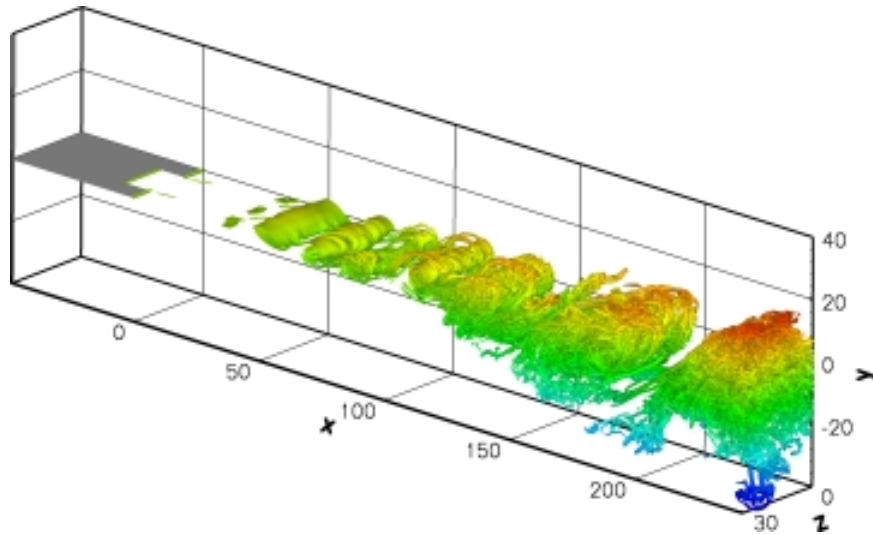
Figure 16: Tollmien-Schlichting (TS) waves.

- *Centrifugal instabilities* can appear over concave regions on the surface and result in the development of *Görtler vortices* (figure 17).
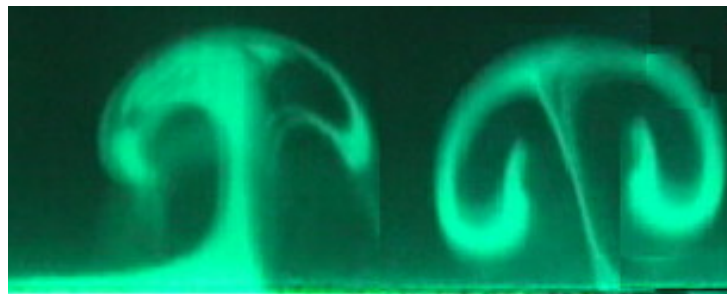
Figure 17: *Görtler vortices* visualization inside the boundary layer.

- *Crossflow waves* are an inviscid instability mechanism caused by the combined effect of wing sweep and pressure gradient.

All of these instabilities can appear individually or together depending on the combination of Reynolds number, wall curvature, wing sweep, pressure gradient, and external disturbances.

2.3.1   Crossflow primary instability

The crossflow instability that occurs on swept wings in regions of strong, favorable pressure gradient. The phenomenon overview is very useful, for proceeding of the thesis, in order to set flow field and conditions in which next chapters analysis will take place.

Unlike TS instability, the *crossflow problem* exhibits "*stationary*" ($f = 0$) as well as "*traveling disturbances*" that are amplified. Even though both types of waves are present in typical swept wing flows, transition is usually dominated by either the stationary or the traveling waves. LINEAR THEORY predicts that the traveling disturbances are more highly amplified, however many experiments are dominated by stationary waves. Whether the stationary or traveling waves dominate is directly related to the *receptivity process*, as said in section 1.4 yet. Stationary waves dominate transition in low-disturbance environments, while traveling waves are more important in high-disturbance environments. For the last case, linear theory makes the crossflow waves behavior explicit, while, for the first one, the mean flow is distorted and quickly reach a non-linear behavior, such as the linear analysis become inadequate. Since the low-disturbance environment is more characteristic of flight, the stationary waves are expected to be more important.

As far as the receptivity process is concerned, it could be explained through the description of factors that strongly affect the occurence of such a phenomenon [5]:

- ROLE OF FREESTREAM FLUCTUATIONS, that is the effect of freestream turbulence on crossflow transition. Turbulence intensities about $Tu > 0,0015$ produced transition behavior dominated by traveling waves. for increased turbulence levels where traveling waves dominate but the turbulence intensity is not too high, $0,0015 < Tu < 0,0020$, transition was actually delayed relative to low-turbulence cases at the same Reynolds number. The explanation for this is that the traveling waves excited by the increased freestream turbulence were sufficiently strong to prevent stationary waves from causing transition but were not strong enough to cause transition as quickly as the stationary waves they replaced.

- ROLE OF SURFACE ROUGHNESS, that is the receptivity mechanism for the stationary vortices that are important for transition in environments with very-low-amplitude turbulent fluctuations.

- ROLE OF TURBULENCE/ROUGHNESS INTERACTIONS, that is the receptivity of freestream turbulence interacting with surface roughness. It is to take in account that turbulent fluctuations play a much more significant role in the transition process than acoustic fluctuations. Stationary waves dominate transition, but when the roughness array is activated, the saw-tooth transition front is replaced by a diffuse spanwise transition front indicative of traveling waves dominated transition. Traveling waves do result from an interaction of freestream velocity fluctuations with surface roughness and not from turbulence intensity alone.

The rotational components of stationary crossflow waves are typically very weak, hence analytical models have long been based on linear theory. However, experiments often show evidence of strong nonlinear effects. The resolution of this apparent paradox lies in the understanding of the physical mechanism by which the stationary waves disturb the boundary layer. The key to the stationary disturbance is that the wave fronts are fixed with respect to the model and nearly aligned with the

46

potential-flow direction (the wavenumber vector is nearly orthogonal to the inviscid streamline). Consequently, although the rotational motion of the wave is weak, its stationary nature produces an *integrated effect* that causes a strong streamwise distortion in the streamwise boundary-layer profile. This integrated effect and the resulting local distortion of the mean boundary layer leads to the modification of the basic state and the early development of non-linear effects.

An interesting feature of the stationary crossflow waves, which will be explained in the next section, is the destabilization of *secondary instabilities*. The streamwise distortions created by the stationary wave are time-independent, resulting in a spanwise modulation of the mean streamwise velocity profile. As the distortions grow, the boundary layer develops an alternating pattern of accelerated, decelerated, and doubly inflected profiles. The inflected profiles are "inviscidly unstable", and as such, are subject to a high-frequency secondary instability. This *secondary instability* is highly amplified and leads to rapid *local breakdown*. Because transition develops locally, the transition front is nonuniform in span and characterized by a *saw-tooth* pattern of turbulent wedges, as represented in figure 18.
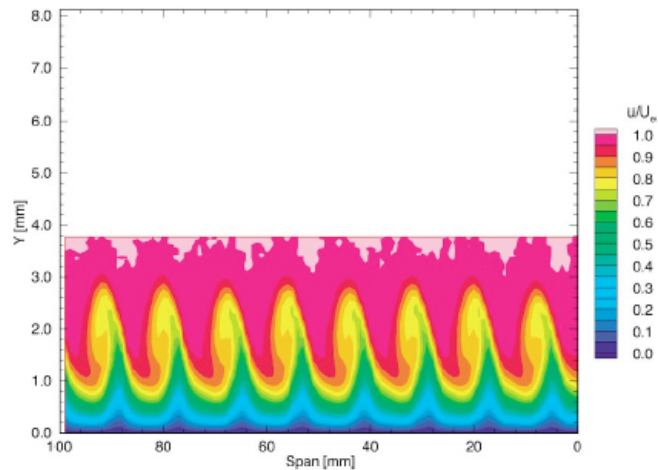
Figure 18: Transition front characterized by a *saw-tooth* characteristic pattern of turbulent wedges, along the spanwise direction [5].

2.3.2 Absolute instabilty

In this paragraph, the link between *rotating disk* and crossflow boundary layers are highlighted in order to present the *absolute instability concept*.

The boundary layer on the surface of a rotating disk, shown in figure 19, can be used as a model problem for swept wing flow because the velocity profiles on the disk provide a basic state and stability behavior very similar to that of the swept wing boundary layer. The advantage of the rotating disk is the existence of a well-known similarity solution for the basic flow that features a boundary layer of constant thickness.
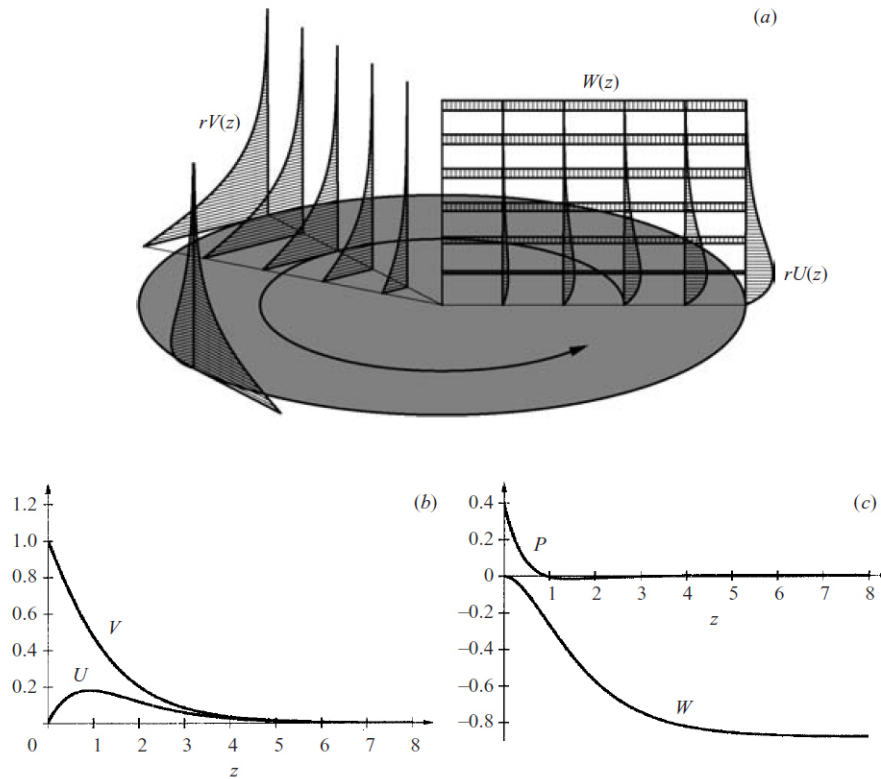
Figure 19: Rotating disk boundary layer (a), velocity and pressure profiles along z coordinate (b, c).

The most important recent development in the study of the rotating-disk problem is the THEORY OF LINGWOOD, which state that rotating-disk boundary layers support an absolute instability at $Re = 510$. The implication of this finding is that the steady, laminar basic state cannot exist beyond this Reynolds number regardless of the care taken in preparing and conducting each numerical simulation of such a flow field. Basing on this criterion, indeed, suitable Reynolds numbers will be choose, up ahead, in order to best simulate crossflow boundary layer, strictly linked, as said yet, with the rotating disk problem. This finding is in good agreement with various rotating disk experiments, most of which do not maintain laminar flow much beyond $Re = 500$.

Lingwood follow *Briggs method*, which prescribes the means to evaluate the *Fourier-Laplace integral* that arises from considering an initial-boundary-value problem for impulsive forcing in a developing flow. If the group velocity of a disturbance wave packet goes to zero while the temporal growth rate is positive, then the flow is absolutely unstable. Lingwood applied Briggs method by using a parallel-flow approximation and observed a pinch between two neutral branches of the dispersion relationship that yields a positive temporal growth rate at a Reynolds number $Re \geq 510,625$. As Re is increased, the absolutely unstable wave-number range expands and, at large Reynolds numbers, tends toward the limits found for the inviscid case.

The absolute instability then arises from an inviscid mechanism and that the good correlation between the Reynolds number limit for absolute instability, indicated by Lingwood, and the experimental transition Reynolds numbers makes a case for transition being triggered by the absolute instability.

Moreover, studies about rotating disk instabilities includes a number of routes to turbulence. First, high-amplitude traveling disturbances may be amplified at very low Reynolds numbers, while at higher Reynolds numbers stationary waves dominate, as it has been said before. If the disturbance levels are high, then high-frequency secondary instabilities lead to rapid transition. On the other hand, if disturbance levels are low and secondary instabilities do not appear, the flow becomes absolutely

unstable for Reynolds numbers above $Re = 510$, and transition occurs.

2.3.3 Primary instability development in the crossflow boundary layer

In this paragraph, the flow evolution, characterized by instability, inside crossflow boundary layer, is going to be analyzed, graphically and on a quality level, gradually introducing several aspects which affect flow development [4].

Natural roughness   In the absence of artificial surface roughness, naturally occurring stationary crossflow waves are nonuniform in span due to submicron surface irregularities near the leading edge. This is shown in figure 20, which displays a contour plot of the normalized boundary-layer velocity at $x/c = 0,55$ for $Re = 2,4 \times 10^6$.
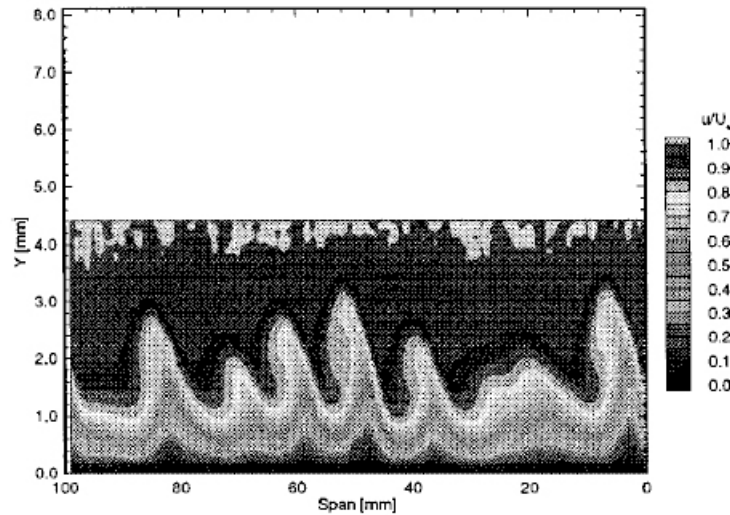
Figure 20: Contour plot of the normalized boundary-layer velocity u/U_e at $x/c = 0,55$ for $Re = 2,4 \times 10^6$, without surface roughness [4].

The figure shows that the streamwise velocity u/U_e, in the $Y - z$ plane. The flow is toward the reader and the stationary vortices are turning in the right-handed sense. The wave-like structure of figure 20 represents the integrated effect of the weak

50

stationary vortices on the streamwise velocity. It also displays a dominant feature at a $12\,mm$ spanwise spacing, which is approximately the most amplified stationary wavelength according to the *linear theory.*

Critical forcing Figure 23 shows the streamwise velocity contour with the roughness installed. The dominance of the $12\,mm$ mode is striking, and allows a direct calculation of the stationary disturbance amplitude.
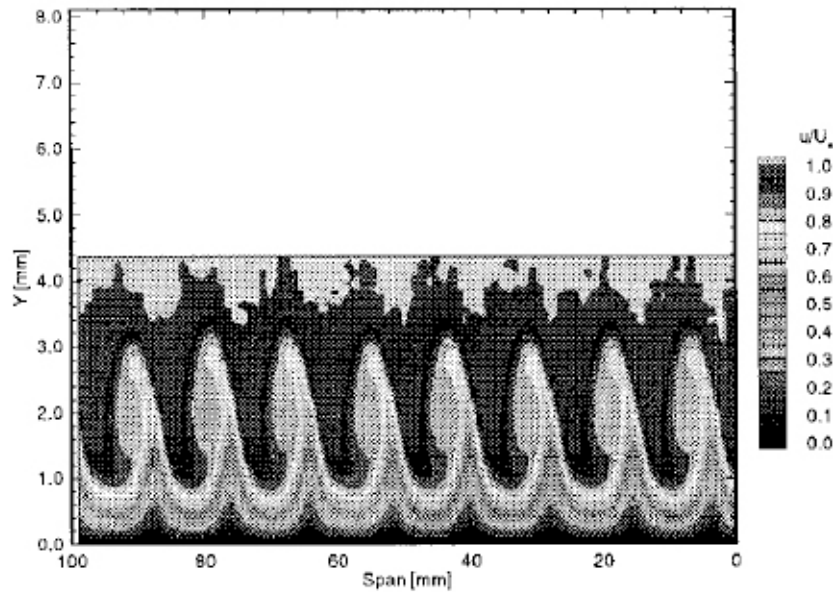
Figure 21: Contour plot of the normalized boundary-layer velocity u/U_e at $x/c = 0,45$, with artificial surface roughness installed [4].

Figure 22, instead, compares the experimental amplification factor, "*N-factor*", for the $12\,mm$ forcing with the predictions of the *OrrSommerfeld equation* (OSE), the *linear parabolized stability equations*, and the *full nonlinear parabolized stability equations.*

The early growth shows excellent agreement with linear PSE, however strong nonlinear effects develop well before transition at $(x/c)_{tr} = 0,52$. The importance of

nonparallel effects is indicated by the "failure" of traditional linear stability theory (OSE) to accurately predict the growth even in the linear range. When nonlinearity is added, the agreement is remarkable over the entire measurement region and all aspects of the growth are predicted. This correspondence is due to curvature inclusion in the computation problem. The sensitivity to very weak curvature is due to the strong stabilizing *Görtler effect* with convex curvature. This is the reason for the disagreement between the linear experiments and linear theory without curvature.
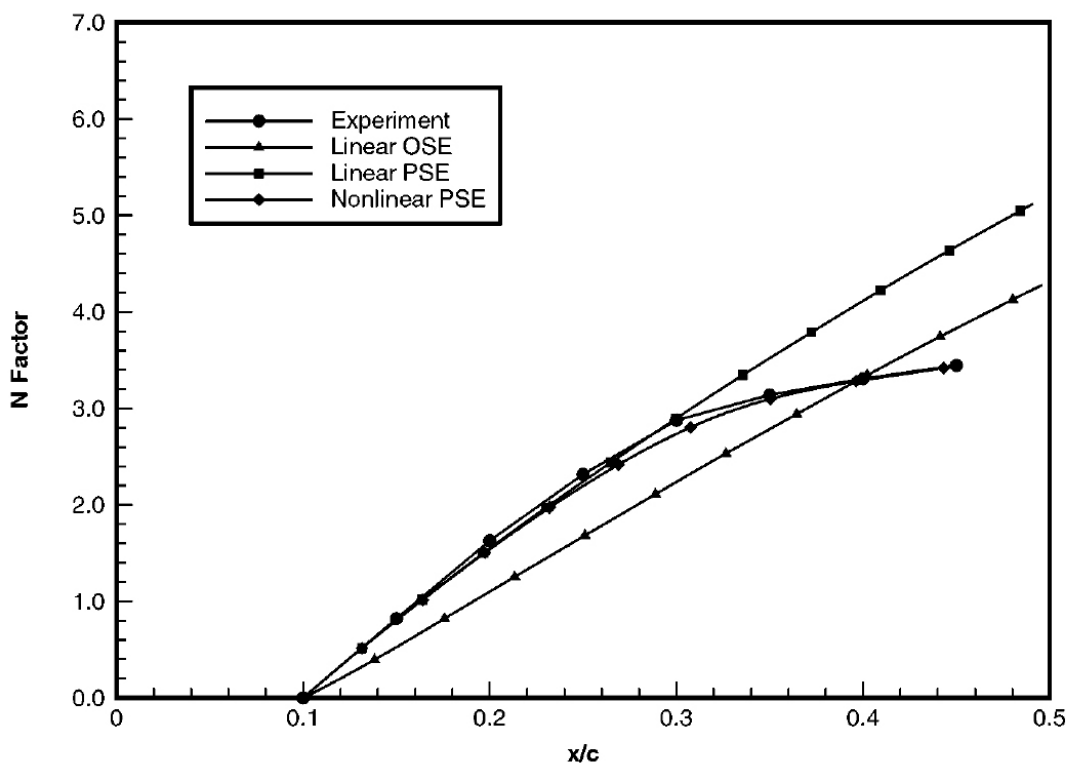
Figure 22: Measured and theoretichal amplification factors, *N-factor*, for the condition of figure 23 [5].

Role of spanwise spacing It was be noted that unstable waves occur only at integer multiples of the primary disturbance wavenumber. In other words, spacing

52

the roughness elements $12\,mm$ apart excites disturbances with spanwise wavelengths of $6\,mm$ and $4\,mm$.

As far as this statement is concerned, it is possible to continue with the wave front development qualitative description. Figure 23, instead, shows the normalized velocity profiles for $Re = 2,4 \times 10^6$, at $x/c = 0,40$. The $18\,mm$ spacing is observed with a very strong $9\,mm$ modulation.
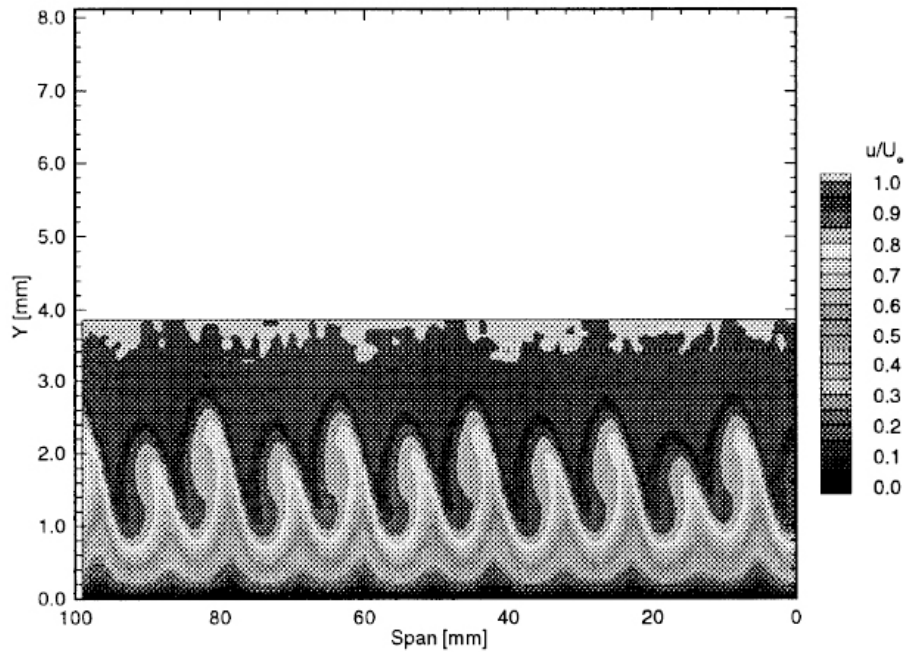
Figure 23: Contour plot of the normalized boundary-layer velocity u/U_e at $x/c = 0,40$, with artificial surface roughness installed and $k = 6\mu m$, at $18\,mm$ spacing [4].

Even at $x/c = 0,45$, the small artificial roughness yields boundary layer distortions that are very uniform and periodic is span. Boundary layer profiles from which the contour map of last figure is made are shown in figure 24, in order to give an approximate idea of the velocity trend in the considered ragion and to compare with next results.
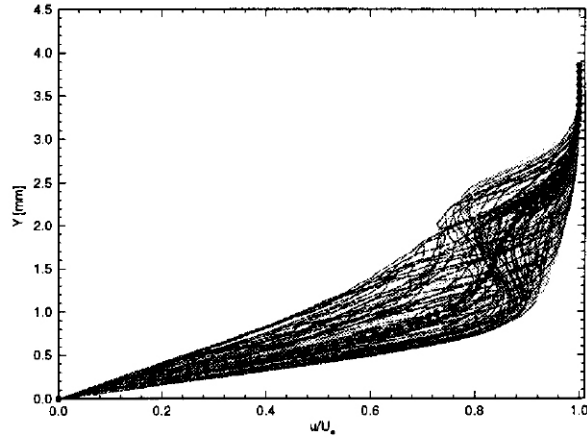
(a)
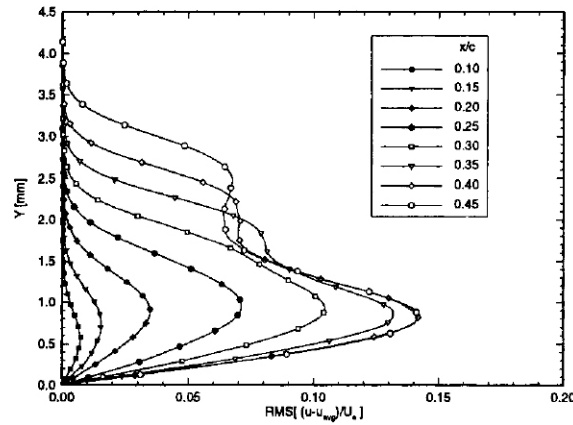
(b)

Figure 24: Spanwise array of 100 velocity profiles spaced $1\,mm$ apart at $x/c = 0, 40$ (a) and stationary crossflow mode shapes (b), at the same conditions of (a) [4].

In figure 24 (a) the mean profile is also shown and as with the no roughness case, the stationary disturbance has dramatically distorted the mean boundary layer. The

54

spanwise-average profile is doubly inflected even for $x/c \geq 0,30$. 24 (b) presents the *total disturbance mode* shape profiles for $x/c \geq 0,30$.

As far as *individual mode amplitude* is concerned, a full set of spanwise scans are presented to extract the modal content of the disturbance. The height scanned corresponds to the maximum of the total disturbance mode shape at each x/c. The power spectral density computations for these scans are computed. Integration of the peaks of these data are used to form figure 25.
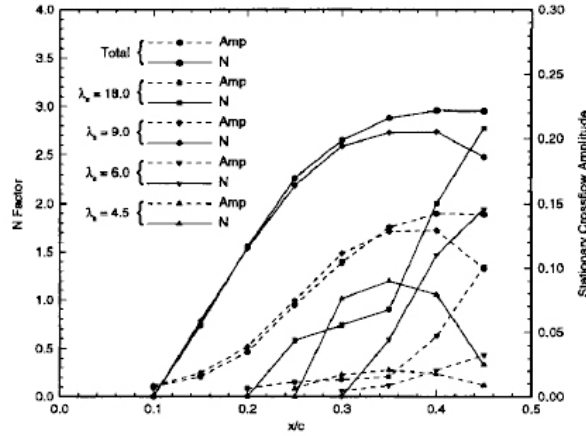
Figure 25: Total and single-mode disturbance amplitudes and "*N-factor*s", at conditions of figure 24 [4].

The spectrum at this location shows energy in the (0,2) mode, that is $\lambda_z = 9 \ mm$. It is interesting that the mode contains more energy than the *fundamental mode* for $\lambda_z = 18 \ mm$. The fundamental mode is not measurable until $x/c = 0,20$. Although the fundamental is detected, the first harmonic at $\lambda_z = 9 \ mm$ still contains most of the disturbance energy. The fundamental disturbance grows rapidly for $0,35 \leq x/c \leq 0,45$, where the (0,2) mode actually shows some decay. Higher harmonics become unstable for $x/c \geq 0,25$. The spectrum at $x/c = 0,45$ shows detectable disturbances for the (0,3) and (0,4) modes, at $\lambda_z = 6 \ mm$ and $\lambda_z = 4,5 \ mm$ respectively.

The (0,2) mode shows exponential growth up to $x/c = 0,25$, at which point the mode begins to *saturate*. It reaches a maximum amplitude of 13% at $x/c = 0,40$, after

which it decays. It is in this "saturation and decay region" where the fundamental disturbance shows strong growth. This is also the region of strong nonlinear effects as seen by the growth of the second lobe in the total disturbance mode-shape profiles in figure 24.

Normalized velocity profiles for $Re_c = 2,4 \times 10^6$ and roughness are shown in figure 26 for chord locations $x/c = 0,30$ (a) and $x/c = 0,60$ (b), respectively.

(a)

(b)
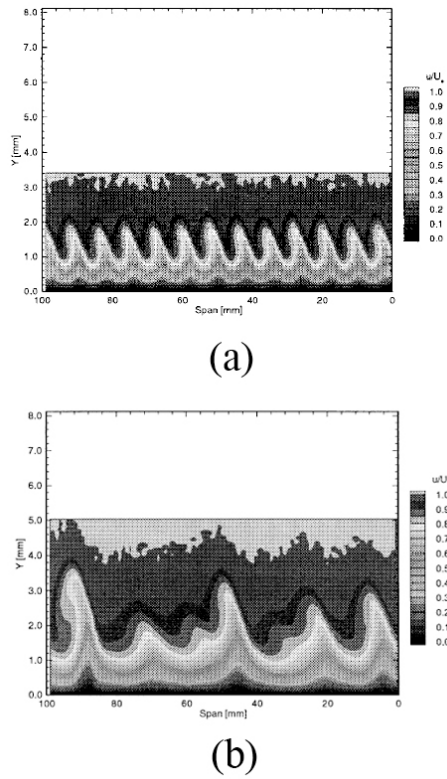
Figure 26: Streamwise velocity profiles at $x/c = 0,30$ (a) and $x/c = 0,60$ (b), for $Re_c = 2,4 \times 10^6$, $k = 6\mu m$, at 8 mm spacing [4].

The disturbance is first measurable at $x/c = 0,10$, and a very uniform and dominant $\lambda_z = 8$ mm mode develops for $0,10 \leq x/c \leq 0,25$. At $x/c = 0,30$ (a), although the contour plot still shows a dominant 8 mm mode, there is noticeable development

of some slight nonuniformity. This nonuniformity becomes more dramatic with increasing chord, and the 8 mm structure fades out in favor of some longer wavelength disturbances. By $x/c = 0, 50$, the dominance of the fundamental mode is gone, while $x/c = 0, 60$ (b) the fundamental mode is indistinguishable in the velocity profiles.

The total disturbance amplitude, *N-factors*, computed from the mode shapes show that the total disturbance grows rapidly from $0, 10 \leq x/c \leq 0, 30$, at which point the amplitude saturates and then slows strong decay. At $x/c = 0, 30$, the second lobe high in the mode shape is evident, indicating strong nonlinear effects. The amplitude continues to decay up to $x/c \leq 0, 45$, where the amplitude levels off and then shows a second region of strong growth for $0, 50 \leq x/c \leq 0, 60$.

In short, considered Reynolds number and roughness delays transition past that of the natural roughness case. Strong early growth of the 8 mm mode effectively suppresses initial growth of the very unstable 9 mm and 12 mm near the leading edge, which the linear stability theory predicts to be the region where these modes have the largest growth rates. Moreover, the dramatic decay allows for longerwavelength background disturbances to become unstableb due to submicron surface irregularities. The growth of these longer wavelength broadband disturbances eventually leads to transition.

2.3.4 Secondary instability

After the process, leading to primary instability, has been fully described in last paragraphs, the process by which the saturated vortices produced by this instability "*break down*" and lead to *turbulence* will be well-documented in this section [6, 7].

What is observed in stationary-wave-dominated transition experiments is that, at some point aft of where the vortices saturate, breakdown to turbulence occurs very rapidly along a jagged front. These studies suggest that the final stage of transition occurs over a very short streamwise distance and that turbulence originates at fixed, distinct points in the boundary layer from which it spreads in a characteristic wedge pattern.

In order to describe *saturated-vortex breakdown* is that the distorted mean flow produced by these vortices includes very strong and *inflectional shear layers* and thus becomes unstable to secondary instabilities. These instabilities grow to large amplitudes over a very short streamwise distance and lead to breakdown and turbulence.

The crossflow velocity profile $w_s(y)$ is inflectional and causes a strong primary spatial instability of the flow with respect to so-called crossflow eigenmodes, which can be steady or unsteady. In physical space, strong *co-rotating vortices* are formed with their axes oriented approximately along the outer streamline. As said before, upon downstream vortex saturation, the mean flow is deformed resulting in the formation of strong shear layers, which are connected to local wall-normal and crosswise inflectional mean profiles $u_s(y)$ and $u_s(z)$. They trigger a convective high-frequency *secondary instability* with explosive spatial growth of unsteady modes. The frequency of the most amplified secondary mode is about one order of magnitude higher than the frequency of the most amplified primary crossflow mode.

These instabilities are localized in physical space and they move focused along the primary vortical structure. They appear mostly in the low-momentum upwelling region, where especially the spanwise gradients in the meanflow become extreme. The growth of these secondary instabilities is connected to the appearance of *secondary*

finger-vortices twining around the crossflow vortices from their upward moving side. This phenomenon is graphically shown in figure 27. The final breakdown by *tertiary vortices* in between the secondary finger vortices.
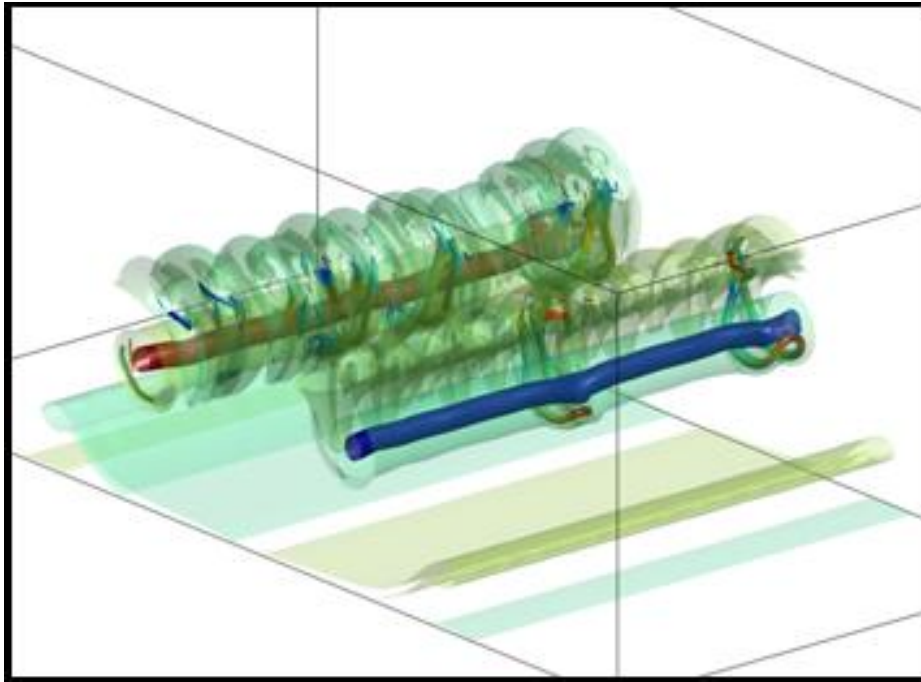
Figure 27: *Secondary finger-vortices* wrapped around the crossflow primary vortices.

Principally, three different classes of secondary instability mode were identified, which are listed below.

- The high-frequency "*mode I*" or "*z*" mode, induced by the minimum of the spanwise gradient of the streamwise velocity component $(\partial U/\partial z)$; this mode seems to be most important;

- the high-frequency *mode II* or *y* mode, induced by the local maximum of the wall-normal gradient $(\partial U/\partial y)$;

- the low-frequency *mode III*, most probably linked to the maximum of the spanwise gradient.

The modes exhibit their amplitude maxima in the respective regions of the deformed three-dimensional mean flow. For istance, the most amplified z mode is located at the updraft crossflow vortex side, and the y mode on top of the vortex. The weaker amplified "*mode-III*" class is found under the vortex close to the wall.

Moreover, in another series of experiments, the secondary instability was observed in boundary layers in which a combination of travelling and stationary primary disturbances was forced by variable leading edge roughness. The secondary-instability fluctuations were only observed for certain combinations of the travelling and stationary primary waves, suggesting that under some conditions neither the stationary nor travelling primary-instability waves are sufficiently strong to destabilize the secondary instability, but that superposition of both is capable of producing sufficient mean-flow deformation to destabilize the secondary instability for certain phase ranges of the superposition.

Such a non-linear interaction can generates vortical interaction structures that lead the transitional process before some kind of known secondary instabilities come into play. Moreover, one can notice, at clean conditions, that an unsteady pure single crossflow wave cannot lead to transition because it generates only non-zero diagonal elements in the frequency spanwise wavenumber space.

Growth rates of a secondary instability induced by travelling primary crossflow waves on a swept cylinder have been calculated, as described in section 2.1.1, using secondary instability analysis in a reference frame moving with the spanwise phase speed of the primary wave. They found the rates twice as high as in the case with steady primary disturbances, and at somewhat lower frequencies, but did not further analyse this finding because in the corresponding experiment the frequency of the secondary instability connected to the steady primary vortices dominated.

2.3.5 Secondary instability development in the crossflow boundary layer

In analogy with section 2.3.3, in this paragraph, secondary-instability spatial evolution inside crossflow boundary layer is described, for $Re_c = 2, 4 \times 10^6$ and with

roughness installed, in order to give a qualitative idea of the phenomenon described in last paragraph.

The first measurement station is at $x/c = 0,30$, which is the first position for which the quantity $\partial U/\partial y$ equals zero somewhere inside the boundary layer, indicating that significant mean-flow distortion has developed. Figure 28 shows a collection of meanflow velocity profiles (a) and the spanwise mean of the individual profiles (b).
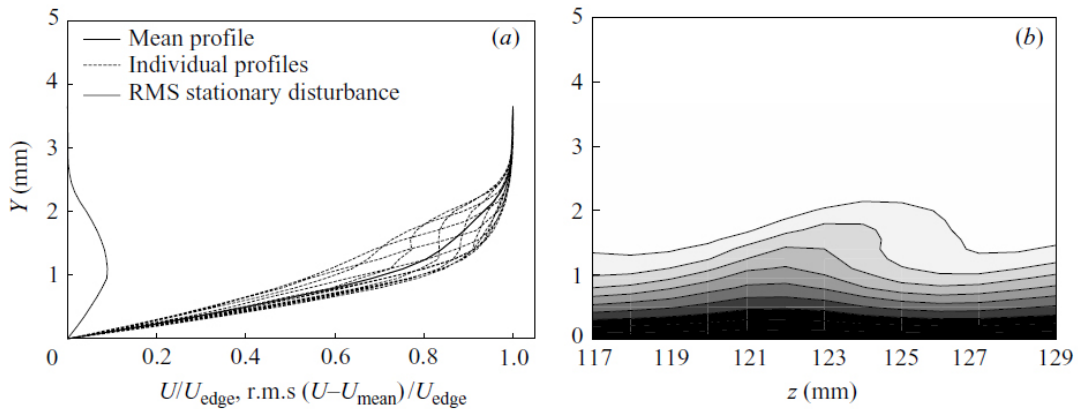
Figure 28: meanflow velocity profiles (a) and the spanwise mean of the individual profiles (b) [6].

The curve, represented by the continuous line, idetifies the *root mean square* (r.m.s.) of stationary mode disturbance (a). For this condition, although there is some distortion of the mean flow, the disturbance evolution may still be consistent with *linear stability theory* because the r.m.s. curve has not yet developed the upper lobe that accompanies the advent of significant nonlinearities. The development of an upper lobe is due to the rollover phenomenon that brings low-momentum fluid into the upper part of the boundary layer signalling the onset of significant mean-flow distortion, and hence, nonlinear disturbance evolution. In figure righten-side (b), dark shades are low-momentum regions, while light shades are high-momentum regions.
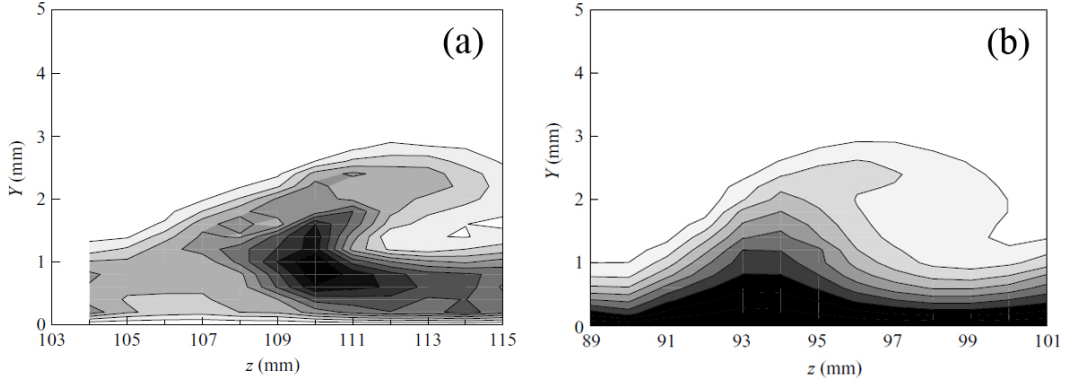
Figure 29: Velocity-fluctuation r.m.s. distribution at $x/c = 0,35$ (a) and mean-flow velocity profiles (U/U_∞) at $x/c = 0,40$ (b) [6].

In figure 30 it can be noted that, moving to $x/c = 0,35$, the earliest stage of non-linear evolution is apparent in the mean flow. Both figure (a) and figure (b) show that overturning of the low-momentum upwelling is well under way. Figure (a) shows that travelling-wave fluctuations are strongly modulated due to an interaction with the stationary disturbance. The modulation is simply a result of the nonlinear interaction of the stationary and travelling disturbances that becomes more pronounced as the disturbance amplitudes increase. In figure (b), instead, stationary-mode amplitude is substantially increased.

As far as the spatial distribution of the $3\,kHz$ fluctuations is concerned, figure 30 shows that these fluctuations lie along the shear layer to the left of the upwelling region and extend over much of the span of the stationary structure. The high frequencies represent a secondary instability in the strictest sense because neither the high-frequency band nor the spatial location at which the fluctuations exist are associated with an instability of the undistorted mean flow.

Because the secondary instability is situated where it is, aligned on the high-velocity shear layer along the left edge of the low-momentum upwelling, it appears that this is an inviscid, inflection-point-driven instability. As such it is manifested as vortex lines that lie in the (y, z) plane and convect in the stream direction.

62
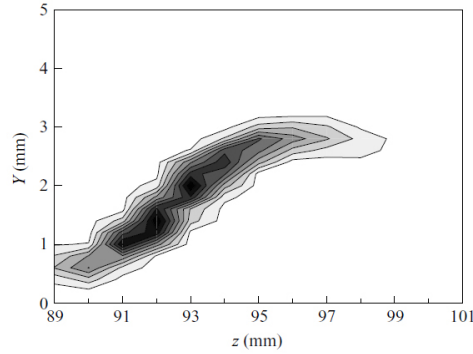
Figure 30: High frequency velocity-fluctuation r.m.s. at $x/c = 0, 40$ [6].

A visual representation of secondary instability can be achieve through rolls that wrap along the left side of and extend above the stationary structure, as shown in figure 31.
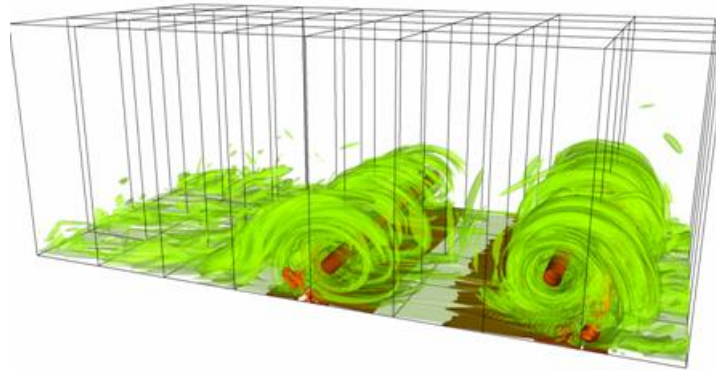
Figure 31: Visual representation of *secondary instability*.

Proceeding streamwise, up to $x/c = 0, 45$, the fluctuation spectra show that the $3\,kHz$ and $6, 1\,kHz$ modes continue to grow rapidly, closer to half the span locations participating. The spatial distribution of the $6, 1\,kHz$ lies clearly along the shear layer to the left of the low-momentum upwelling zone coincident with the location of the $3\,kHz$. In figure 32 are shown these modes at $x/c = 0, 45$.

63
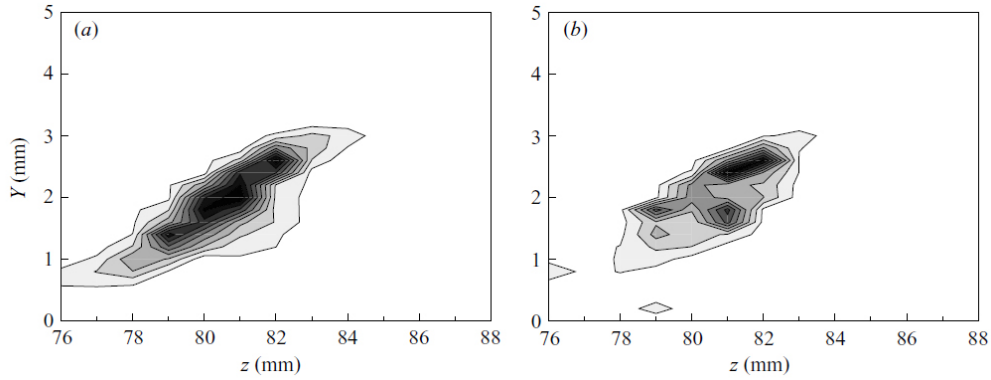
Figure 32: $3\,kHz$ (a) and $6,1\,kHz$ (b) velocity fluctuations r.m.s. at $x/c = 0,40$ [6].

Finally, at $x/c = 0,46$, *localized breakdown* occurs. Figure 33 shows that much of the fine structure of the mean flow has been eliminated. The low-momentum upwelling no longer has a narrow apex; instead this region is wider and flatter.

What is most important, in figure below, is the velocity gradient near the wall to the left of the low-momentum upwelling. This region looks quite different from previous cases; in particular the contour lines are now very close together, indicating that the wall shear here is quite high. What are responsible for these changes in the mean flow are of course the muchincreased velocity fluctuations brought on by breakdown to turbulence.
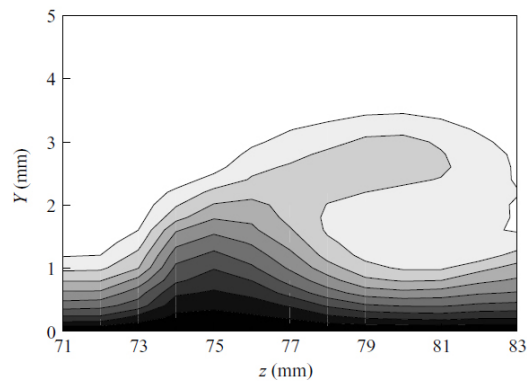
Figure 33: Mean-flow velocity profiles at $x/c = 0,46$ [6].

64

Downstream of the *breakdown* location we expect the stationary structure to dissolve quickly in the face of the enhanced fluctuation levels. This is evident at $x/c = 0,47$ in the mean-flow velocity profiles of figure 34.
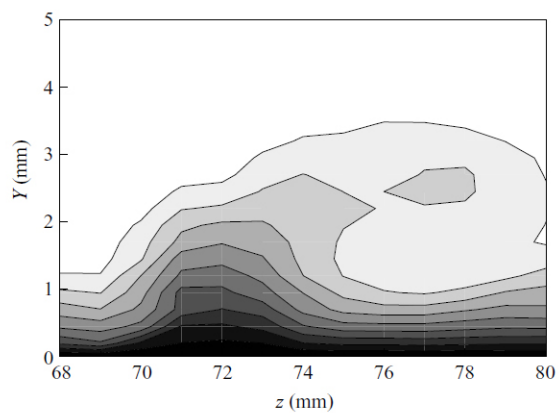
Figure 34: Mean flow velocity profiles at $x/c = 0,47$ [6].

This figure shows the continuing breakup of the low-momentum zone high in the boundary layer and the extension of the high-wall-shear zone. For that final location, the low-momentum upwelling region is fully turbulent, with spectral amplitudes decreasing away from the wall.

3 Mathematical model

After the phenomenology regarding both primary and secondary instability inside a crossflow three-dimensional boundary layer has been presented in last chapter and, even before, equations governing bidimensional boundary layer (*Navier-Stokes equations* for boundary layer), in this chapter, MATHEMATICAL MODEL is obtained in order to compute the pressure field inside a three-dimensional boundary layer. The model will be useful no only for the calculation of pressures themselves, both dimensional and dimensionless, but also for their analysis and their comparison with results obtained for the instability growth factor (energy). This formulation is called *initial-value problem*.

3.1 Base flow

First, it is necessary to define the *base flow*, which it is assumed *viscous* and *incompressible*.
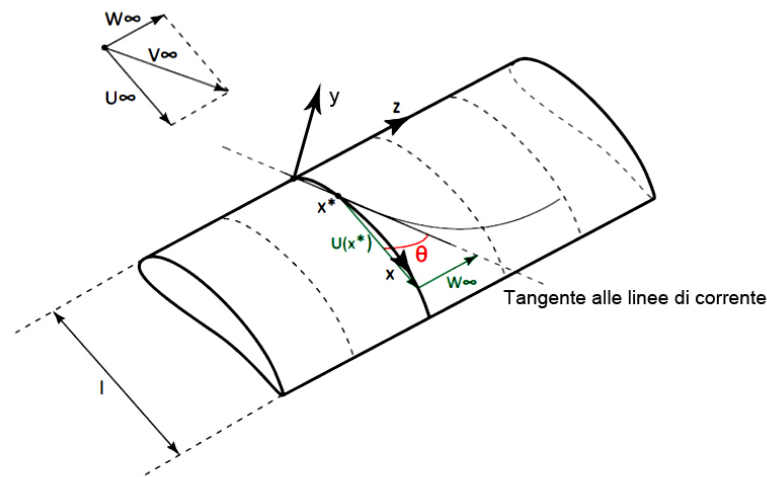
Figure 35: Definition of parameters related to the *base flow*.

As shown in figure 35 and remembering reference system presented in the chapter 2, x coordinate is taken parallel to the freestream velocity, whereas y coordinates orthogonal to it. The potential flow cut the airfoil with velocity U_∞, but a component W_∞, characteristic of crossflow, adds to it and generates resultant velocity V_∞, oriented of a certain θ angle, the so called *crossflow angle*. This angle ensures that V_∞ velocity presents two components, U and W, tangent and orthogonal to streamline respectively, and this fact is explicable, as seen in section 2.1.2, with the presence of strong spanwise pressure gradients on a swept wing.

Streamlines, resulting from superimposition of freestream and induced velocity, are not necessary parallel neither to the x-axis nor to the freestream flow, but they are at an angle θ, which is not steady becouse of potential changes of components U and W.

3.2   Initial values formulation

The *base flow*, described above, is perturbed with small arbitrary three-dimensional perturbations. The *perturbed system* then is linearized, thereafter *continuity equation* and *Navier Stokes equations*, which describe its space-time evolution, can be adapted to the three-dimensional perturbed flow.

Crossflow flow is characterized by following parameters [8]:

$$\begin{cases} U_s = U(x, Re) \\ W_s = W(x, Re) \end{cases}$$

that are velocity components resulting from the base flow and, differently from the apsumptions made presenting *method of small disturbances* in section 2.2.1, in the mathematical model for crossflow boundary layer it is adopted:

$$u = U_s + \tilde{u}, \qquad v = \tilde{v}, \qquad w = W_s + \tilde{w}, \qquad p = P + \tilde{p}.$$

Navier Stokes equations for three-dimensional boundary layer are listed below:

$$\begin{cases} \frac{\partial u}{\partial t} + u\frac{\partial u}{\partial x} + v\frac{\partial u}{\partial y} + w\frac{\partial u}{\partial z} = -\frac{\partial p}{\partial x} + \frac{1}{Re_{\delta*}}(\frac{\partial^2 u}{\partial x^2} + \frac{\partial^2 u}{\partial y^2} + \frac{\partial^2 u}{\partial z^2}) \\ \frac{\partial v}{\partial t} + u\frac{\partial v}{\partial x} + v\frac{\partial v}{\partial y} + w\frac{\partial v}{\partial z} = -\frac{\partial p}{\partial y} + \frac{1}{Re_{\delta*}}(\frac{\partial^2 v}{\partial x^2} + \frac{\partial^2 v}{\partial y^2} + \frac{\partial^2 v}{\partial z^2}) \\ \frac{\partial w}{\partial t} + u\frac{\partial w}{\partial x} + v\frac{\partial w}{\partial y} + w\frac{\partial w}{\partial z} = -\frac{\partial p}{\partial z} + \frac{1}{Re_{\delta*}}(\frac{\partial^2 w}{\partial x^2} + \frac{\partial^2 w}{\partial y^2} + \frac{\partial^2 w}{\partial z^2}) \\ \frac{\partial u}{\partial x} + \frac{\partial v}{\partial y} + \frac{\partial w}{\partial z} = 0 \end{cases}$$

Assuming that disturbances are small enough to considere the hypothesis:

$$u, v, w \ll U_\infty, W_\infty$$

and substituting velocity expressions, obtained by the superimposition of the base flow with the perturbed system, equations become:

$$\begin{cases} \frac{\partial \tilde{u}}{\partial x} + \frac{\partial \tilde{v}}{\partial y} + \frac{\partial \tilde{w}}{\partial z} = 0 \\ \frac{\partial \tilde{u}}{\partial t} + U_s\frac{\partial \tilde{u}}{\partial x} + \tilde{v}\frac{\partial U_s}{\partial y} + W_s\frac{\partial \tilde{u}}{\partial z} + \frac{\partial \tilde{p}}{\partial x} = \frac{1}{Re_{\delta*}}\nabla^2\tilde{u} \\ \frac{\partial \tilde{v}}{\partial t} + U_s\frac{\partial \tilde{v}}{\partial x} + W_s\frac{\partial \tilde{v}}{\partial z} + \frac{\partial \tilde{p}}{\partial y} = \frac{1}{Re_{\delta*}}\nabla^2\tilde{v} \\ \frac{\partial \tilde{w}}{\partial t} + U_s\frac{\partial \tilde{w}}{\partial x} + \tilde{v}\frac{\partial W_s}{\partial y} + W_s\frac{\partial \tilde{w}}{\partial z} + \frac{\partial \tilde{p}}{\partial z} = \frac{1}{Re_{\delta*}}\nabla^2\tilde{w} \end{cases}$$

where:

$$\begin{cases} \tilde{u}(x,y,z,t) \\ \tilde{v}(x,y,z,t) \\ \tilde{w}(x,y,z,t) \\ \tilde{p}(x,y,z,t) \end{cases}$$

are the components of the perturbation velocity and pressure, respectively.

U,W , $\partial U_s/\partial y$ and $\partial W_s/\partial y$ are the terms related with the base flow and, in particular, last two terms represent U and W derivatives with respect to the shear direction. Variables x, y and z are defined from $[0, +\infty]$, $[0, +\infty]$ and $[-\infty, +\infty]$, respectively. From this formulation, we proceed in order to reach equations fundamental for

68

pressure field computation inside crossflow boundary layer, through the transfer from physical space to Fourier field, which is explained in this section.

Moreover, one can notice that all the physical quantities are made dimensionless with respect to freestream flow velocity U_∞ and to boundary-layer *displacement thickness*, defined as:

$$\delta^* = \int_0^\infty (1 - \frac{u}{U_\infty})dy$$

Displacement thickness δ^* allows to define the Reynolds number which appears in the equation system written above:

$$Re_{\delta^*} = \frac{\rho U_\infty \delta^*}{\mu} = \frac{U_\infty \delta^*}{\nu}$$

where ν represents *kinematic viscosity*.

It is useful to remember also the relation between this Reynolds number, identifying perturbated system, and the one related to the base flow, that is the *global Reynolds number* defined with respect a characteristic dimension "L" of the body:

$$Re_{\delta^*} = 1,72 \cdot \sqrt{Re}$$

3.2.1 Perturbation velocity computation

Since previous dormulation is given, it is necessary now to present the method helpful to obtain introduced perturbation velocity, $\tilde{u},\tilde{v},\tilde{w}$, that are terms necessary to solve *boundary layer equations*, making exlicit pressures, which are the object and goal of studies underway.

Equations of the system are then combined to eliminate the pressure, provisionally, and the *vorticity vector* is defined as:

$$\vec{\tilde{\omega}} = [\tilde{\omega}_x, \tilde{\omega}_y, \tilde{\omega}_z]$$

By introducing, further, the kinematic quantity:

$$\nabla^2 \tilde{v} = \tilde{\Gamma} = \frac{\partial \tilde{\omega}_z}{\partial x} - \frac{\partial \tilde{\omega}_x}{\partial y}$$

The system then adopts a reduced form in terms of *vorticity* and *velocity*:

$$\begin{cases} (\frac{\partial}{\partial t} + U_s \frac{\partial}{\partial x} + W_s \frac{\partial}{\partial z})\tilde{\Gamma} - \frac{\partial^2 U_s}{\partial y^2} \frac{\partial \tilde{v}}{\partial x} - \frac{\partial^2 W_s}{\partial y^2} \frac{\partial \tilde{v}}{\partial z} = \frac{1}{Re_{\delta*}} \nabla^2 \tilde{\Gamma} \\ (\frac{\partial}{\partial t} + U_s \frac{\partial}{\partial x} + W_s \frac{\partial}{\partial z})\tilde{\omega}_y + \frac{\partial U_s}{\partial y} \frac{\partial \tilde{v}}{\partial x} = \frac{1}{Re_{\delta*}} \nabla^2 \tilde{\omega}_y \\ \nabla^2 \tilde{v} = \tilde{\Gamma} \end{cases}$$

First equation is none other than *Orr-Sommerfeld equation*, obtained in section 2.2.2, expressed by different variables, while the second one is the *Squire equation*.

For every dependent variable, a combined spatial Laplace-Fourier decomposition in the x and z directions it is performed and defined by:

$$\hat{g}(y, t, \alpha, \gamma) = \int\limits_{-\infty}^{+\infty} \int\limits_{0}^{+\infty} \tilde{g}(x, y, z, t) e^{(-i\alpha x - i\gamma z)} dx dz$$

where $\tilde{g}$ is the general dependent variable, α, which is the longitudinal wave number, is complex ($\alpha = \alpha_r + i\alpha_i$), and γ, which is the transversal wave number, is real.

The system transfered in the *Fourier space*, finally, substituting changed quatities, can be expressed by:

$$
\begin{cases}
\left[\frac{\partial^2}{\partial y^2} - \overrightarrow{k}\right]\frac{\partial \hat{v}}{\partial t} = \left(-i\left(k\cos\phi + i\alpha_i\right)U_s + ik\sin\phi W_s\right)\left[\frac{\partial^2 \hat{v}}{\partial y^2} - \overrightarrow{k}\,\hat{v}\right] + i\left(k\cos\phi + i\alpha_i\right)\frac{\partial^2 U_s}{\partial y^2}\hat{v} \\
\qquad + ik\sin\phi\frac{\partial^2 W_s}{\partial y^2}\hat{v} + \frac{1}{Re_{\delta*}}\left[\frac{\partial^4 \hat{v}}{\partial y^4} - 2\overrightarrow{k}\frac{\partial^2 \hat{v}}{\partial y^2} + \overrightarrow{k}^2\hat{v}\right] \\
\\
\frac{\partial \hat{\omega}_y}{\partial t} = \left(-i\left(k\cos\phi + i\alpha_i\right)U_s - ik\sin\phi W_s\right)\hat{\omega}_y - ik\sin\phi\frac{\partial U_s}{\partial y}\hat{v} + i\left(k\cos\phi + i\alpha_i\right)\frac{\partial W_s}{\partial y}\hat{v} \\
\qquad + U_s\frac{\partial}{\partial x} + W_s\frac{\partial}{\partial z})\tilde{\omega}_y + \frac{1}{Re_{\delta*}}\left[\frac{\partial^2 \hat{\omega}_y}{\partial y^2} - \overrightarrow{k}\,\hat{\omega}_y\right] \\
\\
\left[\frac{\partial^2 \hat{v}}{\partial y^2} - \overrightarrow{k}\,\hat{v}\right] = \hat{\Gamma}
\end{cases}
$$

where, as said in section 2.2.2, α_i is the complex part of the α parameter and is called *spatial damping factor*. In the modified equations system, moreover, $\overrightarrow{k}$ vector and ϕ angle, that is *obliquity angle*, turn up and the last one is an important parameter in order to compute pressures, as it will be seen next. These parameters can be defined, basing on the graphical scheme in figure 36 [9].
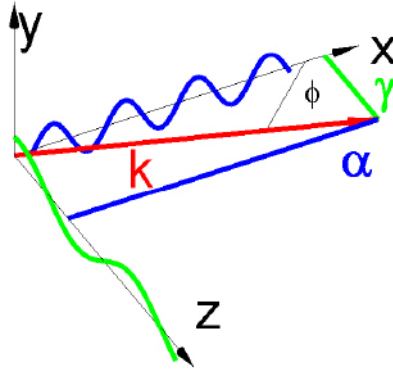
Figure 36: Gemometrical scheme of disturbance, where the disturbance dove la perturbazione spreads along the polar wave number k direction [9].

First parameter can be defined with respect to the *polar wave number* , k:

$$k = \sqrt{\alpha_r^2 + \gamma^2}$$

$$\overrightarrow{k} = k^2 - \alpha_i^2 + 2i\alpha_i k \cos\phi$$

where ϕ is the *obliquity angle* and defined by geometrical link:

$$\phi = \tan^{-1}\left(\frac{\gamma}{\alpha_r}\right)$$

and allows to express single geometrical links, which exists between *polar wave number* and *wave number* along x e z directions:

$$\alpha_r = k\cos\phi$$

$$\gamma = k\sin\phi$$

The polar wave number is also related to the *wave lenght* by the relationship:

$$\lambda = \frac{2\pi}{k}$$

All the presented parameters turn out to be fundamental for the resolution of computational problem in order to obtain both velocities and pressures, as they influence significantly motion field inside the three-dimensional boundary layer, and it is necessary to choose them opportunely.

The system is now of the *fourth order*, two orders upper than the previous system defined on the physical plane, and can be solved by the introduction of suitable *initial* and *boundary conditions*. The last conditions are defined at the limits of the domain under consideration:

$$y = 0 \quad \rightarrow \quad \begin{cases} \hat{v} = 0 \\ \frac{\partial \hat{v}}{\partial y} = 0 \end{cases}$$

$$y = \infty \quad \rightarrow \quad \begin{cases} \hat{v} = 0 \\ \frac{\partial \hat{v}}{\partial y} = 0 \end{cases}$$

Boundary conditions, just exspressed, impose no-slip conditions at wall both on velocity and its derivative. At the same time annulment of these components is imposed outside the boundary layer.

The *vorticity*, instead, must submiti to two imposed conditions:

$$y = 0 \quad \rightarrow \quad \hat{\omega}_y = 0$$

$$y = \infty \quad \rightarrow \quad \hat{\omega}_y = 0$$

Finally, *initial conditions* are arbitrarily imposed to the two variables:

$$\hat{v}(y, t = 0) = y^2 e^{-y^2}$$

$$\hat{\omega}_y(y, t = 0) = 0$$

The problem, under imposed conditions and through the choice of characteristic parameters, can be solved and provides perturbative velocities which appear in the three-dimensional boundary layer equations inside the physical space.

3.3 Mathematical methods for the pressure field computation

In this section, mathematical method for the pressure field computation is presented. Two methods, more precisely, have been taken into account during the work, which are variation of the base concept derived from the *small disturbances theory*. These two methods have been implemented on MATLAB software in order to compute the three-dimensional pressure field inside a crossflow boundary layer. Two methods are also necessary for a mutual comparison and validity control. Basing both on time and efficiency evaluations using the software, one of the two methods has been chosen and used for all the following analysis.

The two methods are explained in the next two paragraphs, which present changed formulations of the governor equations and the process of the *Fourier transformation.*

3.3.1 First method

The fundamental idea, in both methods, is that of making explicit the terms related to pressure gradients $\partial\tilde{p}/\partial x, \partial\tilde{p}/\partial y$ e $\partial\tilde{p}/\partial z$ in Three-dimensional boundary layer equations seen in section 3.2 and then then integrating these pressure gradients, after the simulation, in order to find the pressure values in all the motion field.

In the first method, described here, velocities, obtained with the method explained in section 3.2.1, which are taken from the database saved during previous simulations achieved in POLITECNICO DI TORINO DEPARTMENT OF MECHANICAL AND AEROSPACE ENGINEERING, are immediatly *anti-transformed* from the Fourier field to the physical filed and then put in the system of boundary layer equation.

As seen before, for every dependent variable, a combined *spatial Laplace-Fourier decomposition* in the x and z directions has been performed and defined by:

$$\hat{g}\left(y,t,\alpha,\gamma\right) = \int\limits_{-\infty}^{+\infty}\int\limits_{0}^{+\infty} \tilde{g}(x,y,z,t)e^{(-i\alpha x - i\gamma z)}dxdz$$

The anti-transformation can be ideally expressed as:

$$\hat{u}(y,t,\alpha,\gamma) \quad \xrightarrow{\ \mathcal{F}^{-1}\ } \quad \widetilde{u}(x,y,z,t)$$

where $\hat{u}$ is the generic velocity component in the Fourier space, whereas $\widetilde{u}$ is the generic velocity in the physical space, which will be used in this first method.

When the velocity components $\hat{u}, \hat{v}$ and $\hat{w}$ are all transformed to the physical space, depending now on x, y, z space variables and t time variable, and the reference velocities U_s and W_s of the base flow are given, the system of three-dimensional boundary layer equations can be espressed as:

$$\begin{cases} \frac{\partial \tilde{p}}{\partial x} = -\frac{\partial \tilde{u}}{\partial t} - U_s \frac{\partial \tilde{u}}{\partial x} - \tilde{v} \frac{\partial U_s}{\partial y} - W_s \frac{\partial \tilde{u}}{\partial z} + \frac{1}{Re_{\delta*}} \nabla^2 \tilde{u} \\ \frac{\partial \tilde{p}}{\partial y} = -\frac{\partial \tilde{v}}{\partial t} - U_s \frac{\partial \tilde{v}}{\partial x} - W_s \frac{\partial \tilde{v}}{\partial z} + \frac{1}{Re_{\delta*}} \nabla^2 \tilde{v} \\ \frac{\partial \tilde{p}}{\partial z} = -\frac{\partial \tilde{w}}{\partial t} - U_s \frac{\partial \tilde{w}}{\partial x} - \tilde{v} \frac{\partial W_s}{\partial y} - W_s \frac{\partial \tilde{w}}{\partial z} + \frac{1}{Re_{\delta*}} \nabla^2 \tilde{w} \\ \frac{\partial \tilde{u}}{\partial x} + \frac{\partial \tilde{v}}{\partial y} + \frac{\partial \tilde{w}}{\partial z} = 0 \end{cases}$$

From this system one can get pressure gradients values all over the domain considered in the problem and, through a numerical integration in MATLAB software, the pressure field in the crossflow boundary layer is obtained, that is $\tilde{p} = \tilde{p}(x,y,z)$ in the physical space.

Having all the pressure values in the considered field it is easy to achieve each wanted visualization along x, y or z axis. But it has been noted, during tests on the method, that it is quite slow, taking many times to solve the equations. Moreover, in order to remove some failings at the initial limit of the domain, it has been found that integrating the second equation of the system, which explicits $\frac{\partial \tilde{p}}{\partial y}$ gradient, to compute the pressure, these problems are significantly, but not completly, reduced. Although this equatons is used, few failings still remain.

3.3.2 Second method

In previous paragraph, problems of the first method have been presented. With the necessity to remove them, a second method has been introduced, considering a different approach.

The equations are now first transformed with the *spatial Laplace-Fourier decomposition* in the x and z directions and perturbative velocities $\hat{u}, \hat{v}$ and $\hat{w}$ are directly introduced in the system in the Fourier space. The transformation is obtained substituting each mathematical operator in the equations as:

$$\begin{cases} \frac{\partial \varphi}{\partial x} & \longrightarrow & i\alpha \cdot \varphi \\ \frac{\partial \varphi}{\partial z} & \longrightarrow & i\gamma \cdot \varphi \\ \nabla^2 \varphi & \longrightarrow & \left(\frac{\partial^2}{\partial y^2} - k^2 \right) \cdot \varphi \end{cases}$$

where φ is a generic variable and $k^2 = \alpha^2 + \gamma^2$.

The system transfered to the Fourier space then turns out as:

$$\begin{cases} i\alpha\hat{p} = -\frac{\partial \hat{u}}{\partial t} - i\alpha\hat{u}U_s - \hat{v}\frac{\partial U_s}{\partial y} - i\gamma\hat{u}W_s + \frac{1}{Re_{\delta*}} \left(\frac{\partial^2}{\partial y^2} - k^2 \right) \hat{u} \\ \frac{\partial \hat{p}}{\partial y} = -\frac{\partial \hat{v}}{\partial t} - i\alpha\hat{v}U_s - i\gamma\hat{v}W_s + \frac{1}{Re_{\delta*}} \left(\frac{\partial^2}{\partial y^2} - k^2 \right) \hat{v} \\ i\gamma\hat{p} = -\frac{\partial \hat{w}}{\partial t} - i\alpha\hat{w}U_s - \hat{v}\frac{\partial W_s}{\partial y} - i\gamma\hat{w}W_s + \frac{1}{Re_{\delta*}} \left(\frac{\partial^2}{\partial y^2} - k^2 \right) \hat{w} \end{cases}$$

As said before, perturbative velocities are directly introduced into the system, whereas $\frac{\partial U_s}{\partial y}$ and $\frac{\partial W_s}{\partial y}$ base flow gradients are given and so unchanged after the transformation.

The second equation is taken into account again in order to minimize failings at the edge of the domain and it is integrated with respect to y coordinate. The result of this numerical integration, implemented on MATLAB, is the pressure field itself in the Fourier space, all over the computational domain:

$$\hat{p} = \hat{p}(y, t, \alpha, \gamma)$$

So it is necessary to transfer pressure values form this space to the physical space, dependant on x, y, z and t coordinates. The anti-transformation process can be expressed now as:

$$\hat{p}(y, t, \alpha, \gamma) \quad \xrightarrow{\mathcal{F}^{-1}} \quad \widetilde{p}(x, y, z, t)$$

Hence the perturbed pressure field in the physical space is derived, coming to the same results as the first method.

However, too long times of computing are drastically reduced, proceeding with this method, and failings at the domain origin are totally removed. As far as the results of the two method are concerned, they perfectly agree both for the pressure gradients and pressure themselves. The second method has proved to be more efficient and faster than the first one, so it has been chosen for the simulation and parametric analysis, implemented in the next chapter.

3.4   Amplification factor

At the end of the present chapter, it is necessary to shortly present another parameter, which will useful up ahead during the parametric analysis for a comparison with the results obtained for the dimensionless pressure field, that is the *amplification factor G*. Such a parameter represents a functional indication of the instabilty of the flow, on varying several characteristic paremeters, inside a three-dimensional boundary layer, region taken into account by this thesis.

To measure the growth of the perturbations, *kinetic energy density* is defined:

$$
\begin{aligned}
e(t; \alpha, \gamma, Re) &= \frac{1}{2} \frac{1}{2y_d} \int_{-y_d}^{+y_d} \left(|\hat{u}^2| + |\hat{v}^2| + |\hat{w}^2| \right) dy = \\
&= \frac{1}{2} \frac{1}{2y_d} \frac{1}{|\alpha^2 + \gamma^2|} \int_{-y_d}^{+y_d} \left(|\frac{\partial \hat{u}}{\partial y}|^2 + |\alpha^2 + \gamma^2| |\hat{v}^2| + |\hat{\omega}_y{}^2| \right) dy
\end{aligned}
$$

where $+y_d$ and $-y_d$ are the computational limits of the domain along the orthog-

onal direction to the surface, while $\hat{u}(y,t,\alpha,\gamma)$, $\hat{v}(y,t,\alpha,\gamma)$ and $\hat{w}(y,t,\alpha,\gamma)$ are the transformed velocity components of the perturbed field.

The amplification factor, G, is then introduced, as the kinetic energy density normalized with respect to its initial value:

$$G(t;\alpha,\gamma) = \frac{e(t;\alpha,\gamma)}{(t=0;\alpha,\gamma)}$$

This parameter indicates the disturbance growth, thus its amplification or damping. Basing on the asymptotic trend of G so the flow results stable or unstable. Moreover, the amplification factor derivative indicates the achievement of the asymptotic limit for the perturbed flow.

In the next chapter, G will be the basis for comparison with the pressure field, in order both to comprehend if a link between the two trends could exist and to choose which configuration, stable or unstable, meaningful, is to be simulated.

4   Perturbative pressure field parametric analysis

The three-dimensional boundary layer *perturbative pressure field*, $\widetilde{p} = \widetilde{p}(x, y, z, t)$ has been computed thanks to the analytical method explained in section 3.3.2 of the previous chapter. The focus now will be pointed on a parametric analysis of the perturbed pressure field in order to consider effects of boundary layer flow characteristic parameters on the perturbed motion field, also analysing initial and asymptotic pressure trends.

It is important to remember that pertubed pressure computed is dimensionless, as it is divided by the freestream typical quantities:

$$\tilde{p} = \frac{\tilde{p}_{dim}}{\rho U_\infty^2}$$

and the time, t, is made dimensionless as:

$$t_{car} = \frac{\delta^*}{U_\infty}$$

where t_{car} is the so-called *characteristic time*, which will be merely written as t up ahead. So a *dimensionless perturbed pressure field* is taken into accout in order to make all pressure trends along each direction "self-similar", allowing a correct parametric comparison.

4.1   Simulation parameters

It can be useful to list all the characteristic parameters, some of which have been introduced in section 3.1 and 3.2.1, that will be varied during the analysis. Referring to figure 37 showing the crossflow boundary layer velocity-field, such parameters are listed below giving a functional statement for the analysis understanding.
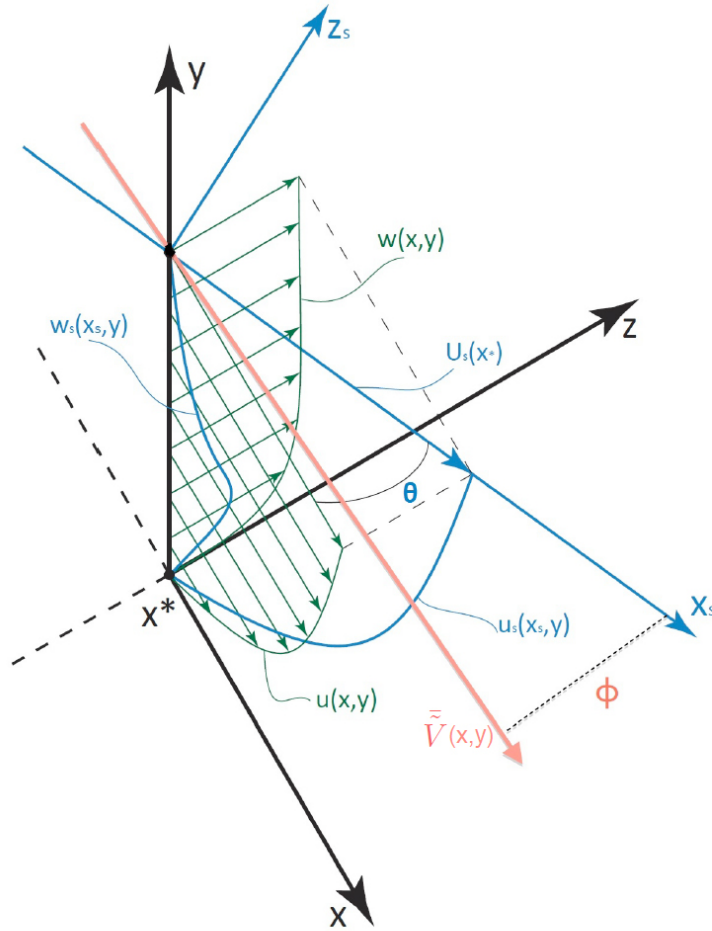
Figure 37: Reference systems and characteristic parameters of the crossflow boundary layer.

CROSSFLOW ANGLE θ First, one can notice that the $[x_s, y, z_s]$ reference system is associated with directions tangent and orthogonal to the streamlines respectively. These directions are defined, with respect to the generic $[x, y, z]$ reference system, by the well-known *crossflow angle* θ, which measures the inclination of streamlines due to crossflow component, W, and so θ coincides with the angle between U velocity, parallel to x axis, and U_s base flow velocity, parallel to x_s axis. The value of this

angle is assumed costant taking into account a certain value computed at 20% of the chord lenght.

The values of crossflow angle chosen for the parametric analysis of the simulated three-dimensional pressure field are:

$$\theta = \left[\frac{\pi}{6} , \frac{\pi}{4} , \frac{\pi}{3} \right]$$

OBLIQUITY ANGLE ϕ The second fundamental parameter to be introduced is the angle which the perturbation creates with the x_s, z_s axes, that are the directions parallel and orthogonal to the streamline motion as seen above, and it is called *obliquity angle* ϕ. In other words, it represents the incidence the perturbative wave comes in the boundary layer with.

The values of obliquity angle chosen for the parametric analysis of the simulated three-dimensional pressure field are:

$$\phi = \left[0 , \frac{\pi}{4} , \frac{\pi}{2} \right]$$

These values coincide with *longitudinal, oblique* and *orthogonal perturbative waves*, respectively.

POLAR WAVE NUMBER k Another important parameter is the *polar wave number* or merely the *wavelength number k*. As seen in section 3.2.1, it is defined as:

$$k = \sqrt{\alpha_r^2 + \gamma^2}$$

and is also related to *wave lenght* as:

$$\lambda = \frac{2\pi}{k}$$

For the implementing simulations and next analysis some of these values, considered the most significant and representative of short and long wase, are chosen:

$$k = [0.02\,,\,0.06\,,\,0.1\,,\,0.6\,,\,1\,,\,1.2\,,\,1.6]$$

As can be noticed, this is a quite wide range of wave numbers that represents three different order of magnitude.

DIMENSIONLESS PRESSURE GRADIENT β The *dimensionless pressure gradient* β or *Hartree parameter* is related to the definition of the diedral angle and has the following mathematical expression:

$$\beta = \frac{2m}{m+1}$$

where m, as it will be seen in the next chapter, is a characteristic parameter of the flow.

The dimensionless pressure gradient characterizes different flow typologies, as crossflow boundary layers, if $\beta \neq 0$, or Blasius boundary layers, if $\beta = 0$. Since the field under examination is the crossflow boundary layer, two different values of β are chosen:

$$\beta = [-0.1988\,,\,1]$$

where the negative value suggests a *positive pressure gradient* along x-coordinate, which involves, for the Bernoulli equation, a deceleration of the flow. This deceleration is a strongly destabilizing factor, so we will refer to $\beta < 0$ as an unfavourable pressure gradient. On the other hand, the positive value of β suggests a *negative pressure gradient* and an acceleration of the flow along x-axis. This is, on the contrary, a favourable pressure gradient.

82

REYNOLDS NUMBER $Re_{\delta*}$ The last parameter to be decided is the Reynolds number $Re_{\delta*}$ related to the *displacement thickness* δ^*. This choice is made basing on *linear stability studies*, mentioned in section 1.4, and on THEORY OF LINGWOOD, which states, as written in section 2.3.2, that rotating-disk boundary layers support an *absolute instability* at $Re = 510$. Stable and unstable behaviours, respectively, are expected for:

$$Re_{\delta*} = [100\,,\,5000]$$

and these will be the Reynolds numbers considered in the following numerical simulations in order to compare pressure behaviours both inside a well-known stable and in an unstable boundary layer.

In order to have a statement of chosen parameters for the following numerical simulations of the crossflow boundary layer, the summarizing table 1 is shown below.

REYNOLDS NUMBER $Re_{\delta*}$	Re=100 , Re=5000
PRESSURE GRADIENT β	1 , -0,1988
CROSSFLOW ANGLE θ	$\frac{\pi}{6}$, $\frac{\pi}{4}$, $\frac{\pi}{3}$
OBLIQUITY ANGLE ϕ	0 , $\frac{\pi}{4}$, $\frac{\pi}{2}$
WAVELENGTH NUMBER k	$0.02\,,0.06\,,0.1\,,0.6\,,1\,,1.2\,,1.6\,,2$

Table 1: Summarizing table of the parametrs chosen for the numerical simulation of the crossflow boundary layer *pressure field*.

4.2 Simulation results

This section represents the fulcrum of this thesis because now all the results of several numerical simulations implemented in order to compute the pressure field of a three-dimensional boundary layer, are shown and analysed. Studying the effects of each parameter variation on the pressure field inside the crossflow boundary layer is the goal of this chapter and of the entire thesis.

The pattern we have decided to follow is to vary one parameter a time at a certain values. In this way it is possible to compute and analyse different configurations of the boundary layer and incoming perturbative waves, not only showing significant changes in the pressure field, but also looking for links between pressure and amplification factor G temporal trends, related to instability phenomenon. In addition, the computation of G is useful to decide which configuration of the flow is to be chosen, from time to time, in order to simulate either a stable or an unstable field.

Basing on these preliminary remarks it has been decided to simulate certain configurations of the perturbed crossflow boundary layer, expecting a priori a significant behavior and trend of the pressure. The simulations to be made are shortly listed below and will be completely presented, shown and explained in following paragraphs.

1. VARIATION OF WAVELENGTH NUMBER k for two different configurations:
    - $\theta = 30^o$, $\phi = 45^o$, $\beta = 1$ for $Re = 100$
    - $\theta = 60^o$, $\phi = 90^o$, $\beta = 1$ for $Re = 5000$.

2. VARIATION OF OBLIQUITY ANGLE ϕ for the fixed configuration:
    - $\theta = 60^o$, $k = 0.4$, $\beta = 1$ for $Re = 5000$.

3. VARIATION OF CROSSFLOW ANGLE θ for the fixed configuration:
    - $\phi = 45^o$, $k = 0.4$, $\beta = 1$ for $Re = 5000$.

4. VARIATION OF PRESSURE GRADIENT β for the fixed configuration:
    - $\theta = 30^o$, $\phi = 0^o$, $k = 0.1$ for $Re = 5000$

5. PRESSURE SURFACES on x, y and y, z planes for the configurations listed above.

For each implemented simulation, the graphs reporting pressure results will be shown in order to achieve the parametric analysis. The graphs realized are:

- Graphs showing $\tilde{p} = \tilde{p}(x)$, $\tilde{p} = \tilde{p}(y)$ and $\tilde{p} = \tilde{p}(z)$, at characteristic time $t = 40$, in order to evaluate the spatial evolution of the pressure field.

- Graphs showing $\tilde{p} = \tilde{p}(y)$ at characteristic times $t_1 = 15$, $t_2 = 40$ and $t_3 = 95$ in order to evaluate the spatial and temporal evolution of the pressure field.

- Graph showing the temporal trend of the pressure at fixed spatial points (x, y, z) in order to compare results achieved with the amplification factor G.

Then, in the following paragraphs, results obtained from each numerical simulation will be listed and the trends of the pressure field inside the crossflow boundary layer will be carefully investigated.

Finally, the domains fixed for the three spatial coordinates x, y, z and the temporal coordinate t, in the MATLAB numerical simulations are:

$$\begin{cases} x \in [5 \div 150] & with \ \triangle x = 0.05 \\ z \in [-50 \div 50] & with \ \triangle z = 0.05 \\ t \in [0 \div 900] \end{cases}$$

whereas for y coordinate the domain is included between:

$$\begin{cases} y \in [0 \div 250] & with \ \triangle y = 0.05 \quad for \ k < 0.2 \\ y \in [0 \div 100] & with \ \triangle y = 0.05 \quad for \ 0.2 \le k \le 1.2 \\ y \in [0 \div 50] & with \ \triangle y = 0.05 \quad for \ k > 1.2 \end{cases}$$

where all the values of the domain are dimesionless and the origin of the reference system, as said before, is at the wing leading edge.

4.2.1 Variation of polar wavenumber k

In this paragraph, the effects of the variation of *polar wavenumber k* on the perturbative pressure field are shown and investigated in order to find a correlation between the wavelength of the disturbances introduced in the pressure field. The perturbative pressure field, in this chapter, is not refered to a reference mean pressure, which will be add during the dimensional total flow analysis in the last chapter; all the variations, positive and negative, are not to be considered final total value, but only sums and decrements, respectively, which will be added to the reference mean pressure afterwards.

As listed above, the first configuration to be analysed is:

1. $\theta = 30^o$, $\phi = 45^o$, $\beta = 1$ *for $Re = 100$*

which is a flow tipology, arbitrarily chosen, with intermediate values of the characteristic parameters. We espect a stable behaviour for this Reynolds numbers and that the perturbative waves affects the pressure field both along x and z direction.

The graph, accounting the simulation results, are shown and analysed below; the same description procedure will be followed in next paragraphs for all the other configurations.

In figure 38 (a) perturbative pressure profiles along x direction, $\tilde{p} = \tilde{p}(x)$, are shown, by varying wavenumber from $k = 0.02$, a long wave with $\lambda \approx 314.15$, to $k = 2$, related to a small value of the wavelength $\lambda \approx 3.14$. As it can be seen, this parameter significantly affects pressure profiles of the flow under investigation, even if differently for each of its values. Large wavenumbers, related to small wavelengths, up to $k = 0.6$, slightly affect the pressure field, and small periodic fluctuations in the range of zero value are shown (c). In particular, observing figure 38 (b), pressure for $k = 0.6$ presents small oscilaltion periods and oscillations around zero, about $\tilde{p} \simeq \pm 2 \cdot 10^{-4}$, that are very small with respect to longer waves, which are two orders of magnitude higher.

(a)

(b)

(c)
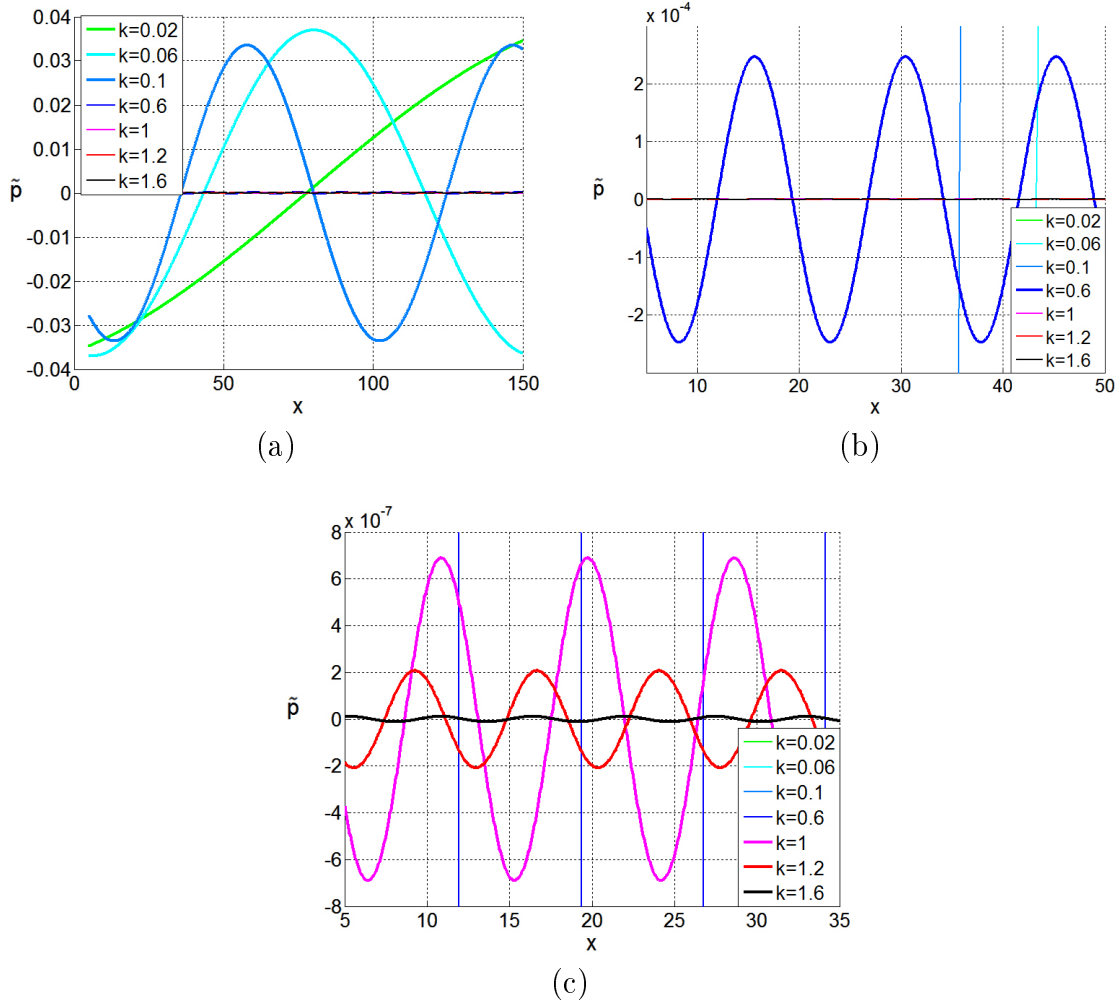
Figure 38: Pressure profiles along x direction (a), with fixed $y = 10$ and $z = 3$, and enlargement (b,c), on varying *wavenumber* k, at characteristic time $t = 40$, for $\theta = 30^o$, $\phi = 45^o$, $\beta = 1$ and $Re = 100$ configuration.

On the contrary, this sinusoidal trend is highly clear going on to smaller wavenumbers, which present higher maximum and minimum points, that are higher amplitudes of the fluctuations. An higher amplitude, in particular, is noticed for $k = 0.1$, which represents a wavelength affecting $\tilde{p}$ along x coordinate with a very larger oscillation period than $k = 0.6$.
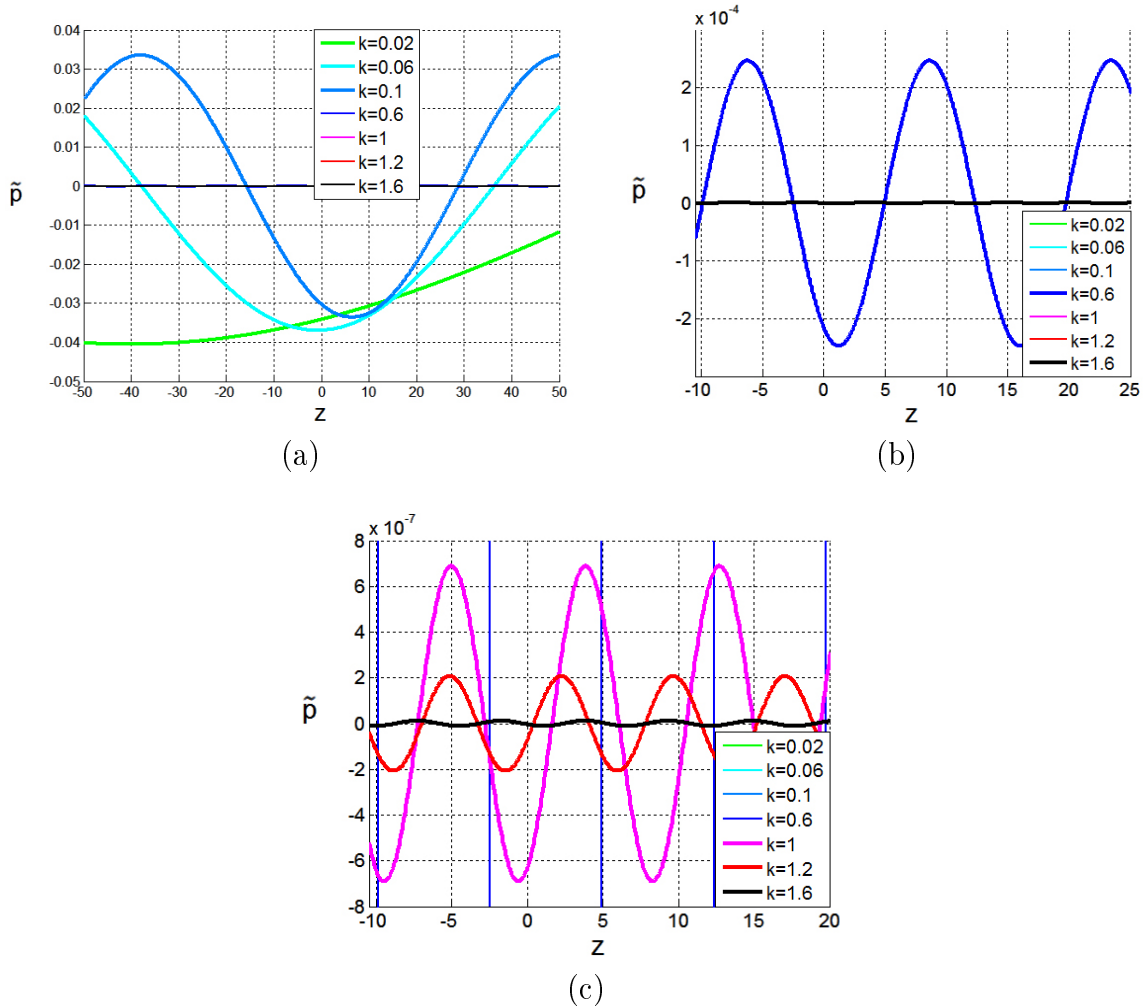
Figure 39: Pressure profiles along z direction (a), with fixed $x = 10$ and $y = 10$, and enlargement (b,c), on varying *wavelength number* k, at characteristic time $t = 40$, for $\theta = 30^o$, $\phi = 45^o$, $\beta = 1$ and $Re = 100$ configuration.

Proceeding forward to smaller values of k, the period continues to increase and the amplitude increases as well. At $k = 0.02$, the oscillation period and amplitude significantly further increase and the period presents a doubled value than the shorter wavelengths. This trend could have a significant influence on the mean pressure field, as it will be investigated more deeply in the next chapter, and we expect a certain

influence on the flow by intermediate wavelengths too. The results obtained show a periodic trend similar to the one of the *velocity profile* along x coordinate, as it is shown in figure 36, since the pressure term, according to Bernoulli, is directly related to the inverse of the velocity term.

As far as the pressure contour along z is concerned, figure 39, it is important to remember that, along this direction, the velocity profile is considered to be periodic, as along x axis, and the periods of the velocity fluctuation are quite similar. This fact can be noticed in figure 39 (a) where the profile is clearly sinusoidal and the period of the oscillation around the mean value is similar to the one along the x direction. All wavelengths have the same oscillation period values and amplitudes of the pressure trend along x. This is what is exactly expected with $\phi = 45^o$ configuration.

Disturbances so seem to equally affect the pressure profiles along both directions, having wavelength variations the same influence too.

In figure 40 and 41, perturbative velocities profiles $\tilde{u}(y)$, $\tilde{v}(y)$ and $\tilde{w}(y)$ along y-direction are now shown in order to compare the velocity and pressure perturbative fields and give an idea about the starting velocities.
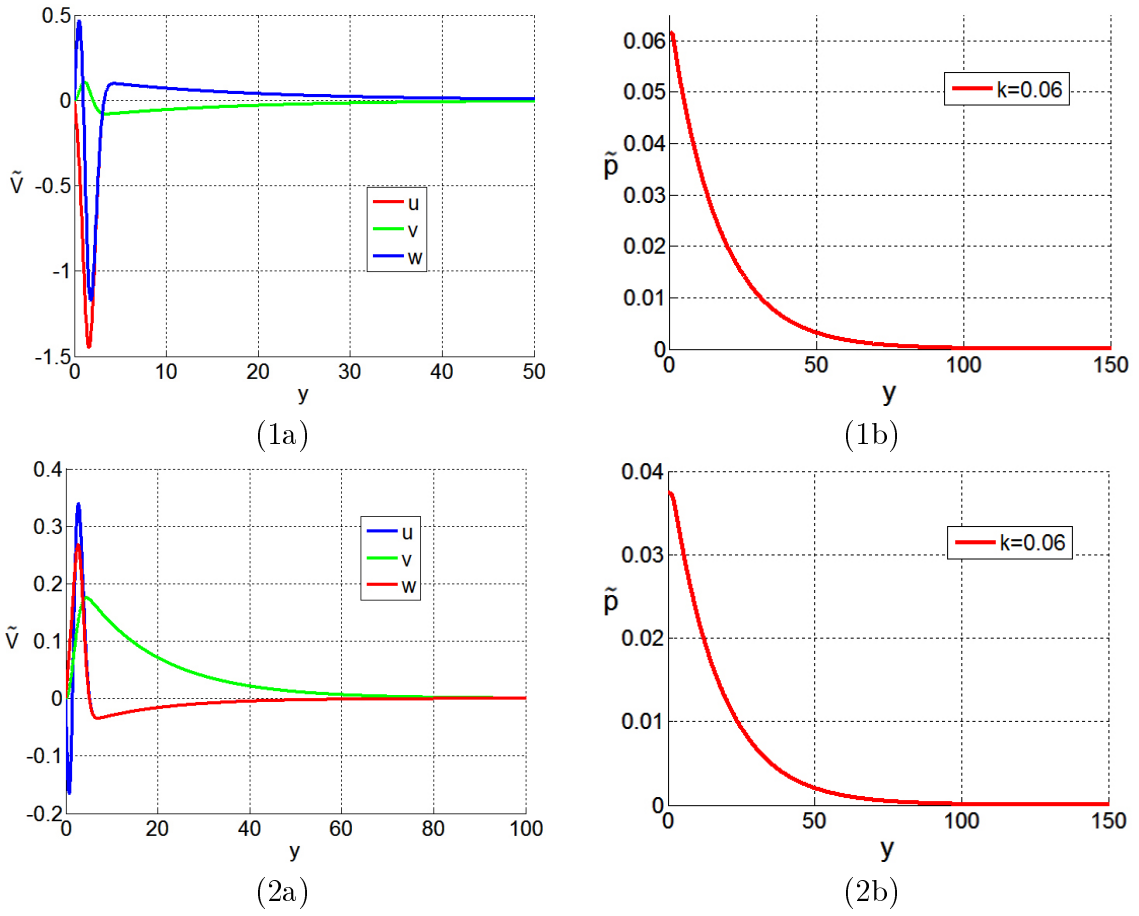
Figure 40: Spatial evolution along y-axis of velocity $\tilde{v} = \tilde{v}(y)$, $\tilde{v} = \tilde{v}(y)$, $\tilde{w} = \tilde{w}(y)$ and pressures $\tilde{p} = \tilde{p}(y)$ (1b, 2b) at times $t_1 = 25$ (1a, 1b), and $t_3 = 95$ (2a, 2b), for $x = 10$, $z = 3$ and $k = 0.06$.

(3a)

(3b)

(4a)

(4b)
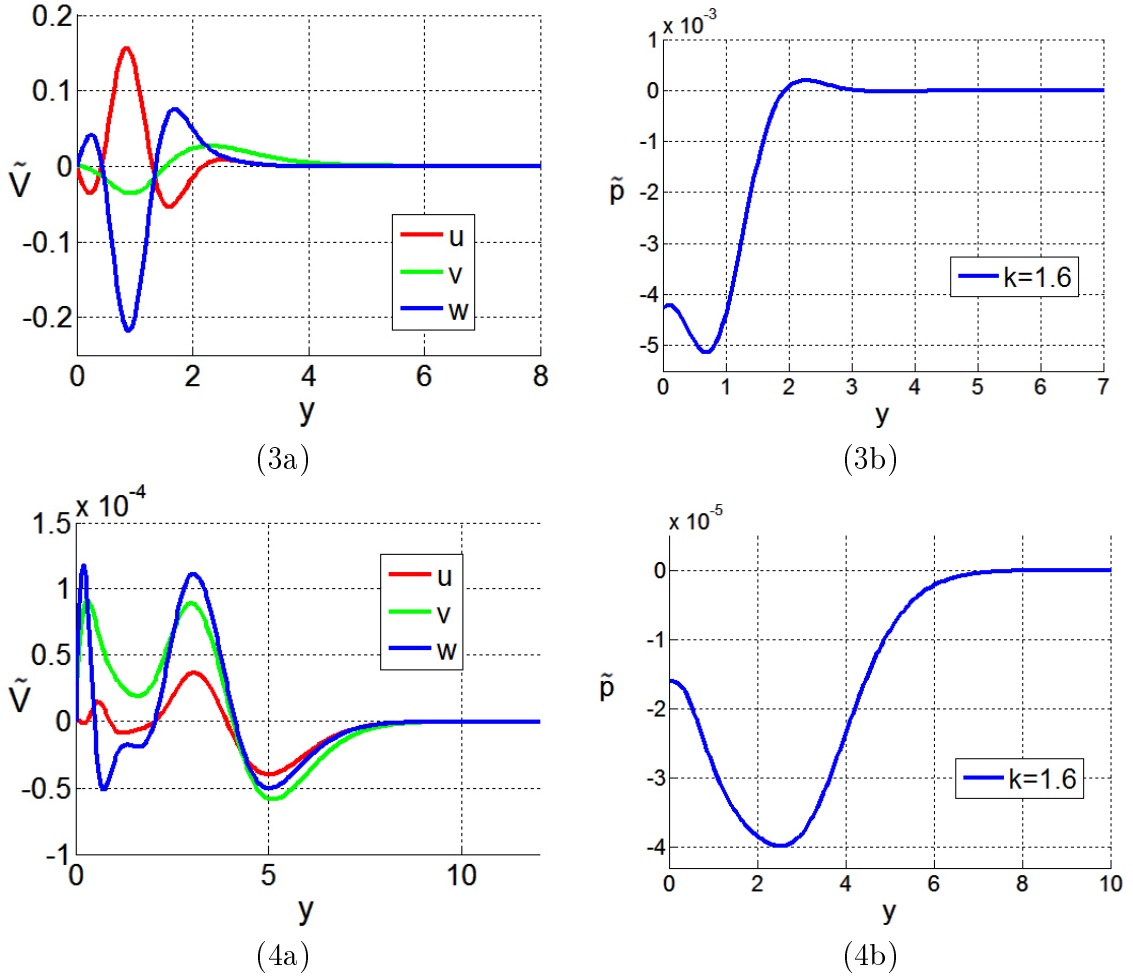
Figure 41: Spatial evolution along y-axis of velocity $\tilde{v} = \tilde{v}(y)$, $\tilde{v} = \tilde{v}(y)$, $\tilde{w} = \tilde{w}(y)$ and pressures $\tilde{p} = \tilde{p}(y)$ (1b, 2b) at times $t_1 = 25$ (1a, 1b), and $t_3 = 95$ (2a, 2b), for $x = 10$, $z = 3$ for $k = 1.6$.

In figure 42 the spatial evolution of dimensionless perturbative pressure, $\tilde{p} = \tilde{p}(y)$, at three fixed characteristic times, $t = 25$, $t = 60$, $t = 95$, is shown in order to give an idea also of the temporal development of the flow along the coordinate orthogonal to the wall.

At $t = 15$ (1a), that is a time in which the perturbation is very strong, the pressure assumes positive starting values at wall for wavelengths from $k = 0.06$ to $k = 0.1$,

91
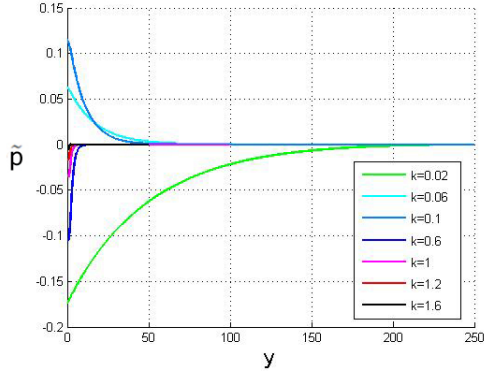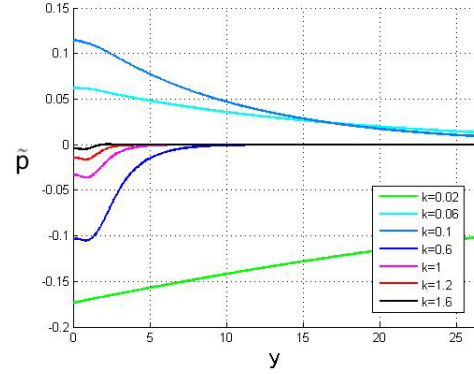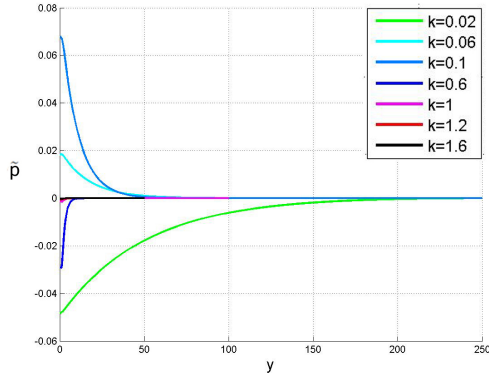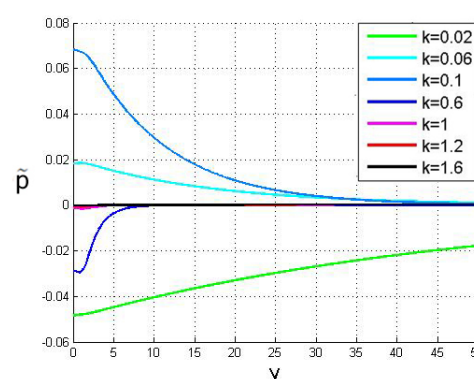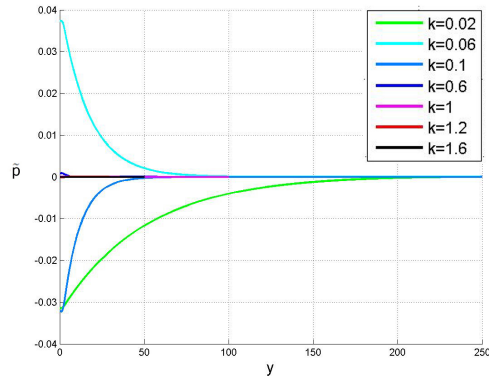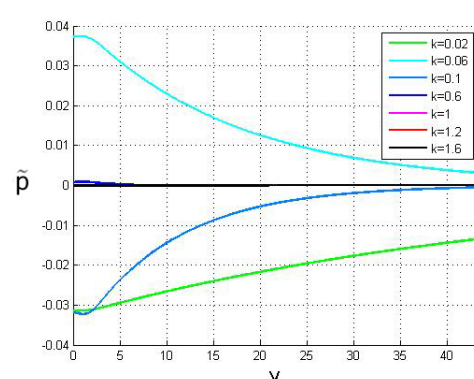
Figure 42: Spatial evolution of pressure $\tilde{p} = \tilde{p}(y)$ at characteristic times $t_1 = 15$ (1a), $t_2 = 40$ (2a) and $t_3 = 95$ (3a), for $x = 10$ and $z = 3$, and enlargements at the wall (1b, 2b, 3b).

while $k = 0.02$ and others lower wavelengths present negative perturbative pressure quantities close to the wall with the lower one for $k = 0.02$ itself. This pressure goes to zero, at $y \simeq 200$, while for short wavelengths, figure 42 (b), from $k = 0.6$ to $k = 1.6$, pressure goes to zero at $y \simeq 3 \div 10$. For $k = 0.06$ and $k = 0.1$, instead, the symptotic state is reached for $y \simeq 60$; as it can be seen in the enlargment, then an increase of the wavelength leads to higher thickness of the perturbative pressure profiles.

It is also to be noticed that, very close to the wall, high wave-numbers induce a certain oscillation in their profiles with a *change in the pressure gradient sign*, about at $y \simeq 2$, generating maximum points as greater as the wavelength number is decreased.

At $t = 40$ (2a), low wavelength numbers, up to $k = 0.6$, present elevated perturbative pressures along y direction, but with one order of magnitude lower values than previous time step, beyond $\tilde{p} = 0.06 \div 0.02$, and the same thickness. On the other hand, for high wavelength numbers, pressures are almost steady around the mean value, since the perturbation is made damped for low wavelength. Near the wall (2b) a change in pressure slope is noticed only for $k = 0.6$.

Finally, at $t = 95$ (3a), the influence of the disturbance introduced is lower than before, as it can be noticed from the low pressures at wall, because the pressure field is reaching a steady and stable state, since the perturbations are going to blow over. Only a significant change is noticed, that is for $k = 0.1$, which presents a change in the pressure gradient sign. This phenomenon may be related to the beginning of the disturbance damping, since every temporal decreasing of pressure profile is marked by such a variation in sign. This fact can be interesting as an indicator about the damping of perturbative pressure profile along y coordinate.

(a)   (b)
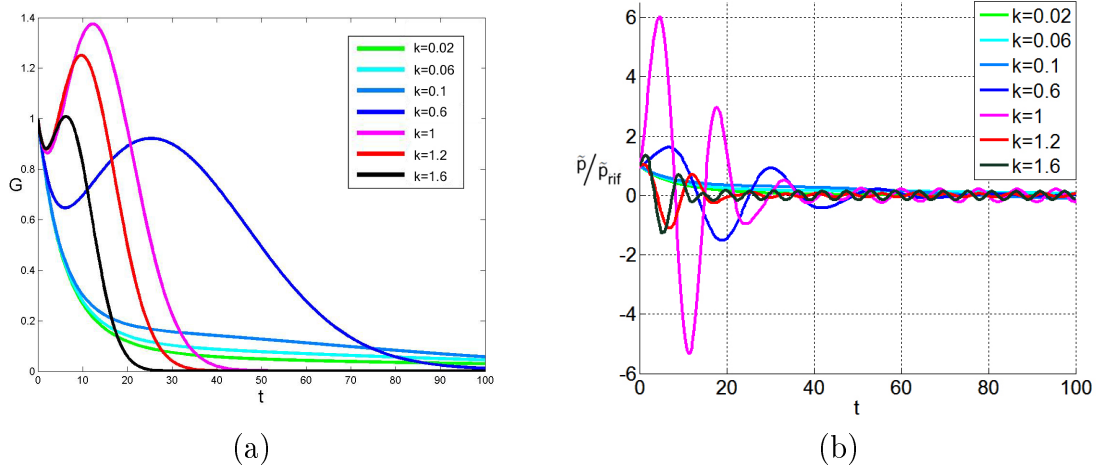
Figure 43: Temporal development of G (a) and $\tilde{p}$ (b) for 100 characteristic time, at fixed spatial point, $x = 10$, $y = 10$, $z = 3$, on varying *wavelength number k*, for $\theta = 30^o$, $\phi = 45^o$, $\beta = 1$ and $Re = 100$ configuration.

In figure 43 (a) amplification factor G development in time is shown. As it can be seen, the configuration under analysis is a stable one because G reaches a zero value within about 100 characteristic times for all the considered wavelength numbers. The highest peaks are shown for $k = 1$, 1.2, 1.6, 2 with an oscillating transient growth, that, however, reaches quickly the zero value. The most particular behaviour is related to $k = 0.6$, which cancels out at about $t = 100$, whereas lower wavelength numbers present decreasing trends over thus time and so they have a longer transient period. Such a behaviour is well-noticeable in temporal development of the perturbative pressure, $\tilde{p}$, refered to its initial value $\tilde{p}/\tilde{p}_{rif}$, taking into account a spatial fixed point $[x, y, z]$ in the computational domain, for 100 characteristic times, shown in figure 43 (b) .

The graph shows a clear correlation between the amplification factor G and the trend of the perturbative field pressure $\tilde{p}$. As for G, also for pressure, high wavelength numebers $k = 1$, 1.2, 1.6, 2 show a shorter transient period than the lower ones, with several oscillations around the mean value, that present higher maximum and lower minimum points proceeding toward lower wavelength, up to $\tilde{p}/\tilde{p}_{rif} = 6$ at $t = 5$

and $\tilde{p}/\tilde{p}_{rif} = -5$ at $t \geq 10$ respectively, and also wider oscillation periods. The asymptote is reached, exactly as in previous graph, at about $t = 20 \div 50$.

As far as the $k = 0.6$ pressure trend behaviour is concerned, this is significantly different from the others, presenting much larger oscillation periods and lower peaks than $k = 1$. The asymptotic value is reached for $t = 100$, as it is expected from the G graph.

This periodic transient attenuates or completely disappears, as in the previous graph, for lower values of k. These pressures reach the asymptotic state for significant characteristic times until $t = 200$, not shown here.

For $Re = 100$ then a good correlation between the two quantities is found and it is possible to confirm that, at this low Reynolds number, a stable state flow is present. Pressures, indeed, for each changing k parameter, go to an asymptotic value, which represent an indication of stability.

Finally, for this configuration, pressure field *bidimensional surfaces* are shown in figure 44 in order to give a qualitative idea of the region under analysis.

Equal and significant oscillating trends are shown for pressures along x and z directions, whereas along y the pressure cancels out away from the wall. Strong *oscillating perturbative pressure waves* then pass obliquely through the x, y plane with lower intensities going away from the wall.
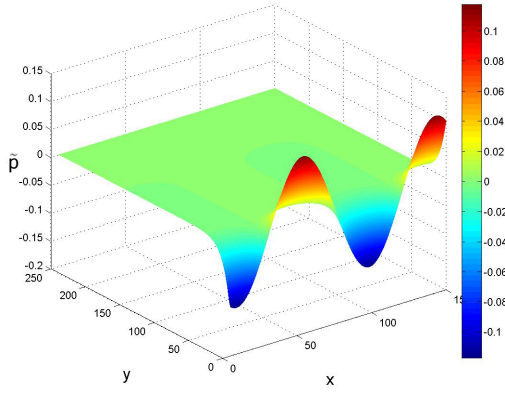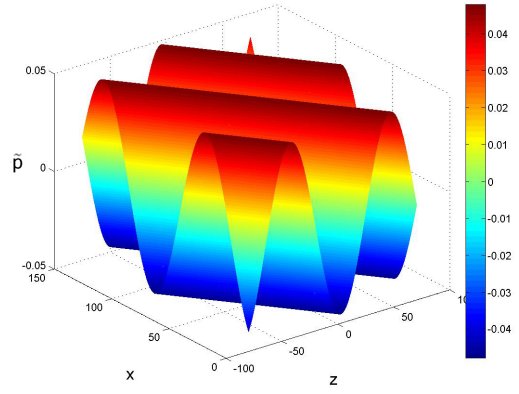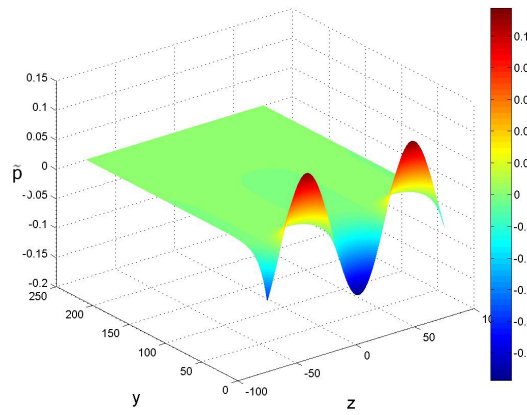
Figure 44: Pressure field *bidimensional surfaces* on $x - y$ (a), $x - z$ (b), $y - z$ (c) planes at $k = 1$ and $t = 60$, for $\theta = 30^o$, $\phi = 45^o$, $\beta = 1$ and $Re = 100$ configuration.

The second configuration to be analysed is:

2. $\theta = 60^o$, $\phi = 90^o$, $\beta = 1$ for $Re = 5000$

It is chosen basing on the amplification factor G diagram, for this flow scheme, presented in figure 45 (a) below.

(a)   (b)
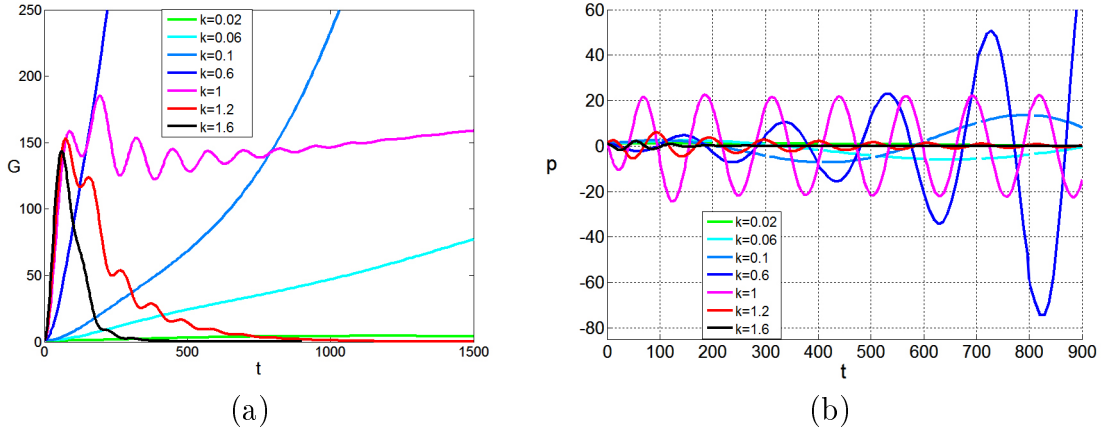
Figure 45: Temporal development of G (a) and $\tilde{p}$ (b) for 900 characteristic time, at fixed spatial point, $x = 10$, $y = 10$, $z = 3$, on varying *wavelength number k*, for $\theta = 60^o$, $\phi = 90^o$, $\beta = 1$ and $Re = 5000$ configuration..

As it is expected to be, the graph shows, for $k = 0.02 \div 1$, an increasing trend, related to a certain instability in time of the flow. The amplification factor continues to increase for many characteristic times, $t = 900$ in this simulation, and does not reach an asymptotic value. This is due to combined effects of $Re = 5000$, that, as said before, identifies an unstable field, and the increasing of *obliquity* and *crossflow* angles, ϕ and θ, toward extreme values. For $k = 0.6$, the G curve significantly and suddenly increases, immediately showing an strong amplification. For high wavelength numbers from $k = 1.2$ to $k = 1.6$, lower values of energy are reached and a transient growth characterizes the initial behaviour. For $k = 0.06$ and $k = 0.1$, G slower goes toward instability state. For $k = 1$, the G first grows and then reaches a mean value around which it fluctuates slowly decreasing its amplitude.

Also for this configuration, figure 45 (b) shows a good correlation with amplification factor curves, on varying wavelength number k. Pressure curves related to intermediate and great wavelengths, with respect to the time, diverge and tend to progressively reach higher values. These configurations reveal an unstable behavior in time, hich could be symptomatic of a "*turbulence blast*". According to this conjecture, the increasing periodic temporal trend of the pressure is meaningful and lead to a great increase of pressure perturbative values. As one can notice, the limit behaviours mentioned above, for $k = 1$ and $k = 0.6$, are significant in this graph, as they presents realy elevated oscillation periods and amplitudes; the first one also shows the same behaviour seen for G, since it reaches an unstable oscillation trend, which tends to significantly increase in time. All the lower wavelength numbers than $k = 1$ presents stable behaviours, reaching the asymptotic zero value for time between $t = 300 \div 900$. Since, for $k = 0.6$, a sudden increase toward a very high maximum point is shown, the pressure related to this wavelength could be the most unstable for this flow. Very low wavelength numbers, $k = 0.02$ and $k = 0.06$, lead to higher oscillation periods and lower amplitudes of the pressure curves, because, as G graph shows, they become unstable after few temporal scales.

Moreover, it is to note that maximum and minimum points for perturbative pressure come before than those related to G. This delay of energy with respect to pressure is noticed in every implemented simulation. This *phase delay* can be justified by the fact that, increasing the perturbative pressure field, the energy field could perceive this variation at few istants laters.

Finally, as far as intermediate and higher wavelength numbers are concerned, it can be say that pressure trend in time reflects the unstable and diverging behaviour we are waiting for. So the field related to $Re = 5000$, great obliquity and crossflow angles and medium-low wavelengths, can be defined unstable.

Pressure curves along x, y and z coordinates are now shown in figure 46, 47 and 50 in order to remarke differences with the stable configuration analysed at the beginning of this section.

The first thing to note is that the curves along x direction, figure 46, are not af-

fected by the disturbance introduced, as it is expected, because now the perturbative wave enters the crossflow boundary layer with an *obliquity angle* $\phi = 90^o$ causing a perturbative component only along the direction orthogonal to the streamline. Moreover, higher values are shown for higher wavelength numbers, as the previous configuration, whereas lower wavelength numbers lead to negative perturbative values.
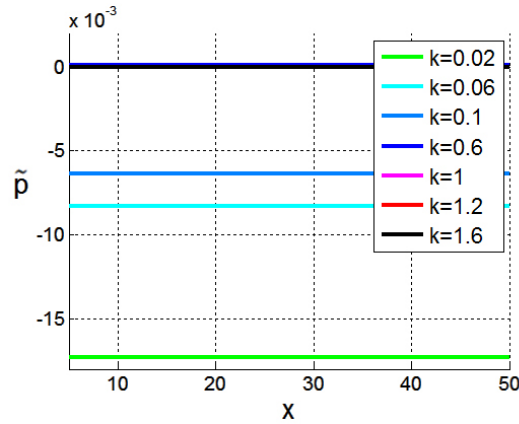
Figure 46: Pressure profiles along x, with fixed $y = 10$ and $z = 3$ on varying *wavelength number* k, at characteristic time $t = 40$, for $\theta = 60^o$, $\phi = 90^o$, $\beta = 1$ and $Re = 5000$ configuration.

In figure 47 (a), perturbative pressure curves along z direction are shown. In this case, the pressure curves are strongly affected by the disturbance introduced, since they have the typical oscillating trend around a mean value. The oscillation amplitudes and periods increase with the decrease of the wavelength number For instance, for $k = 0.1$, perturbative pressure presents an higher point for about $\tilde{p} = 0.075$, lower than the maximum for $Re = 100$ and $\phi = 45^o$. Lower values of wavelength numbers lead to increasing oscillation amplitudes and periods, as previous configuration. Figure 47 (b) shows how pressure amplitudes for small wavelength disturbances are one or two orders of magnitude lower than the higher one and present very short oscillation periods.
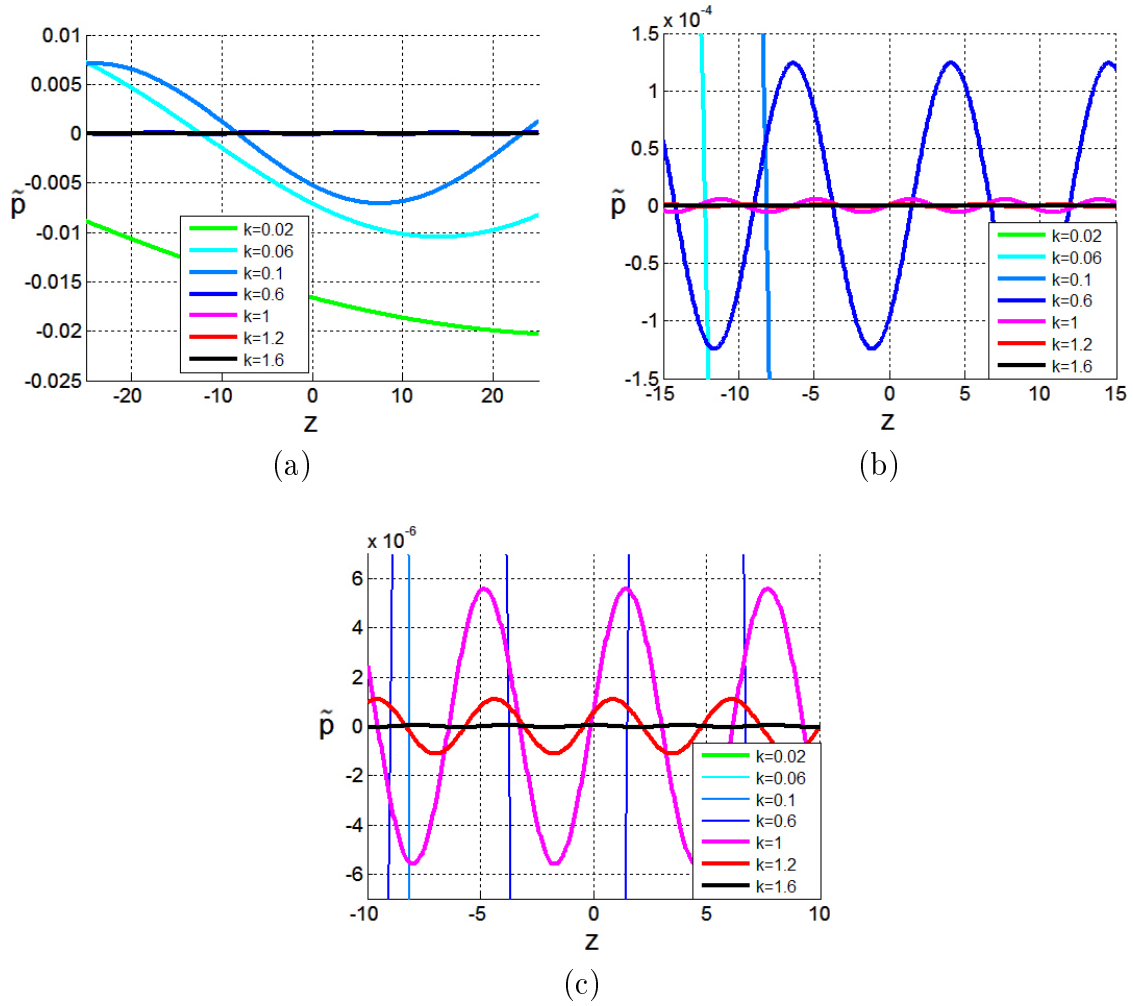
Figure 47: Pressure profiles along z, with fixed $x = 10$ and $y = 10$ (a), on varying *wavelength number* k, and enlargements (b,c), at characteristic time $t = 40$, for $\theta = 60^o$, $\phi = 90^o$, $\beta = 1$ and $Re = 5000$ configuration.

Then introducing the perturbative wave in the direction perpedicolar to the streamlines, it mostly affects that direction and the effect on the longitudinal direction is almost void. This is what it is expected for this configuration and pressure profiles prove it.

Pressure profiles along y coordinate are now shown for three different fixed char-

acteristic times, $t = 15$, $t = 40$, $t = 95$ with enlargements focused on their behaviours at the wall in figure 50 (1a, 2a, 3a and 1b, 2b, 3b). First velocities $\tilde{u}(y)$ and $\tilde{w}(y)$ along direction orthogonal to the wall are presented in figure in order to give an idea of the three-dimensional perturbative velocity profile.

Pressure profiles along y direction orthogonal to the wall are not so different from the previous configuration, showing lower values for lower wavelength numbers, that correspond to higher wave lengths, while higher k present more significant values at wall than before. Proceeding in time, perturbative pressure increases its values inside the boundary layer, as it is expected, due to the "*pressure blast*".

Changes in pressure gradient signs take place more frequently, also for longer wavelehgth, since initial times, as $t = 15$. The maximum points induced by this variations increase significantly in time, for wavelengths from $k = 0.6$ to $k = 1.2$, reaching both negative and positive values due to their temporal oscillations. At $t = 95$, some of this maximum values overtake the pressures ralated to longer wavelengths. Only for $k = 0.06$ and $k = 1.6$ a decrease of their value is noticed, probably suggested a damping of the perturbative pressure in the second case, whereas a translation toward negative value is expected for the first one.

As far as the perturbative pressure profiles thicknesses are concerned, these do not change in time, but their different spatial values are related to the wavenumber considered, as, in general, its decrease lead to more elavated thicknesses. Making a comparison between figures 48, 49 and 50, it is easy to note that the thicknesses of perturbative pressure and velocity profiles are smaller than the ones of perturbative pressures and the velocity profiles related to $Re = 100$ configuration seen previously. This can be related to the fact that the *diffusive component* inside the boundary layer is higher when $Re = 100$ and leads to larger thicknesses for the profiles than $Re = 5000$. On the other hand, as written before, the increase of Reynolds number, together with the previous thickness decrease, leads to greater amplitudes of pressure values than $Re = 100$.
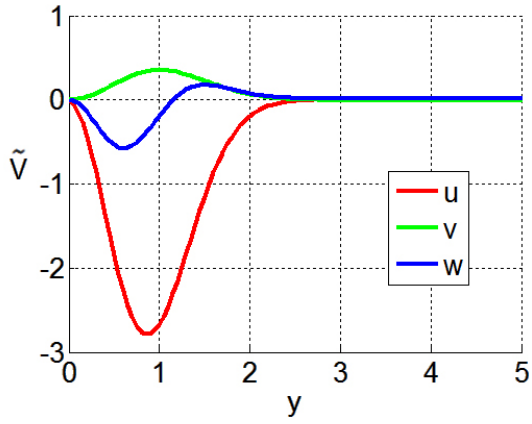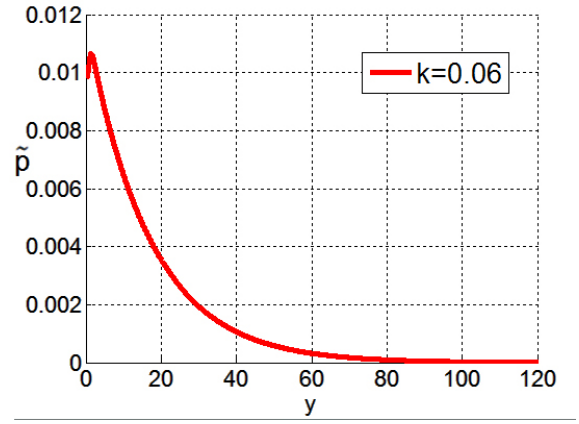
(1a) (1b)
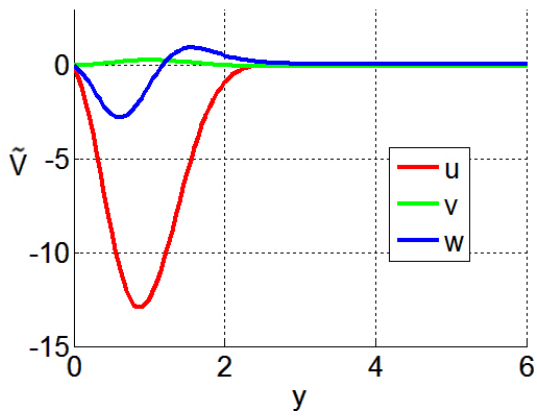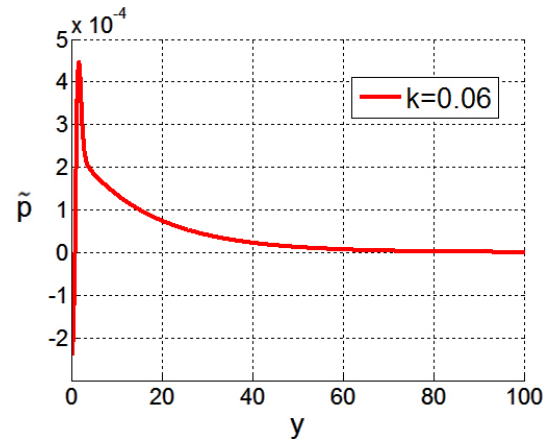
(2a) (2b)

Figure 48: Spatial evolution along y-axis of velocity $\tilde{v} = \tilde{v}(y)$, $\tilde{v} = \tilde{v}(y)$, $\tilde{w} = \tilde{w}(y)$ and pressures $\tilde{p} = \tilde{p}(y)$ (1b, 2b) at times $t_1 = 25$ (1a, 1b), and $t_3 = 95$ (2a, 2b), for $x = 10$, $z = 3$ and $k = 0.06$.
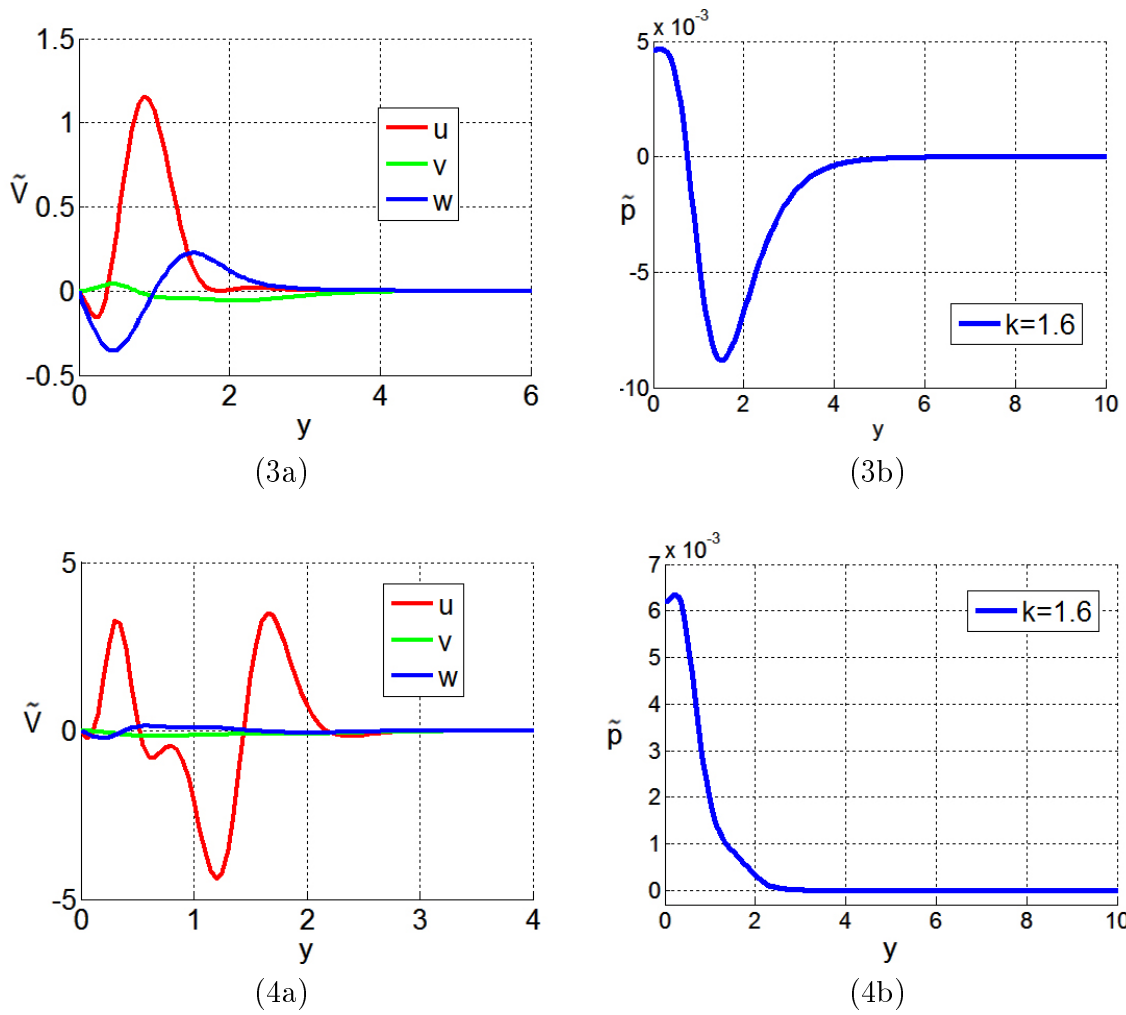
Figure 49: Spatial evolution along y-axis of velocity $\tilde{v} = \tilde{v}(y)$, $\tilde{v} = \tilde{v}(y)$, $\tilde{w} = \tilde{w}(y)$ and pressures $\tilde{p} = \tilde{p}(y)$ (1b, 2b) at times $t_1 = 25$ (1a, 1b), and $t_3 = 95$ (2a, 2b), for $x = 10$, $z = 3$ for $k = 1.6$.

(1a) (1b)

(2a) (2b)

(3a) (3b)
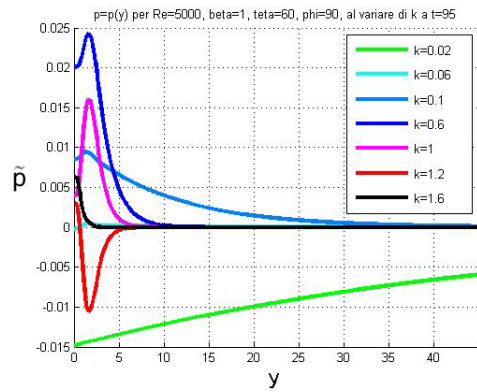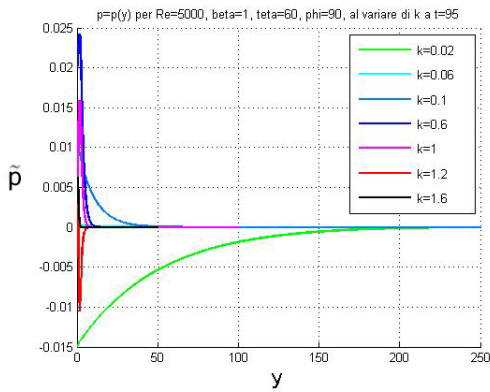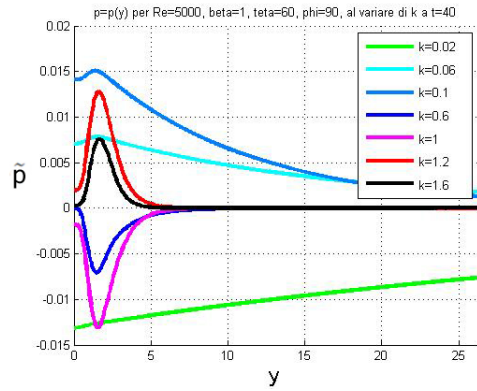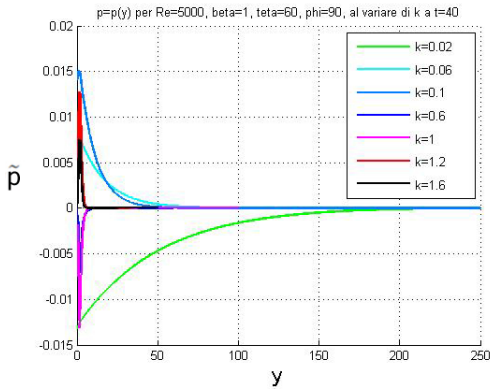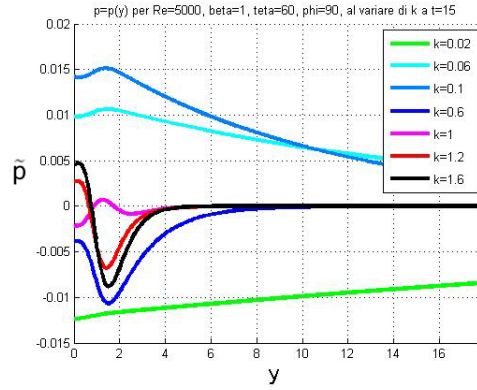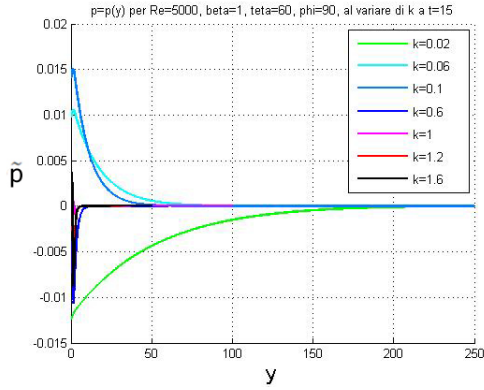
Figure 50: Spatial evolution of pressure $\tilde{p} = \tilde{p}(y)$ at times $t_1 = 25$ (1a), $t_2 = 60$ (2a) and $t_3 = 95$ (3a), for $x = 10$ and $z = 3$, enlargements at wall (1b, 2b, 3b).

Finally, for this configuration, pressure field *bidimensional surfaces* are also shown in figure 51 giving a representation of the pressure field at $Re = 5000$ all over the computational domain.

(a)

(b)

(c)
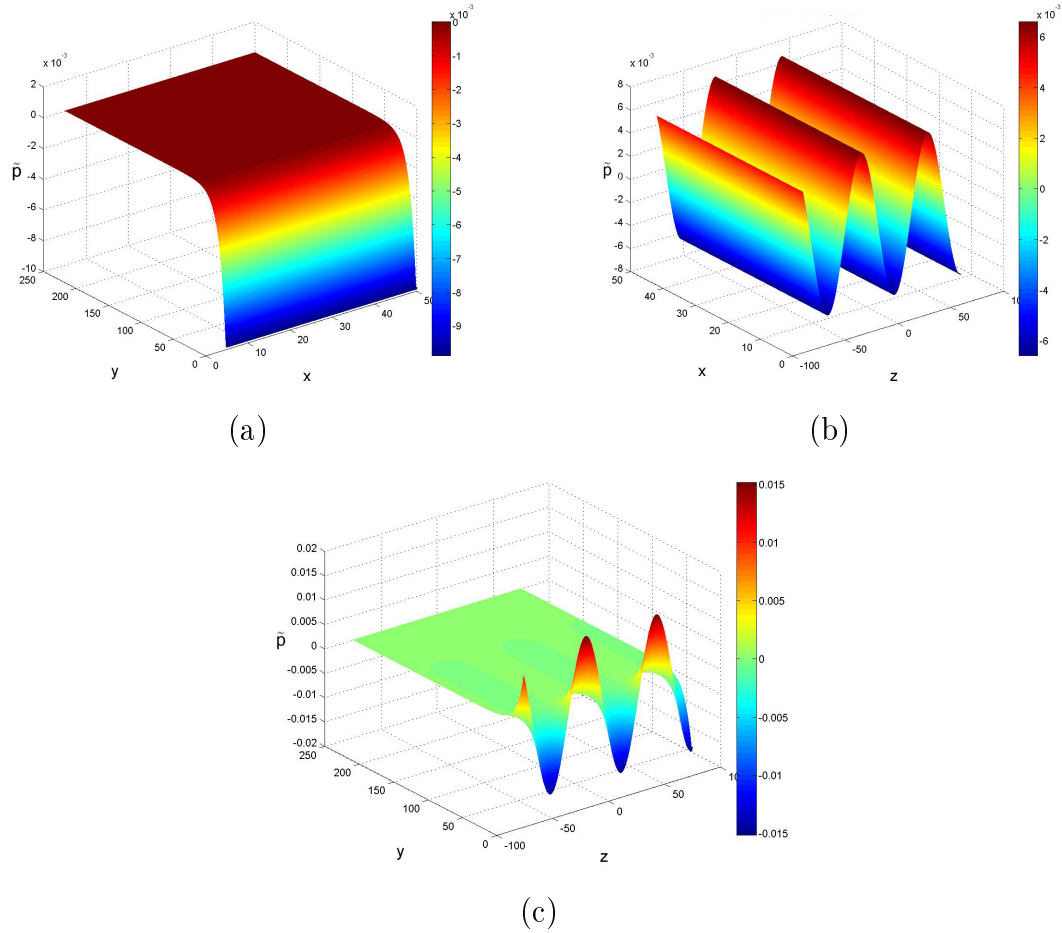
Figure 51: Pressure field *bidimensional surfaces* on $x - y$ (a), $x - z$ (b), $y - z$ (c) planes at $k = 1$ and $t = 60$, for $\theta = 30^o$, $\phi = 45^o$, $\beta = 1$ and $Re = 100$ configuration.

The *oscillating perturbative pressure wave* now goes through the boundary layer along the cross z-direction respect to the streamlines, as it can be clearly noticed, while it is steady along the longitudinal direction. This fact confirms the steatments reported before.

4.2.2 Variation of obliquity angle ϕ

In this paragraph, the effects of the variation of *obliquity angle ϕ* on the perturbative pressure field are shown and investigated. Basing on configuration listed at the beginning of the section, the configuration to be analysed is:

- $\theta = 60^o$, $k = 0.4$, $\beta = 1$ for $Re = 5000$.

Observing which obliquity angle values leads to instability in the crossflow boundary layer is one of the main goals of following simulation.

First of all, the comparison between amplification factor G and pressure curves with respect to time is shown in figure 52, as done in previous section.
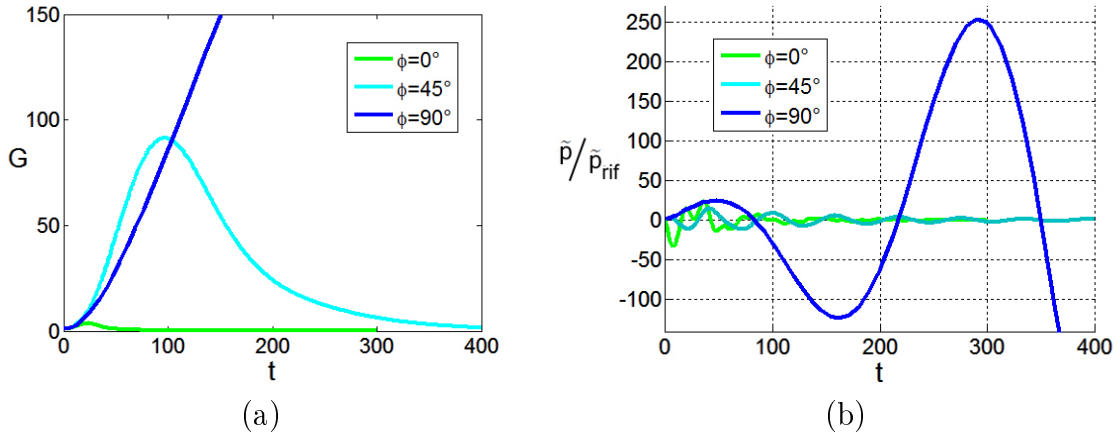
Figure 52: Temporal development of G (a), and $\tilde{p}$ (b) for 400 characteristic time, at fixed spatial point, $x = 10$, $y = 10$, $z = 3$, on varying *obliquity angle ϕ*, for $\theta = 60^o$, $k = 0.4$, $\beta = 1$ and $Re = 5000$ configuration..

The amplification factor graph, in figure 52 (a), shows different behaviours by varying the obliquity angle ϕ. In particular, if the perturbation is introduced with a zero angle with respect to the streamline, $\phi = 0^o$, the G presents only a weak initial transient growth and becomes asymptotically stable at $t = 20$. For $\phi = 45^o$, the G curve presents a slightly higher growth but reaches the stability state at $t = 300$,

when the perturbation blows over, with a maximum of energy at about $t = 90$, but not very elavated. On the contrary, being these previous configurations stable, the third, related to $\phi = 90^o$, is strongly unstable and reaches progressively higher values of the amplification factor. For this obliquity angle, G presents a divergent trend without any initial oscillating transient growth.

In order to find a correlation with the amplification factor trends, a second graph is shown, in figure 52(b), that is the perturbative pressure $\tilde{p}$ curve with respect to time, where $\tilde{p}$ is referred to a initial reference pressure p_{rif} in order to better compare the two quantities.

It is easy to notice that, along 400 characteristic time, the trends expected from the graph of G is confirmed, as longitudinal and oblique disturbances cause a very low pressure increase until $t = 300$ when they reach the asymptotic state, whereas orthogonal waves generate a diverging oscillatory pressure trend along time reaching progressively higher maximum points.

This obliquity angle value $\phi = 90^o$ can be so related to the instability growth and the pressure curves seems to be indicators of a stable or unstable state, being well-interrelated with the amplification factor G. The amplification factor in turn gives an hint about either the growth or the decrease of the pressure field in time. As it is expected, cross waves are the most dangerous because they lead quickly to an explosion of the pressure, which continue to increase reaching very high values.

The last fact to note is that the higher points of the perturbative pressure anticipate the ones of the amplification factor, as the pressure have the first maximum point at $t = 40$, whereas G at $t = 90$ for $\phi = 45^o$.

As far as the spatial developments along x, y, z are concerned, figures 53 and 54 are presented.

First, in figure 53 (a), the curve of perturbative pressure along x direction, at $t = 60$, is shown, by varying the obliquity angle. The domain is not completely drawn because, as one can note, the oscillatory behaviour tends to periodically repeat itself along all the computational field and it is more simple observing a certain region for the analysis of the parameters effects.
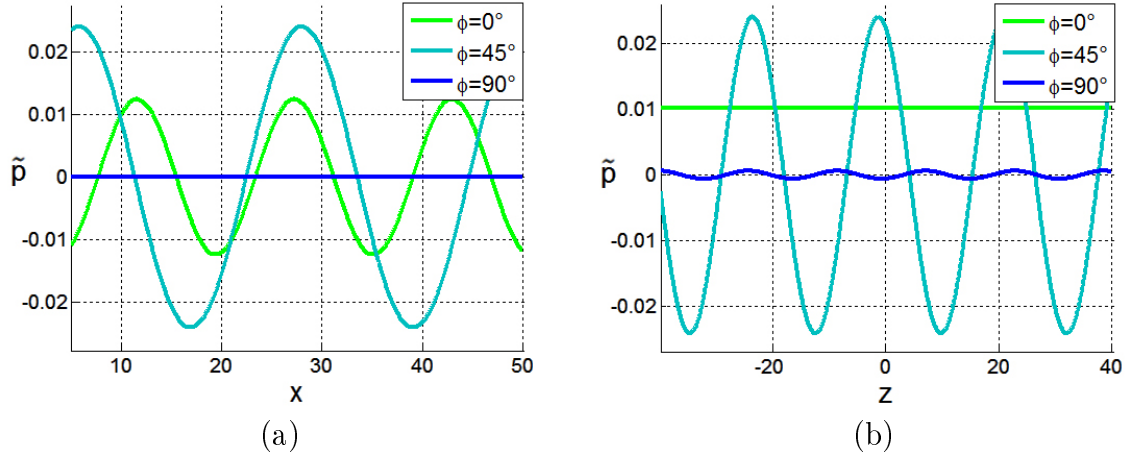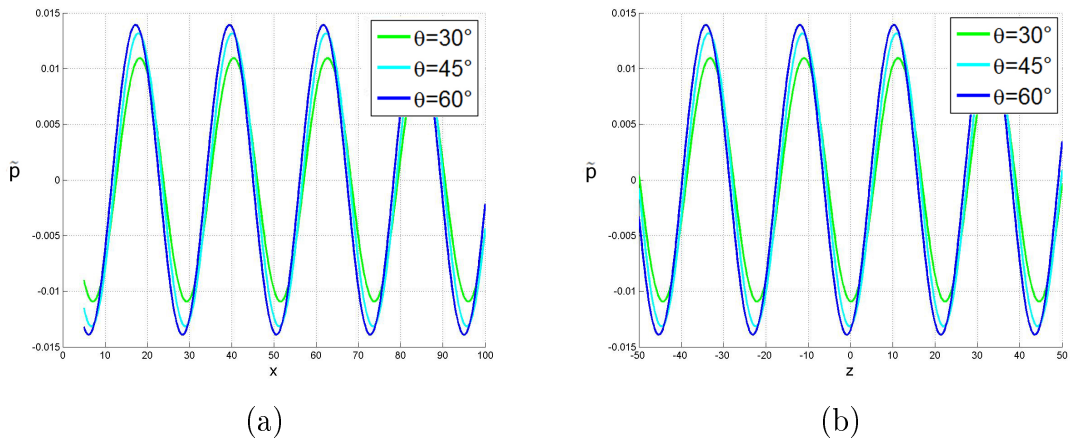
Figure 53: Pressure profiles along x, with fixed $y = 10$ and $z = 3$ (a), and along z, with fixed $x = 10$ and $y = 10$ (b), on varying *obliquity angle* ϕ, at characteristic time $t = 60$, for $\theta = 60^o$, $k = 0.4$, $\beta = 1$ and $Re = 5000$ configuration.

The graph confirms what is expected by varying ϕ, that is a progressive instability caused by the increase of the obliquity angle, the disturbance is introduced with in the three-dimensional boundary layer, along z direction (b), and by the ϕ decrease, along x direction (a). The increasing instability is well highlighted both along x and z coordinate, figure 53 (b), , for $\phi = 90^o$, which represents an orthogonal wave and it is expected to be the most destabilizing along this direction. At the same time, lower values of ϕ cause oscillations in the pressure field along x, where the $\phi = 90^o$ pressure tends to be costant. On the other hand, along z direction, $\phi = 0^o$ pressure become costant, but with an amount slightly higher than zero.

However, it is to noticed that pressure, for $\phi = 0^o$ along x and for $\phi = 90^o$ along z, presents lower oscillation amplitudes and periods than for $\phi = 45^o$, which seems to more affect both the directions, validating what has been observed in section 4.2.1.

Finally, it is important to observed the pressure profiles along y direction, which is a very meaningful coordinate for the boundary layer. Graphs are drawn for three different fixed time, $t = 25$, $t = 60$, $t = 95$, and x, z coordinates in order to analyse the pressure development at different istants.

Thanks to the enlargements of the domain, figure 54 (1b, 2b, 3b), one can notice that $\tilde{p}$ cancels out for $y = 5 \div 7$ at all the times in the $\phi = 90^o$ configuration, whereas the others present a zero value for $y = 3$. When the perturbative pressure $\tilde{p}$ tends to zero value it means that the disturbance fully dissolves going outside the boundary layer where, if the base flow pressure value P is superimposed, the mean field pressure quantity must be found.

The main changes, figure 54 (1a, 2a, 3a), on varying the obliquity angle, are noticed for the pressure values at wall and for the sign of maximum points from time to time. The greatest values of perturbative pressure are shown for $\phi = 90^o$ again, which generate important growths inside the bounadry layer, leading to peaks about $2 \div 4\%$ higher or lower than the mean reference quantity. Furthermore, it is to note that $\tilde{p}$, for a cross wave, oscillates from positive $\tilde{p} = 0.3$ at $t = 25$ to negative $\tilde{p} \simeq -0.3$ to $t = 60$, until an higher negative value of $\tilde{p} \simeq -0.45$ reaching 100 characteristic times; this confirms that the flow is increasingly reaching an unstable state. At $t = 60$, figure 54 (b), a sudden change in pressure gradient $\partial \tilde{p}/\partial y$ is noted and may be necessary to carry back pressure to outer value.

Decreasing the obliquity angle ϕ, instead, significant changes in pressure are mainly noted at $t = 25$, when the perturbation is strongly developed for this configurations. For $\phi = 45^o$ the pressure at wall is 15% higher then the asymptotic value. On contrary, at $t = 95$ perturbative pressures almost null, since they have reached their temporal asymptotic state.
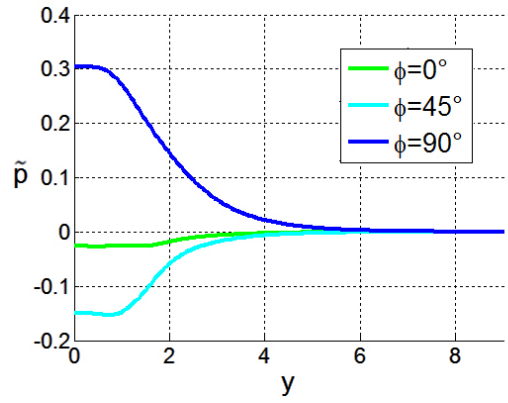
(1)
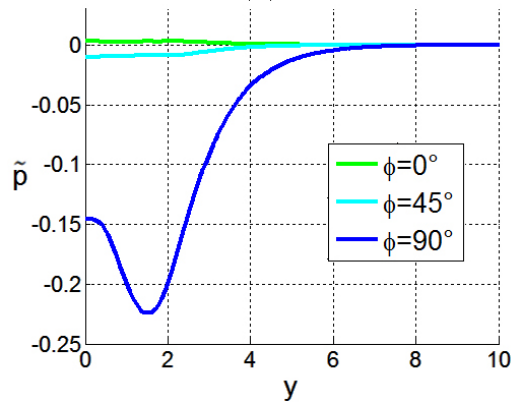
(2)
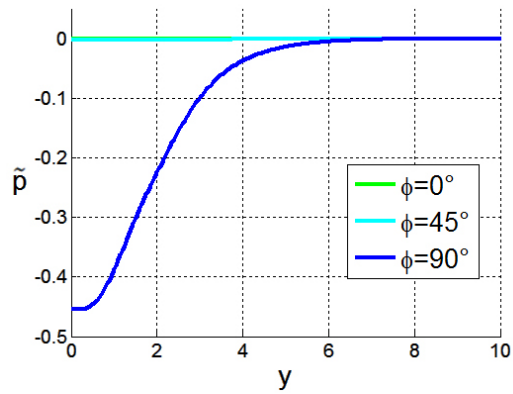
(3)

Figure 54: Spatial evolution of pressure $\tilde{p} = \tilde{p}(y)$ at times $t_1 = 25$ (1), $t_2 = 60$ (2) and $t_3 = 95$ (3), for $x = 10$ and $z = 3$.

4.2.3 Variation of crossflow angle θ

The effects of the variation of *crossflow angle* θ on the perturbative pressure field are now shown and investigated. Basing on configuration listed at the beginning of the section, the configuration to be analysed is:

- $\phi = 45^o$, $k = 0.4$, $\beta = 1$ for $Re = 5000$.

This analysis is very similar to the previous one and is achieved in order to comprehend how the θ characteristic parameter, linked to crossflow streamwise direction, could affect the pressure field, in time and space, and if could lead to an unstable state, in term of pressures, as disturbances obliquity angleϕ.

The same scheme of analysis is followed again starting from the amplification factor G graph, which gives an information about either the growth to an unstable state of the flow or the achievement of an stable state. In figure 55 below a comparison between the G and p/p_{rif} is presented.
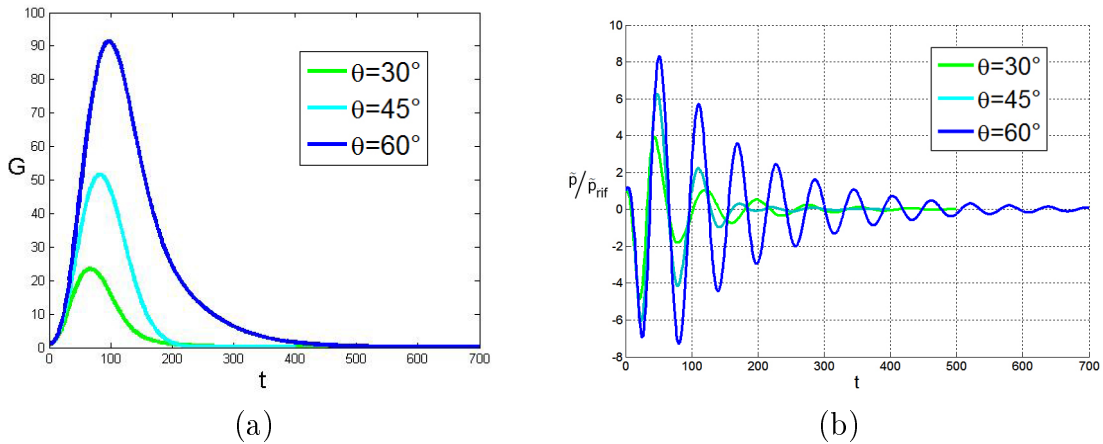
Figure 55: Temporal development of G (a), and $\tilde{p}$ (b) for 100 characteristic time, at fixed spatial point, $x = 10$, $y = 10$, $z = 3$, on varying *crossflow angle* θ, for $\phi = 45^o$, $k = 0.4$, $\beta = 1$ and $Re = 5000$ configuration.

111

For the considered configuration corrisponding to an intermediate wavelength $k = 0.4$ and perturbation introduction angle $\phi = 45^o$, increasing θ, the amplification factor progressively tends to a growing initial transient growth. In figure 55 (a) this is clearly drawn, as, for$\theta = 30^o$ and $\theta = 45^o$, G after an higher point begins to decade toward an asymptotic state, that is the typical transient growth behaviour toward the stability condition, whereas, for $\theta = 60^o$, when the flow is strongly inclined, G maximum point becomes doubly greater than the previous $\theta = 45^o$ value. In general the variation of the crossflow angle leads the G maximum point to increase twice and the transient behavior to grow.

This behaviour is noticed also in the p/p_{rif} temporal diagram in figure 55 (b), in which curves for $\theta = 30^o$ and $\theta = 45^o$ differently tend to the stable asymptote, characterizing the annulment of the perturbation, for $t = 300 \div 400$, while $\theta = 60^o$ clearly leads the pressure toward a greater oscillating transient, which presents oscillating pressures for longer time, until $t = 700$. However, also this crossflow angle value is related to stability, since it reaches the asymptotic mean zero quantity for long times.

As far as the maximum points are concerned, also in this simulation it is to notice that the ones concerning the pressure temporal curves are shown, at $t = 40 \div 50$, before the peaks of G, at $t = 60 \div 70$ and $t = 100 \div 110$. Moreover, higher maximum points are shown for $\theta = 60^o$, even if they are progressively smaller in time, and in general increasing crossflow angle θ leads to higher maximum and lower minimum points respectively. For $\theta = 30^o$ and $\theta = 45^o$, maximum variations in perturbative pressure correspond to about 4% and 6% with respect to the asymptotic value, respectively. Not only the amplitude of oscillating pressures increases, but also their oscillating periods, leading to progressively longer transient times until an instability behaviour.

This first comparison completely confirm what it is expected on varying the crossflow angle, since the influence of θ on the perturbative pressure is very close to that of the obliquity angle ϕ, even if it do not lead to the pressure blast and instability state; in general, however, combined extreme values of these angles lead

to a diverging pressure temporal trend. For instance, two unstable configuration have been noticed in the numerical simulations of both $\theta = 30^o$, $\phi = 0^o$ and $\theta = 60^o$, $\phi = 90^o$ configurations, which will be further investigated in the next chapter.

In order to validate this statement the spatial behaviour of perturbative pressure $\tilde{p}$ is now analysed. In figure 56 pressure developments along x (a) and z (b) coordinates are drawn.

(a)   (b)

Figure 56: Pressure profiles along x, with fixed $y = 10$ and $z = 3$ (a), and along z, with fixed $x = 10$ and $y = 10$ (b), on varying *obliquity angle* ϕ, at characteristic time $t = 15$, $\phi = 45^o$, $k = 0.4$, $\beta = 1$ and $Re = 5000$ configuration.

The pressure trends along both directions being equally affected since an intermediate obliquity angle $\phi = 45^o$ is taken into account, the graphs are similar presenting the typical oscillating trend around a mean value. The oscillations of perturbative pressure around the mean value, instead, are equal and reach the same maximum and low points in both directions. As for the temporal evolution, the effects of the crossflow angle on pressures along x and z directions cause a growth in oscillating amplitude, but not in spatial periods. Increasing the crossflow angle higher perturbative values are reached, until about 0.015 respect to mean value, but changes seem to be not really significant.

Finally, pressure development along the direction orthogonal to the wall is investigated, figure 57. The simulations are made again for three different fixed times $t = 15$, $t = 40$ and $t = 95$, that is when the disturbance is completely developed and almost disappeared respectively.

As for other simulations, perturbative pressure $\tilde{p}$ shows oscillations from negative to positive values developing in time and this fact is noticed in this one too.

Focusing on effects of changing in crossflow angel θ, the usual increase or decrease in maximum or minimum values is shown, when this angle is increased or decreased respectively. For instance, higher pressure values take place for $\theta = 60^o$ as it is expecetd. These maximum values decrease significantly at $t = 95$, even if it preserves a certain variation in its values. Pressures present changings in slope at every oserved time and for the lowest crossflow angle $\theta = 30^o$ pressure quantities are very small.

Moreover, it is to notice that the disturbance of the pressure cancels out, along y coordinates, at $y = 15$ at all the times, so θ does not affect the reaching of the symptotic value along y coordinate.

Finally, it can be said that the crossflow angle θ affects the pressure field leading it to instability state, but variation, on vaying θ, are less significant than the effects of other characteristic parameters. For certain configurations, called "extreme" in this section, as $\theta = 30^o$, $\phi = 0^o$ and $\theta = 60^o$, $\phi = 90^o$, the instability is shown, leading to a progressive increase in pressure along time and higher maximum and minimum values.

114

(1)

(2)

(3)
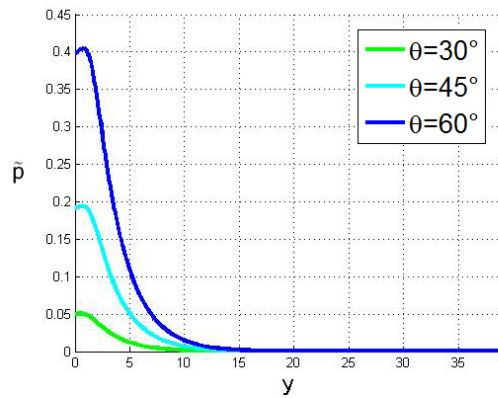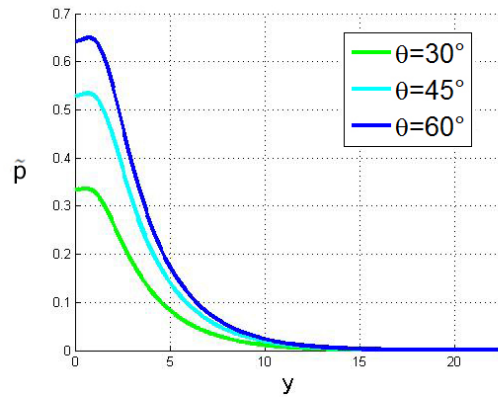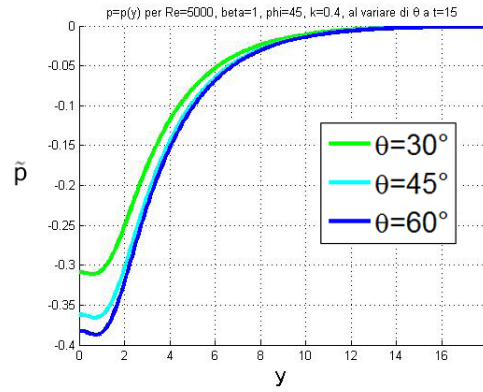
Figure 57: Spatial evolution of pressure $\tilde{p} = \tilde{p}(y)$ at times $t_1 = 15$ (1), $t_2 = 40$ (2) and $t_3 = 95$ (3), for $x = 10$ and $z = 3$.

4.2.4   Variation of pressure gradient β

In this last paragraph, the effects of the variation of *pressure gradient* β on the perturbative pressure field are now shown and investigated. Basing on configuration listed at the beginning of the section, the configuration to be analysed is:

- $\theta = 30^o$, $\phi = 0^o$, $k = 0.1$ for $Re = 5000$

First, the comparison between the amplification factor G and the $p/p_{rif}(t)$ graphs is shown, by varying the pressure gradient β from a negative value, $\beta = -0.1988$, related to a positive pressure gradient $\partial p/\partial x > 0$ along x axis and so to decelerated destabilized flow, to a positive value, $\beta = 1$, related to an accelerated, being $\partial p/\partial x < 0$, and stabilized flow. This fact is well-rendered in figure 58 (a) and (b), where the trends of both quantities diverge for different β.

(a)   (b)
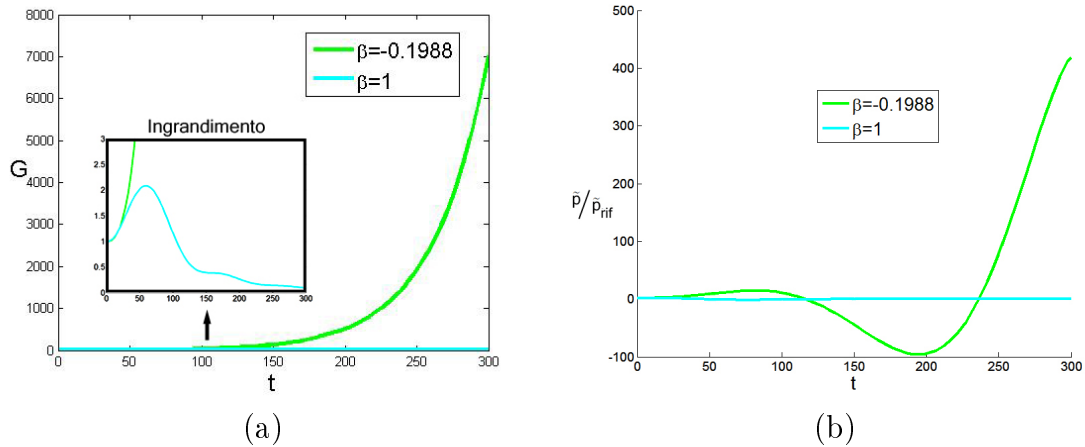
Figure 58: Temporal development of G (a), and $\tilde{p}$ (b) for 100 characteristic time, at fixed spatial point, $x = 10$, $y = 10$, $z = 3$, on varying *pressure gradient* β, $\theta = 30^o$, $\phi = 0^o$, $k = 0.1$ and $Re = 5000$ configuration.

In particular, for 300 characteristic times considered, negative pressure gradient leads to instability, as it can clearly seen in figure 58 (a), since the related curve

goes toward a progressive higher value, whereas a positive value of β presents an asymptotic stable state for G, that slightly changes respect to its initial value, as shown in in figure 58 (a) enlargement. These trends are shown also for the pressure development in time, figure 58 (b), for a fixed spatial coordinate. A negative pressure gradient leads to a strong growth of the perturbative pressure, which tends to progressive higher values. An oscillation near $t = 100$ is noticed, which causes an high maximum point of the pressure, about 15% higher than the asymptotic condition. This higher point, as it is expeeced, only anticipates a further pressure growth at longer simulation characteristic times, $t = 300$. A positive pressure gradient, instead, quickly takes the pressure to extinguish, at about $t = 300$, as seen for G, and variation around the mean value are really lower than the negative pressure gradient configuration. For the first case, the transient is characterized by a strong increasing trend, while the second presents an almost steady value at the beginning and then, from $t \simeq 25$ to $t = 70$, the pressure decays to very low quantities.

The destabilizing effect of a negative β, which leads the flow to decelerate along x direction, is so first confirmed from this analysis. Pressure field greatly grows under the effects of this positive pressure gradient, causing a strong deceleration which makes the flow unstable. A positive β, instead, helps the flow to become stable, damping in time the perturbative pressure.

As far as the pressure development along x and z coordinates are concerned, figure 59 (a) and (b) respectively are introduced.

It is to notice that, for this particulare configuration, where disturbances are lengthwise introduced into a flow with a very small crossflow angle, oscillations are present only along the longitudinal direction, but not along cross-direction.

117

(a)   (b)
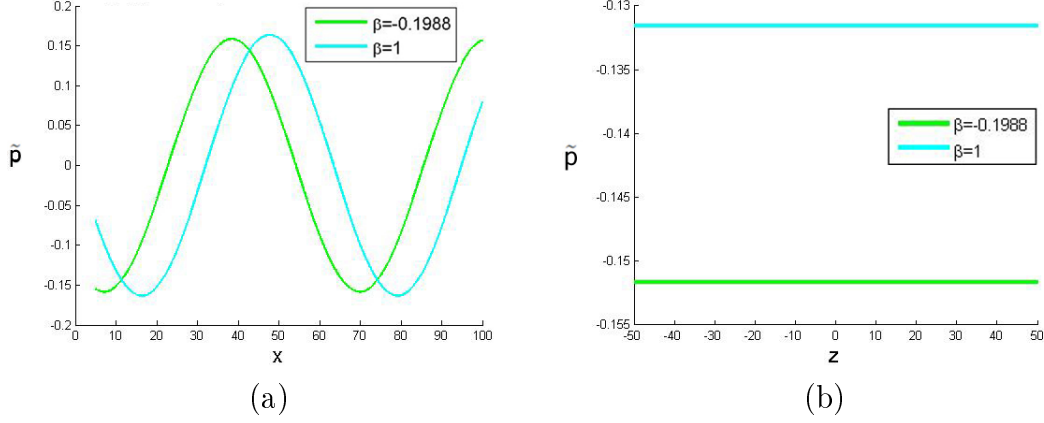
Figure 59: Pressure profiles along x, with fixed $y = 10$ and $z = 3$ (a), and along z, with fixed $x = 10$ and $y = 10$ (b) on varying *pressure gradient* β, at characteristic time $t = 15$, for $\theta = 30^o$, $\phi = 0^o$, $k = 0.1$ and $Re = 5000$ configuration.

The graph in figure 59 (a) precisely shows the perturbed direction and pressure has the typical oscillating trend, which changes only in phase and slightly in amplitude, but not in period. In particular, $\beta = 1$ pressure has a phase delay with respect to the one for $\beta = -0.1988$. On contrary, pressure along z coordinate, figure 59 (b), does not present oscillations, but only a translation of perturbative pressure steady value caused by its phase delay for a fixed x, y point by varying β.

Finally, pressure curves along y direction are shown at three fixed times $t = 15$, $t = 40$ and $t = 95$ and fixed coordinates, $x = 10$ and $z = 3$.

At $t = 15$, figure 60 (a), perturbative pressures, by varying β, present similar profiles, except for the starting values close to the wall, where pressure for $\beta = -0.1988$ has a lightly lower value.

At $t = 40$, figure 60 (b), pressure profiles are very different since $\beta = -0.1988$ leads pressure to a lower negative starting value, $\tilde{p} = -1$ and to cover a larger position of the y domain, $y \simeq 70$, to reach the asymptotic null state, when it cancels out. On the other hand, for $\beta = 1$, the variation along y direction and starting value are significantly reduced, as seen in figure 58 (b).

118
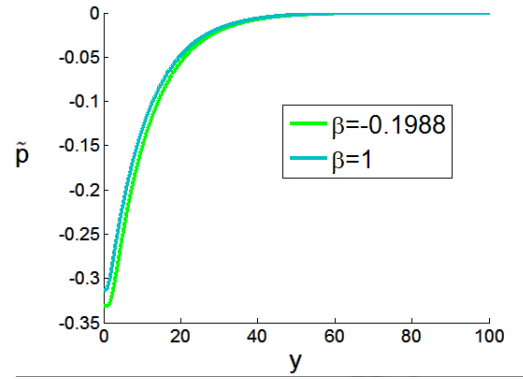
(a)
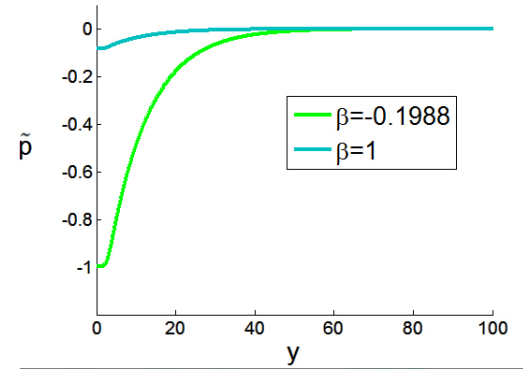
(b)
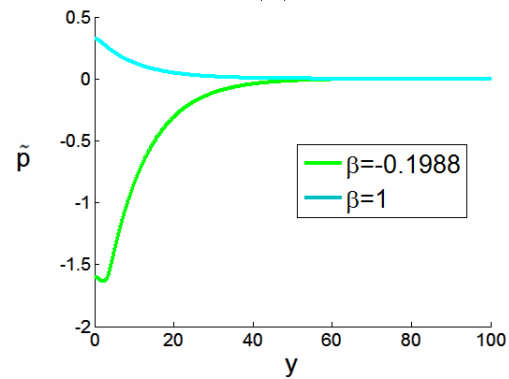
(c)

Figure 60: Spatial evolution of pressure $\tilde{p} = \tilde{p}(y)$ at times $t_1 = 15$ (a), $t_2 = 40$ (b) and $t_3 = 95$ (c), for $x = 10$ and $z = 3$, on varying *pressure gradient* β, for $\theta = 30^o$, $\phi = 0^o$, $k = 0.1$ and $Re = 5000$ configuration.

At $t = 95$, figure 60 (c), pressures for the two configurations completely diverge, since, for $\beta = 1$ and higher characteristic times, pressure continues to oscillate around a value very close to zero, positive here, whereas for $\beta = -0.1988$ pressure reaches a lower negative starting value diverging progressively in time.

The pressure gradient parameter so can affect the pressure field and lead to an "*explosion*" of its values, causing instability phenomena. This fact is well-rendered if the temporal development of perturbative pressure is observed, but also along y ccordinate the pressure shows significant changes, on varying β. Ultimately it has been noticed and proved that a positive pressure gradient, $\beta = -0.1988$, greatly affects the pressure field and causes an instability state for the flow. Because of that, this case will be taken into account in the next chapter, where two unstable dimensional configurations will be analysed in order to investigate the effects of the superimposition of this perturbative pressure field on a dimensional pressure mean field.

5 Mean and perturbative pressure field dimensional analysis

In the previous chapter, the dimensionless perturbative pressure field has been investigated, by varying different characteristic parameters, in order to understand how the introduced disturbances rule the perturbative pressure affecting the crossflow boundary layer. This kind of analysis has been achieved as dimensionless because it was easier to compare different characteristic parameters effects on the perturbative flow in that way. Moreover, only the perturbative pressure field has been taken into account and no mean field, related to the base flow, has been added, refering all quantities to a null mean value.

In this chapter, the mean pressure field is introduced and added to the perturbative field. Furthermore, these two fields are made dimensional in order to achieve real and functional pressure quantities. This investigation can be useful not only in the context of *fluid dynamics*, but also for *structural* and *aeroelastic applications*, since real physical values will be given.

5.1 Dimensional problem

As written in section 3.2, the *total pressure field* is given by the superimposition of mean and perturbative fields, as:

$$p = P + \tilde{p}$$

where p is the total field pressure, while P and $\tilde{p}$ are the mean field and perturbative field pressures respectively. It is assumed that P is only depending on x coordinate, being steady on y and z directions:

$$P = P(x)$$

whereas is well-known that the perturbative pressure is $\tilde{p} = \tilde{p}(x, y, z, t)$.

Thus, P depends only on the x-coordinate and this will be the assumption used in the following analysis for the base flow pressure field.

Moreover, in chapter 4, precisely in section 4.2.3, it has been noticed that two simulations are to be considered very unstable, that is $\theta = 30^o$, $\phi = 0^o$ and $\theta = 60^o$, $\phi = 90^o$. These configuration will be now presented through dimensional quantities and it is expected that they could affect the mean pressure field the most. From the previous chapter, furthermore, it has been found that a negative β, linked to a positive pressure gradient along x-axis, causing a deceleration of the flow, can mostly improve the growth of the perturbative pressure field. The value $\beta = -0.1988$ is then also taken into account together with the ones reported above, since the goal of the dimensional analysis is to observe the effects of the most destabiling perturbative pressure waves on the base flow.

It is to notice, figure 61, that if an airfoil is considered, $\beta = -0.1988$ matches the pressure gradient at 50% of the airfoil chord, where the pressure is increasing, while the velocity decreases. This is the spatial point ehere we put the origin of x-axis for the following configurations. It is assumed that, starting from this point, the mean pressure increases up to the trailing edge, where it reaches the fixed pressure outer value.
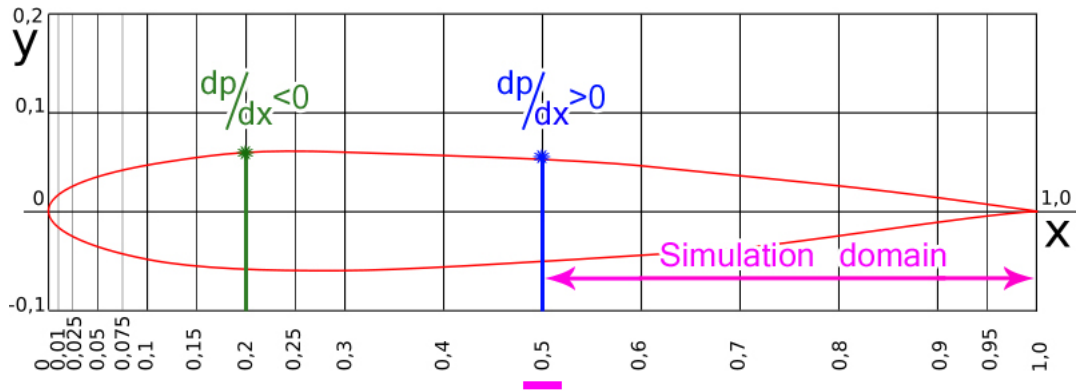
Figure 61: Generic airfoil taken into account in the numerical simulation with shown pressure gradients and simulation domain.

In particular, this analysis is refered to an airfoil of about $1\,m$ chord, infinite spanwise and dipped into a *zero-level standard enviroment*:

$$\begin{cases} p_\infty = 1\,atm = 101350\,Pa \\ \rho_\infty = 1.225\,^{kg}/_{m^3} \\ \nu = 1.5 \cdot 10^{-5}\,^{m^2}/_s \end{cases}$$

These can be the conditions of an experimental test implemented in a medium-size *wind tunnel* at T_{amb} with free flow speed U_∞ related to the chosen $Re_{\delta*} = 5000$, that is:

$$U_\infty = \frac{Re_{\delta*}\nu}{\delta*} = 210.4626\,^{m}/_s \simeq 757.665\,^{km}/_h$$

So the mean pressure profile along x coordinate, having an increasing trend, must reach the outer value, $p_\infty = 10135\,Pa$, at trailing edge, which takes place $0.5\,m$ far from the starting simulation point at $^{x}/_c = 0.5$.

The mean pressure then must have an increasing trend along x and this is reached by the introduction of the approximation suggested by *Rosenhead* [10] for a steady flow inside a boundary layer on a revolutionary surface near the stagnation point. The base idea is to introduce a series expansion along x coordinate for the velocity of the base flow:

$$U(x) = u_1 x + u_2 x + u_3 x + ...$$

which can reduce as:

$$U(x) = U_m x^m$$

where the reference velocity is $U_m = U_\infty$ in this specific case and x is the spatial variable used in the actual numerical simulation. The m parameter is, instead, linked to the pressure gradient parameter β as:

$$\beta = \frac{2m}{m+1}$$

and, for $\beta = -0.1988$, $m = -0.0904$, while $m = 1$ for $\beta = 1$.

This expression of $U(x)$ can be introduce in the *Bernoulli formulation* in order to make the pressure gradient along x direction explicit, as shown below:

$$\frac{\partial P}{\partial x} = -\rho U \frac{\partial U}{\partial x}$$

$$\frac{\partial P}{\partial x} = -\rho U_\infty^2 m x^{2m-1}$$

and through the integration of this expression, the dependence of the mean field pressure P on x coordinate is obtained:

$$P(x) = -\rho U_\infty^2 x^{2m} + c$$

where the integration costant c can be achieved fixing a *boundary condition*, that is related to the free stream pressure value at the end of the airfoil. As said above, the pressure is assumed to be equal to its outer value when the x coordinate is exactly at $x = 0.5\,m$, starting from $^x/c = 0.5$. So the boundary condition introduced is:

$$P(x_{t.e.}) = p_\infty$$

In this way the pressure of the base flow tends to its outer value at the end of the computational domain, as it will be observed next in the graphs showing the trend of mean pressure field along x axis.

5.1.1 Dimensional quantities

As far as the simulation quantities are concerned, perturbative pressures are made dimensional, basing on formulations given at the beginning chapter 4, with respect to the characteristic quantity ρU_∞^2 and become:

$$\tilde{p}_{dim}[Pa] = \tilde{p} \cdot \rho U_\infty^2$$

On the other hand, time t_{dim} is made dimensional as:

$$t_{dim}[s] = t \cdot t_{car}$$

where t_{car} is:

$$t_{car} = \frac{\delta^*}{U_\infty} = 1.69 \cdot 10^{-6}\ s$$

In the formulations above, as in in the previous paragraph, U_∞ is achieved from the linked Reynolds number $Re_{\delta+} = 5000$, being the value of *displacement thickness*, δ^*, of the boundary layer well-known. This can be obtained from [11]:

$$\delta(x) \approx \frac{4.99 \cdot x}{\sqrt{Re_x}}$$

where $Re_x = \left(Re_{\delta^*}/1.72 \right)^2$ and x is taken fixed at $x/c = 0.5$. So the thickness of the boundary layer is:

$$\delta(0.5c) \approx 0.00086\ m$$

and then:

$$\delta^*(x) \approx 0.346 \cdot \delta(x)$$

which is, at $x/c = 0.5$:

$$\delta^*(0.5c) \approx 0.0002975 \; m$$

Now x, y, z coordinates can be made dimensional with respect to $\delta^*(0.5c)$ as:

$$\begin{cases} x[m] = x \cdot \delta^*(0.5c) \\ y[m] = y \cdot \delta^*(0.5c) \\ z[m] = z \cdot \delta^*(0.5c) \end{cases}$$

5.2   Simulation results

This is the actual chapter main section, as section 4.2 was in the previous one. In order to compute the *total pressure field* numerical simulation on MATLAB are newly implemented superimposing the *dimensional perturbative pressure field*, dimensionless analysed in section 4.2, to the *mean pressure field* of the base flow, as explained above. This methodology refers to the METHOD OF SMALL DISTURBANCES described in section 2.2.1, which introduces small disturbances in a mean field and leads to compute the total field quantities.

In particular, two flow configurations, as written previously, are taken into account, since they are unstable:

1. $\theta = 30^o$, $\phi = 0^o$, $\beta = -0.1988$, $Re = 5000$

2. $\theta = 60^o$, $\phi = 90^o$, $\beta = -0.1988$, $Re = 5000$

Both the cases are computed for four different values of *wavenumber k*, being this the characteristic parameter affecting the most the crossflow boundary layer stability and pressure trends:

$$k = [\, 0.06\,,\, 0.4\,,\, 1\,,\, 1.6\,]$$

First of all, for both flow typologies, the graph related to mean flow pressure, costant along y, z and varying only along x-coordinate, is shown with the graph showing the superimposed perturbative pressure. Then total pressure field behaviours, in space and time, are drawn mainly in order to give an idea of orders of magnitude caused by the disturbances introduction. It is important to remember that, since destabilizing perturbative flow configuration have been identified in previous parametric analysis, now the focus is on the trends and achieved real values of the total pressure field.

The numerical simulations are investigated up ahead.

5.2.1 Simulation for $\theta = 30^o$, $\phi = 0^o$, $\beta = -0.1988$, $Re = 5000$

As it has been said at the beginning of the chapter, mean pressure P changes only along x-coordinate with a positive pressure gradient $\partial P/\partial x > 0$, at fixed $x/c = 0.5$, which identifies an un-favorable contribution to stability, up to the end of the considered airfoil section $1\,m$ long. This trend is very clear in figure 62 (a), where the pressure increases until the freestream pressure atmosferic value.

(a)   (b)
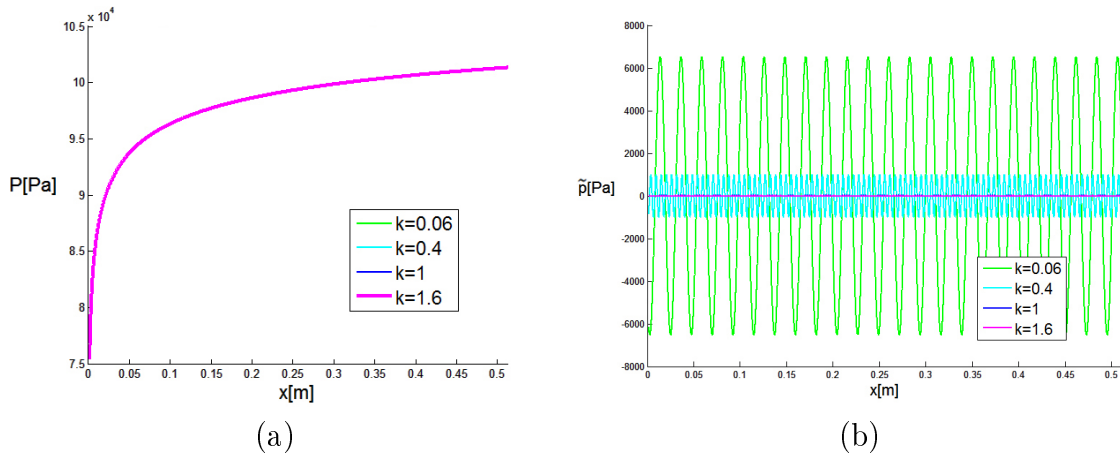
Figure 62: Mean pressure (a) and superimposed perturbative pressure (b) along x-coordinate, belonging to $0.5\,m$ long computational domain and starting from $x/c = 0.5$, for $\theta = 30^o$, $\phi = 0^o$, $\beta = -0.1988$ and $Re = 5000$, with fixed $x = 10 = 3.46\,mm$, $z = 3 = 1.04\,mm$ and initial $t \approx 1.69 \cdot 10^{-5}\,s$.

Alongside of the mean pressure graph, the superimposed perturbative pressure is drawn in figure 62 (b). As it can be noticed and expeceted, the greater disturbances are shown for higher wavelengths, $k = 0.06$, both in terms of ampltudes and oscillation periods, even if these perturbative pressures are one order of magnitude, $\tilde{p} \geq 6000\,Pa$, lower than mean pressures, $P = 7,5 \cdot 10^4 \div 10,135 \cdot 10^4$. Shorter wavelengths are even lower, $\tilde{p} \approx 1000\,Pa$, and expected to less affect the mean flow. Finally, for k=1.6 the disturbe is very small, as it slightly fluctuates around the mean value.

Basing on these conjectures, the results about the total pressure field are now

shown. In figure 63, the *total pressure p* along x-coordinate with fixed y, z are drawn and the expected effects are now observed.

$$(1) \qquad\qquad (2)$$
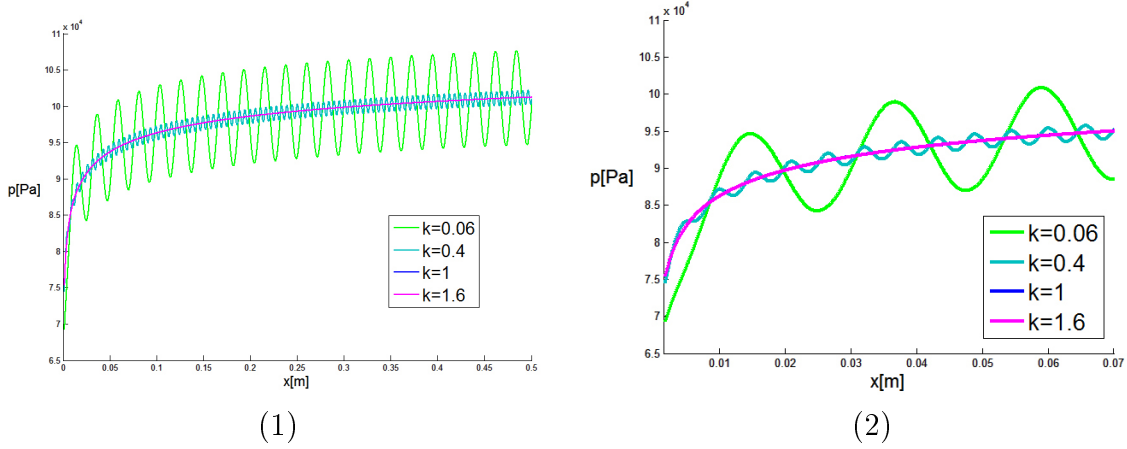
Figure 63: Total field pressure p along x-coordinate with fixed $y = 10$, $z = 3$ and initial t, (1) and enlargement close to the computational starting point for $x = 0 \div 0.07\,m$ (2) for $\theta = 30^o$, $\phi = 0^o$, $\beta = -0.1988$ and $Re = 5000$.

These results confirm the significant influence of longer wavelengths on the mean pressure field. As it can be noticed high positive and negative variations, about $\Delta p = \pm 4000\,Pa \approx \pm 0.039\,atm$, of the pressure are reached with respect to the mean value and the oscillating trend equally repeats itself along all the computational domain, until $x = 0.5\,m$, when it reaches the $p = p_\infty$. For $k = 0.4$, instead, changes are more contained than before. The influence on the flow and the oscillation period have significantly decreased. Proceeding toward smaller wavelengths, these do not affect the mean flow, as their disturbance values are really smaller than the mean pressure field, and the base flow pressure remains almost unchanged.

As far as the oscillation periods and the wavelengths are concerned, in figure 63 (2) the enlargment of the region close to initial computational point clearly shows lengths of the perturbative pressure waves of, that are for $k = 0.06$ and $k = 0.4$ $2\,cm$, for $k = 0.06$, and $5\,mm$ long, for $k = 0.4$, but their fluctuations around the mean quantity are very different, as said just above.

The higher pressure values are obviously achieved close to the trailing edge of the airfoil, where the increasing pressure gradient $\partial P/\partial x$ leads also pressure fluctuations to significantly increase. In this region pressure values of about $p \simeq 10,77 \cdot 10^4 \, Pa$ are achieved, representing an increase of $\pm 0.1 \, atm$ with respect to the mean value, which corresponds to an altitude variation of about $1000 \, m$.
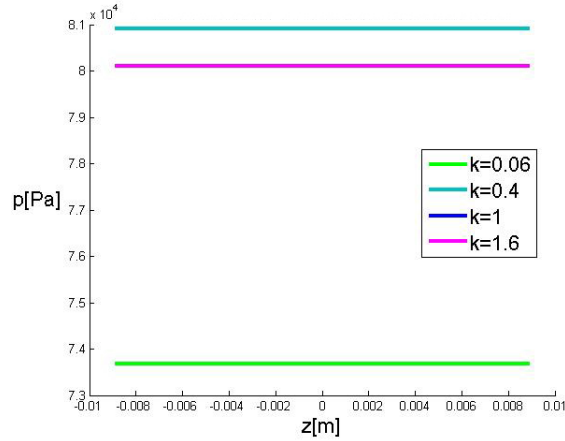
Figure 64: Total field pressure along z-coordinate for $\theta = 30^o$, $\phi = 0^o$, $\beta = -0.1988$ and $Re = 5000$, with fixed $x = 10 = 3.46 \, mm$, $y = 10 = 3.46 \, mm$ and initial $t \approx 1.69 \cdot 10^{-5} \, s$.

In figure 64 the pressure total field along z-coordinate is presented. As it is expected from the previous chapter, this flow tipology presents pressure fluctuations only along x-direction, whereas p along z-axis is costant. This trend is then to be considered less meaningful.

The pressure total field along the y direction orthogonal to the wall is now drawn in figure 65 (1a, 2a, 3a) with its respective enlargements (1b, 2b, 3b), taking into account that mean pressure P does not change along this coordinate. For instance, $k = 0.06$, related to one of the most unstable wavelengths, generates, just at small characteristic times as $t = 5 \approx 8.5 \cdot 10^{-6} \, s$ and $t = 10 \approx 1.69 \cdot 10^{-5} \, s$, a strong pressure variation at the wall of about $\Delta p \simeq 10.000 \, Pa \simeq 0.1 \, atm$ with respect to the mean pressure outer value, while $k = 0.4$ leads pressure to lightly less significant changes.

130
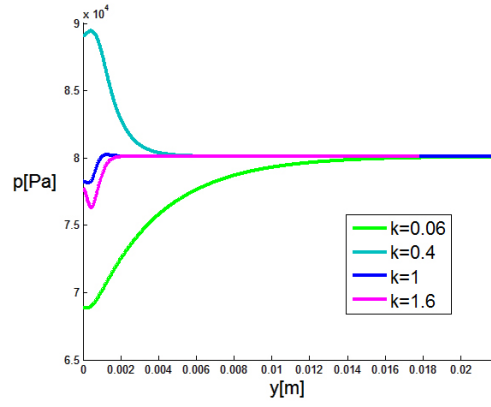
(1)
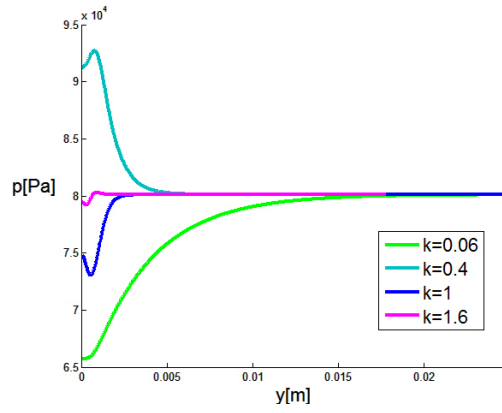
(2)
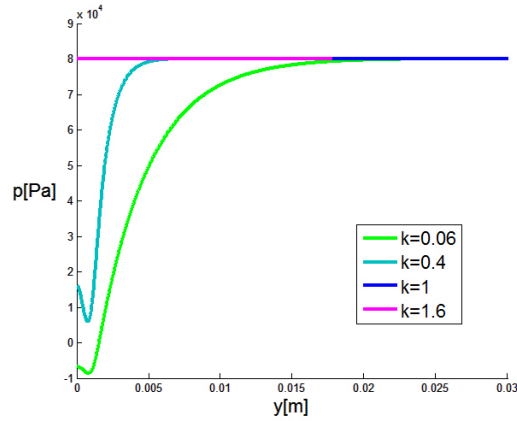
(3)

Figure 65: Spatial evolution of pressure $p = p(y)$ at characteristic times $t_1 = 5 \approx 8.5 \cdot 10^{-6}\,s$ (1), $t_2 = 10 \approx 1.69 \cdot 10^{-5}\,s$ (2) and $t_3 = 95 \approx 0.00016\,s$ (3), for $x = 10 = 3.46\,mm$ and $z = 3 = 1.04\,mm$.

131

It is to notice that only after $t = 95 \approx 0.00016\, s$, figure 65 (3), for $k = 0.06$, the pressure amount at wall have just been changing of about $|\Delta p| \simeq 90.000\, Pa \simeq 0.9\, atm$ with respect to the mean value.

In general, increasing k, pressure variations become smaller. The shorter wavelengths, indeed, first slightly increase their related pressure quantities at wall and then make them very small around the outer pressure value.

Observing then pressure profiles thicknesses, it is to notice that these do not change much proceeding in time, as they vary from $y \leq 2\, mm$ to $y = 2\, cm$, for short and long wavelengths respectively.

(a)   (b)
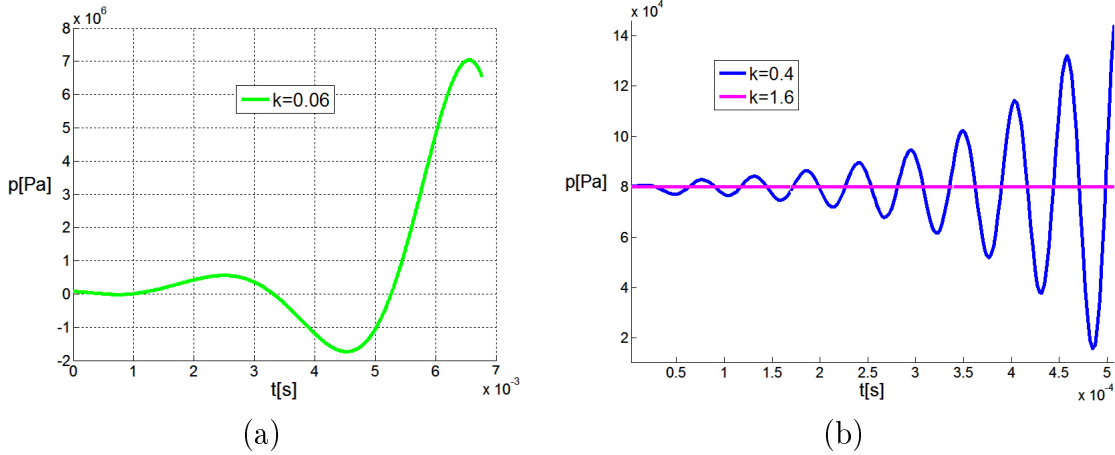
Figure 66: Temporal development of total field pressure at a fixed point in space, $x = 10 = 3.46\, mm$, $y = 10 = 3.46\, mm$, $z = 3 = 1.04\, mm$, on varying wavelength number k, for $k = 0.06$ (a) and enlargement for $k = 0.4$ and $k = 1.6$ (b), for $\theta = 30^o$, $\phi = 0^o$, $\beta = -0.1988$ and $Re = 5000$.

Being this flow configuration, $k = 0.06$, unstable, a progressive and large increase in pressure quantities along time is expected. That statment is confirmed, indeed, by the simulation of pressure total field temporal behaviour for a fixed x, y, z point in the computational domain, shown in figure 66.

It is important to notice that global pressure increases in time with an oscillating behaviour. This pressure growth is related instead to the chosen unstable configura-

132

tion leading to a strong variation $|\Delta p| \simeq 7 \cdot 10^6 \, Pa \approx 16 \, atm$ around its mean value only after $t = 0.0065 \, s$, for $k = 0.06$. Proceeding toward $k = 0.4$, pressure presents a more contained increase with changes that come to about $\Delta p \simeq \pm 6 \cdot 10^4 \, Pa \approx 0.6 \, atm$.

The oscillation period for $k = 0.4$ is of $\Delta t = 0.6 \cdot 10^{-4} \, s$ which is a very short time, while pressure for $k = 0.06$ repeats itself after $\Delta t = 0.005 \, s$, being the oscillation time one order of magnitude higher.

Finally, it can be deduced that this great pressure oscillating growth, in time and space, it is very dangerous both for aerodynamics and structural aspects, as the turbulent *flow separation* due to the strong deceleration of the flow and *aeroelastic effects* (*flattering* phenomenon) related to pressure fluctuations on the wing respectively.

Pressure surfaces are shown below in figure 67. As it can be seen, the wave entering the three-dimensional boundary layer is completely longitudinal and oscillating along this direction very close to the wall, that is the boundary layer region. Proceeding away from the wall, the oscillating trend of the pressure cancels out reaching the outer free-stream pressure amount. Along z-axis no variation of pressure is shown.
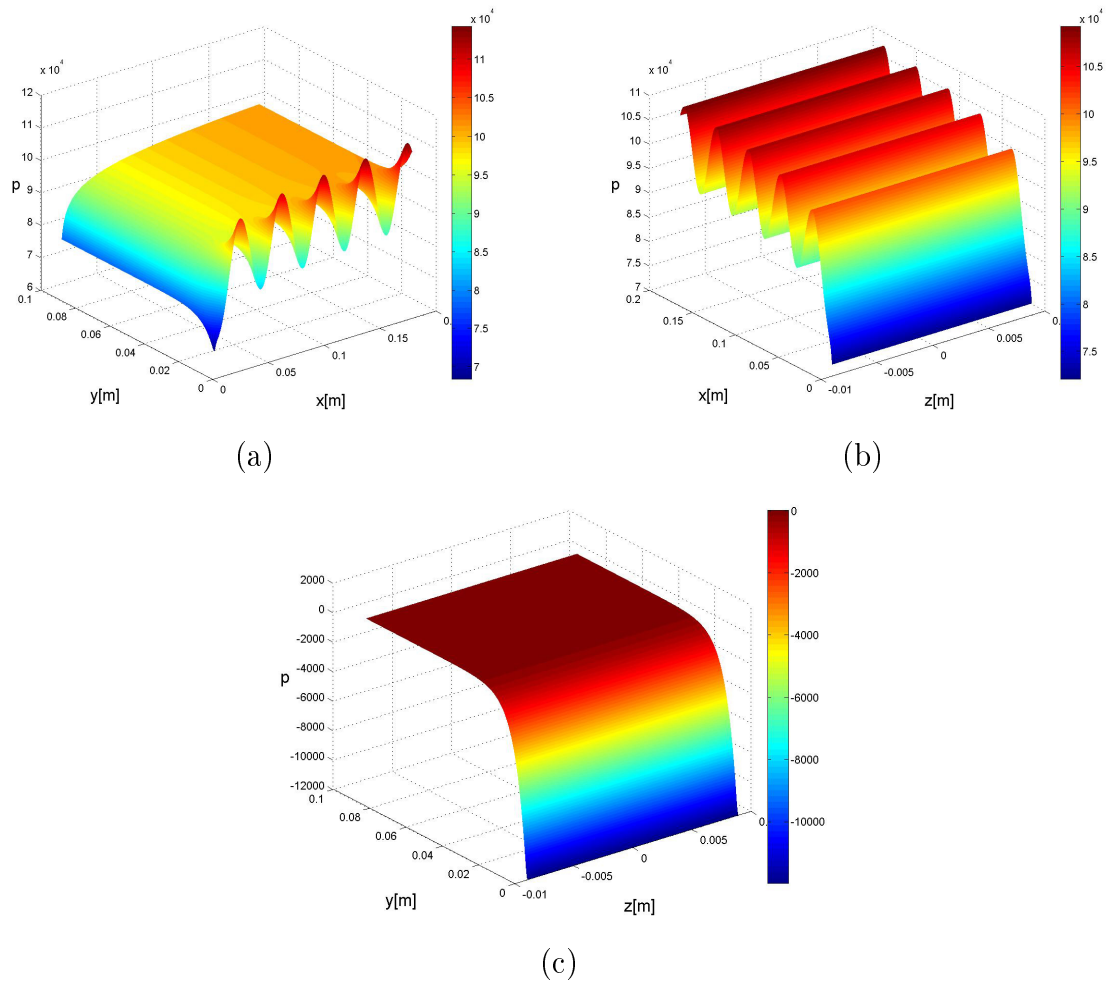
Figure 67: Pressure total field *bidimensional surfaces* on $x-y$ (a), $x-z$ (b), $y-z$ (c) planes at initial time, for $k = 0.06$, $\theta = 30^o$, $\phi = 0^o$, $\beta = -0.1988$ and $Re = 5000$ configuration within a $2\,cm$ long x-domain.

5.2.2 Simulation for $\theta = 60^o$, $\phi = 90^o$, $\beta = -0.1988$, $Re = 5000$

The last simulation presented is related to the highest characteristic angles achievable, that is *crossflow angle* $\theta = 60^o$ and *obliquity angle* $\phi = 90^o$, which characterizes a completely orthogonal wave. The hypothesis of positive pressure gradient along x-coordinate stays valid.

Being $\phi = 90^o$ linked to an *orthogonal wave* an influence of pressure disturbances on the mean pressure field only along z-direction is expected and confirmed by the following figures 68 and 69.
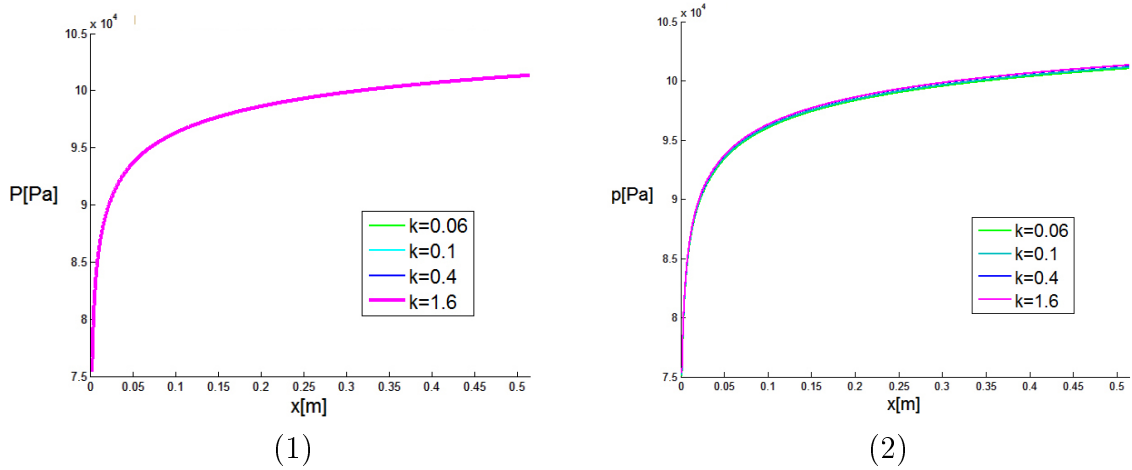
Figure 68: Mean pressure (a) and pressure of total field after the superimposition of perturbative pressure (b) along x-coordinate, belonging to $0.5\,m$ long computational domain and starting from $^x\!/c = 0.5$, for $\theta = 60^o$, $\phi = 90^o$, $\beta = -0.1988$ and $Re = 5000$, with fixed $y = 10 = 3.46\,mm$, $z = 3 = 1.04\,mm$ and initial $t \approx 1.69 \cdot 10^{-5}\,s$.

As it can be seen in figure 68, the mean pressure P increasing trend (a) does not practically change along x-axis adding the perturbative pressure field (b). The p is noted to be unchanged with respect to mean pressure field, as the perturbative pressure profiles do not vary along x coordinate.

On the other hand, in figure 69, a significant oscillating pressure trend in the total field is clear, mainly for low and intermediate wavelengths, identified by $k = 0.06$ and $k = 0.1$ respectively, as just analysed in section 4.2.1.
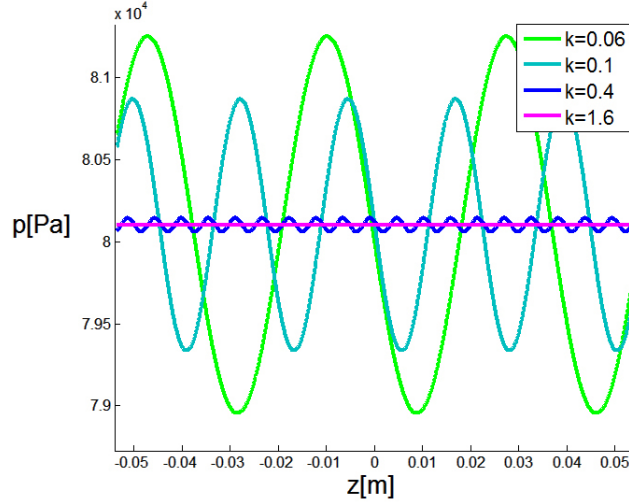
Figure 69: Total field pressure along z-coordinate for $\theta = 60^o$, $\phi = 90^o$, $\beta = -0.1988$ and $Re = 5000$, with fixed $x = 10 = 3.46\,mm$, $y = 10 = 3.46\,mm$ and initial $t \approx 1.69 \cdot 10^{-5}\,s$.

The pressure here reaches low changes for $k = 0.4$, as the previous flow tipology, only about $\Delta p \simeq \pm 43\,Pa \approx \pm 4.24 \cdot 10^{-4}\,atm$ with respect to a mean value, at $x = 3.5\,mm$, $P = 80102\,Pa$ and a period of oscillation around the mean flow of $z \approx 2.8\,mm$. Proceeding forward to higher x points, the greatest absolute pressure quantities are achieved, exactly as the previous configuration.

On the contrary, increasing the introduced wavelengths, for $k = 0.1$ and $k = 0.06$, changes in pressure are $\Delta p \simeq \pm 766\,Pa \approx \pm 7.56 \cdot 10^{-3}\,atm$ and $\Delta p \simeq \pm 1135\,Pa \approx \pm 1.1 \cdot 10^{-2}\,atm$ respectively. For $k = 0.1$, oscillation period is of about $z \approx 2.2\,cm$, while for $k = 0.06$ period increases to $z \approx 3\,cm$.

These changes in pressure with respect to the mean value seem to be less significant than the ones observed in the previous flow tipology, which affects only pressure along x-axis. For istance, variations Δp here results four times lower than the changes obtained for the longitudinal wave. This may be related to a certain loss of effectiveness of the pressure disturbances if crosswise perturbations with respect to the streamlines are introduced inside the boundary layer.

136

(1a)
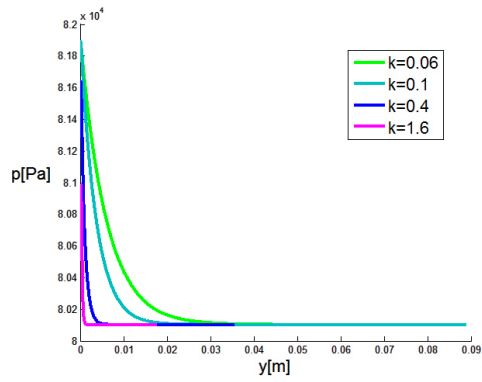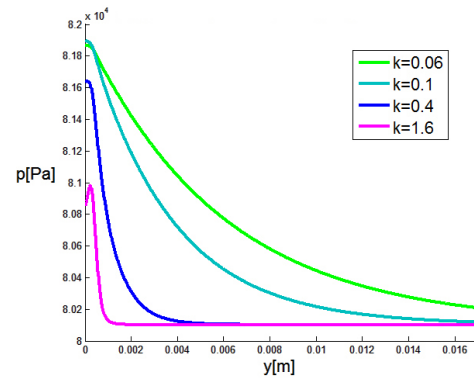
(1b)
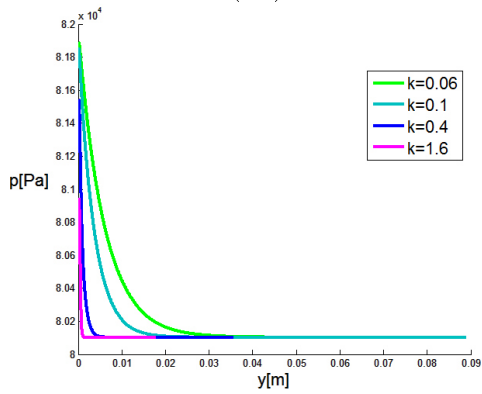
(2a)
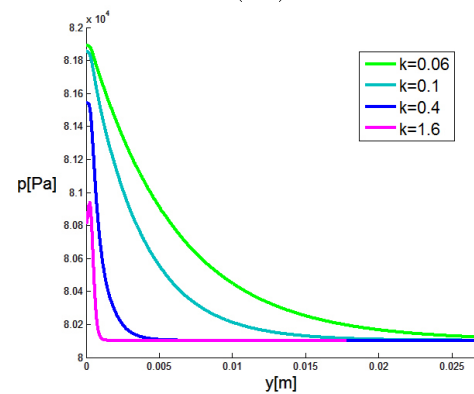
(2b)
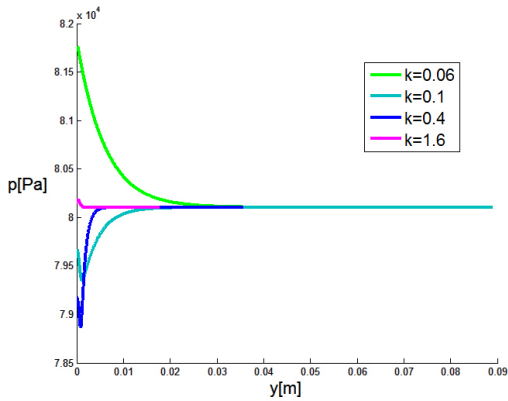
(3a)
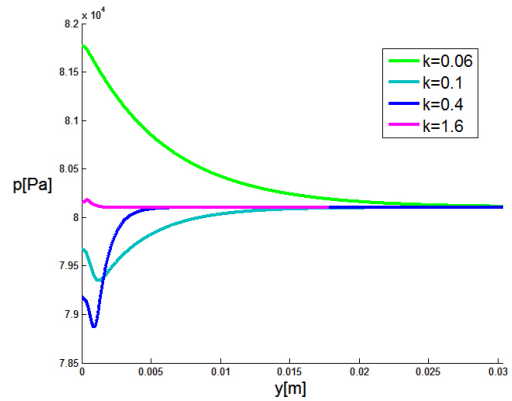
(3b)

Figure 70: Spatial evolution of pressure $p = p(y)$ at characteristic times $t_1 = 5 \approx 8.5 \cdot 10^{-6}\,s$ (1a), $t_2 = 10 \approx 1.69 \cdot 10^{-5}\,s$ (2a) and $t_3 = 95 \approx 0.00016\,s$ (3a), $x = 10 = 3.46\,mm$ and $z = 3 = 1.04\,mm$, and enlargements at the wall (1b, 2b, 3b).

As far as pressure trend along y-coordinate is concerned, figure 70 is shown. Also for this flow configuration, a variation of the pressure inside the boundary layer is shown. The changes in pressure with respect to the outer freestream pressure quantity are slightly lower than for the longitudinal pressure wave. This fact is probably linked to the previous one observed for pressure trend along z-axis, which presents lower oscillations. Pressure values at wall here change from $p = 80800\,Pa \approx 0.79\,atm$ for short wavelength $k = 1.6$ to $p = 81900\,Pa \approx 0.8\,atm$ for long wavelength $k = 0.06$, with a variation with respect to the outer value of about $\Delta p \simeq 7 \cdot 10^{-3}\,atm$ and $\Delta p \simeq 1.8 \cdot 10^{-2}\,atm$ respectively.

It is important to notice that, even if pressure values at wall oscillate around the outer mean quantity, pressure profiles maintain their thickness steady in time, overtaking the computed velocity profiles thickness inside the three-dimensional boundary layer, $\delta = 0.86\,mm$, for long wavelengths, $y \simeq 20\,mm$ and $y \simeq 30\,mm$, and for shorter wavelengths, $y \simeq 7\,mm$ and $y \simeq 2\,mm$.

Finally, in figure 71 the temporal development of the pressure total field at a fixed x, y, z coordinate is presented. The expected significant growth of pressure in time is confirmed, as greater as the wave number is decreased.

In figure 71 (a), instead, the enlargement shows how for $k = 1.6$ no changes can be noticed in pressure temporal development, while $k = 0.4$ leads the pressure field to a temporal growth, which reaches a variation of about $\Delta p \simeq 2200\,Pa \approx 2 \cdot 10^{-2}\,atm$ just at $t = 0.001\,s$. The temporal oscillation period is of about $t \simeq 0.00035\,s$, which is a very small quantity.

This quantity almost triples for $k = 0.1$, as shown in figure 71 (b), where an higher time has been taken into account. The time period is now of about $t \simeq 0.0006\,s$, while the variation in amplitude reaches $\Delta p \simeq 40000\,Pa \approx 0.4\,atm$ after $t = 0.0025\,s$.

Higher wavelengths, as $k = 0.06$, presents higher pressure values. In figure 71 (c) then the simulation time is further increased in order to allow a better view of the pressure development. At $t = 0.006\,s$ the pressure reaches a variation with respect to the mean value of about $\Delta p \simeq 99900\,Pa \approx 0.98\,atm$, which represents a significant and dangerous growth. However, the oscillation period is further increased of one

138

order of magnitude, $t \simeq 0.002 \, s$.

(a)

(b)

(c)
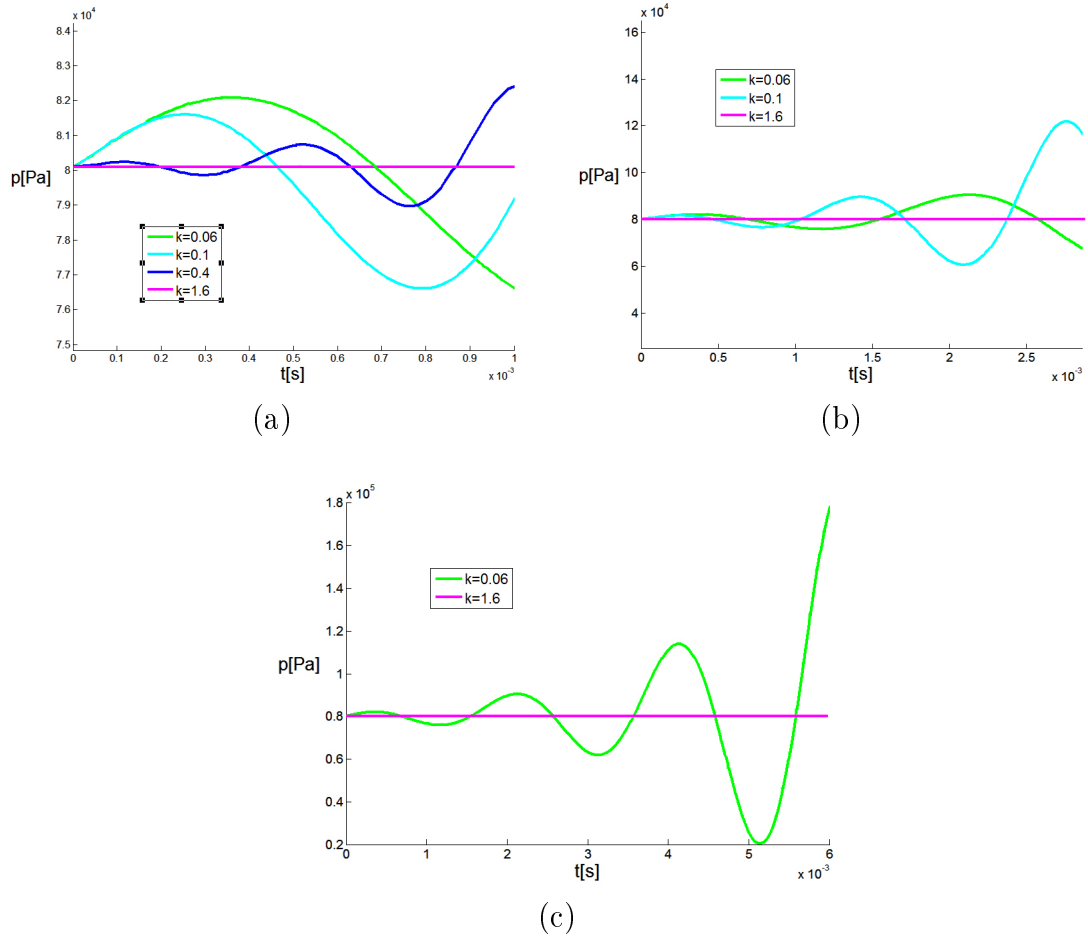
Figure 71: Temporal development of total field pressure at a fixed point in space, $x = 10 = 3.46 \, mm$, $y = 10 = 3.46 \, mm$, $z = 3 = 1.04 \, mm$, on varying wavelength number k, related to $k = 0.4$ (a), $k = 0.1$ (b) and $k = 0.06$ (c), for $\theta = 60^o$, $\phi = 90^o$, $\beta = -0.1988$ and $Re = 5000$.

Bidimensional pressure surfaces of the total field are shown in figure 72 in order to highlight the oscillating behaviour of pressure field along z-direction, which however presents lower peaks than pressure surfaces of the previous flow tipology.

(a)
(b)
(c)
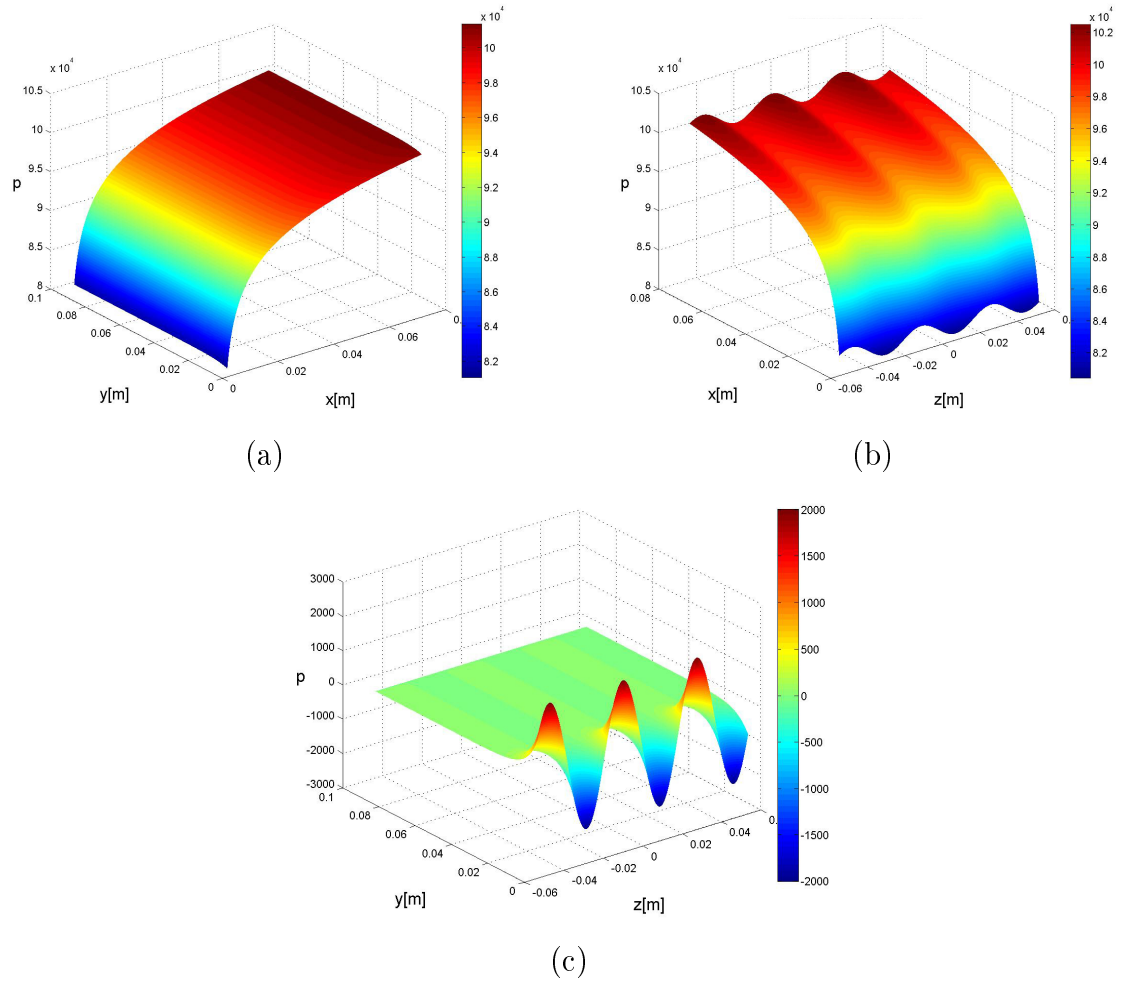
Figure 72: Pressure total field *bidimensional surfaces* on $x-y$ (a), $x-z$ (b), $y-z$ (c) planes at initial time, for $k = 0.06$, $\theta = 30^o$, $\phi = 0^o$, $\beta = -0.1988$ and $Re = 5000$ configuration within a $2\,cm$ long x-domain.

6 Conclusions

The numerical simulation implemented in previous chapters has turned out to be very useful in order to investigate the pressure field in the crossflow three-dimensional boundary layer about all its aspects. Investigating and studying the crossflow boundary layer pressure field can be very important and meaningful for practical purposes, since the swept-back wing is the most used configuration in aeronautical designs.

MATLAB software has allowed us to compute the complete pressure field regarding both the perturbative pressures and the *pressure total field*, which derived from the superimposition of the first one on the base flow. This method is validated by the *theory of small disturbances* and through the use of the *initial values formulation*. Moreover the numerical computation needs to start from perturbative velocities given by the database of the *Department of Mechanical and Aerospace Engineering*.

The PARAMETRIC ANALYSIS has allowed us to reach meaningful results about the effects of characteristic crossflow parameters k, ϕ, θ, β and Reynolds number on the pressure perturbative field inside the boundary layer. Important links, implementing temporal simulations, between amplication factor G and the perturbative pressure field $\tilde{p}$ has been also achieved.

In particular, the variation of *Reynolds number*, from $Re_{\delta*} = 100$ to $Re_{\delta*} = 5000$, leads the pressure field, from a stable condition in which all perturbative pressures quickly cancel out to an unstable state, for pressure disturbances with low *wavenumbers*, $k \leq 1$, and a $\phi = 90^o$ obliquity angle. The different amounts of k, furthermore, cause variations in x, z pressure trends, with higher amplitude and oscillations periods for lower k, and in pressures profiles along direction orthogonal to the wall as well.

Then variations in *obliquity angle* ϕ and also in *crossflow angle* θ generate instability, related to the consequent *"blast"* which leads to a significant growth of the pressure. Two flow configuration has been detected as the most unstable and meaningful, $\theta = 30^o$, $\phi = 0^o$ and $\theta = 60^o$, $\phi = 90^o$, where the perturbative pressure waves are introduced crosswise the reference streamline, in an inclined flow, and longitu-

dinally, in a slightly inclined flow, respectively. In general high ϕ and θ lead to an increasing of the temporal transient growth of the perturbative pressure.

Concerning *pressure gradient* β variation, a negative value, $\beta = -0.1988$, related to a positive pressure gradient along x-axis, $\partial p / \partial x > 0$, results to be very destabilizing for the pressure field, leading to a strong growth indeed.

All these results confirm the correlation which exists between G and $\tilde{p}$ quantities, even if a certain *phase delay* in G maximum and minimum points has been noticed. This fact can lead to use the amplification factor analysis, for every fixed tipology of crossflow on the wing, as a prevision of the possible strong pressure temporal growth related to instability.

As far as the MEAN AND PERTURBATIVE PRESSURE FIELD DIMENSIONAL ANALYSIS is concerned, this can be considered useful for practical purposes. In this thesis only the two most unstable flow configurations have been investigated, that are given by the previous parametric analysis and take place in the region downstream the 50% of the airfoil chord, where the pressure gradient is positive. The computational domain, starting from this point, has been extended to the trailing edge and ground standard conditions has been taken into account. The mean pressure trend has been given by the *Rosenhead* mathematical expansion.

The most interesting fact is that the lengthwise introduced perturbative pressure waves, in the first case, strongly affect the increasing mean pressure trend along x-coordinate, while, in second case, the z-direction only shows significant pressure fluctuations around the mean value. In the first case, close to the trailing edge region, great pressure changes, $p \simeq 10,77 \cdot 10^4 \, Pa$, are achieved, suggesting that this is the most dangerous region, in terms of pressure growth, in case of an unstable crossflow configuration presenting low wavelengths.

The strong and quick pressure growth and the oscillating behaviour, in time and space, suggest the usefulness of further deep studies about this particular three-dimensional pressure field. This computation can also provides useful results for *aeroelastic* and *structural analysis*, since the oscillating pressure field could generate dangerous phenomena, as *flattering* and *vibrations propagation*, that can damage the

structure, periodically stressed, and even make the aircraft uncontrollable.

Since the relevance of this numerical simulation has been highlighted, improvements and expansions of this method may be realized in order to better approach the real model, that is the swept-back wing. In order to achieve these aims, an increasing of the spatial domain may be enforced. Thus the whole wing model could be considered and analised, making also the negative pressure gradient region part of the computational domain or even computing a variable pressure gradient related to each chord coordinate. Moreover, different case of altitude and velocity may be taken into account in order to compare the analysis with real fly conditions.

The temporal computational domain could be also enlarged, coming to seconds, in order to observe a longer development of the flow and understand which high values pressure could reach.

Finally, reasons for justify the interest in studies about pressure field, inside the three-dimensional crossflow boundary layer, are, as seen, numerous. The final and intrinsic purpose is to provide concrete results and behaviours, for the pressure field of this recurrent flow tipology, to the design area.

List of Figures

145

List of Tables

References

[1] J.D. Anderson Jr, "Ludwig Prandtl's Boundary Layer", Physics Today, December 2005

[2] D.Arnal and J.Dèlery, "Laminar-turbolent transition and shock wave/boundary layer interaction", presentato a RTO AVT Lecture Series on Critical Technologies for Hypersonic Vehicle Development, von Kármán Institute, Rhode-St-Genèse, Belgium, 10-14 May, 2004, e published in RTO-EN-AVT-116

[3] H.Schlichting, "Boundary Layer Theory", New York, McGraw-Hill, 1951

[4] W.S.Saric, R.B.Carrillo Jr., M.S.Reibert, "Non-linear Stability and Transition in 3-D Boundary Layers", Arizona State University, Mechanical and Aerospace Engineering; Tempe, USA, published in Meccanica, May 1998

[5] W.S.Saric[1], H.L.Reed[1], E.B.White[2], "Stability and Transition of Three-Dimensional Boundary Layers", [1]Arizona State University, Mechanical and Aerospace Engineering; Tempe, USA e [2]Case Western Reserve University, Mechanical and Aerospace Engineering; Cleveland, Ohio, USA; published in Annual Reviews Fluid Mechanics, 2003.

[6] E.B.White[1] and W.S.Saric[2], "Secondary instability of crossflow vortices", [1]Case Western Reserve University, Mechanical and Aerospace Engineering; Cleveland, Ohio, USA; [2]Texas A&M University, Texas, USA; published in J.Fluid Mechanics, vol. 525, pp. 275-308, 2005

[7] P.Wassermann and M.Kloker, "Transition mechanisms induced by travelling crossflow vortices in a three-dimensional boundary layer", Institut für Aerodynamik und Gasdynamik, Universität Stuttgart, Pfaffenwaldring 21, Stuttgart, Germany; published in J.Fluid Mechanics, vol. 483, pp. 67-69, 2003

[8] S. Scarsoglio, D.Tordella [1], W.O.Criminale [2], "Role of long waves in the stability of the plane wake", [1]Department of Mechanical and Aerospace Engineering,

Politecnico di Torino, Torino, Italy; [2]Department of Applied Mathematics, University of Washington, Seattle, Washington , USA; published in Physical Review E 81, 036326, 2010

[9] S.Scarsoglio, F.De Santi, D.Tordella, "On the frequency of hydrodynamic perturbations. From the early transient through the intermediate term to the asymptotic state", Department of Mechanical and Aerospace Engineering, Politecnico di Torino, Torino, Italy; submitted to New J. Phys.

[10] L. Rosenhead, "Laminar Boundary Layers", London, Oxford University Press, 1963

[11] G.Iuso, F.Quori, "Gasdinamica", Torino, Levrotto & Bella, 2000